ROYAUME DU MAROC
Université Mohammed V
- RABAT -
جامعة محمد الخامس
- الرباط -
Faculté des sciences
كلية العلوم

université
PARIS-SACLAY

CENTRE D'ETUDES DOCTORALES - SCIENCES ET TECHNOLOGIES

N° d'ordre ……C27……

THESE

En vue de l'obtention du : ***DOCTORAT***

Structure de Recherche: Laboratoire de Matière Condensée et Sciences Interdisciplinaires
Discipline: Physique
Spécialité: Matière condensée et Modélisation des systèmes

Présentée et soutenue le 14/11/2018 par :

Khalid QUERTITE

Silicene Growth on Insulating Ultra-Thin Film of NaCl

JURY

Abdelilah BENYOUSSEF	PES, Académie Hassan II des Sciences et Techniques Rabat	Président
Haik JAMGOTCHIAN	HDR, Centre Interdisciplinaire de Nanoscience de Marseille	Rapporteur
Mimouna BAITOUL	PES, Université Sidi Mohammed ben Abdellah Faculté des des sciences, Fez	Rapporteur
Hamid OUGHADDOU	PES, Institut des Sciences Moléculaires d'Orsay	Directeur
Abdallah EL KENZ	PES, Université Mohammed V Faculté de sciences, Rabat	Co-directeur
Nicolas TRCERA	Docteur, Synchrotron SOLEIL, Paris	Co-encadrant
Gregory CABAILH	Maître de conférences, Institut des Nanosciences de Paris	Examinateur
Didier RIBAT	HDR, Ecole Polytechnique Palaiseau, Paris	Examinateur

Année Universitaire
2018-2019

Résume (max 200 mots)

Le silicène est l'équivalent du graphène pour le silicium avec une structure bidimensionnelle (2D). Il est supposé avoir des propriétés électroniques intéressantes comme les fermions de Dirac sans masse et présentant une grande mobilité des électrons. L'existence du silicène a été montrée récemment sur des substrats de métaux nobles comme l'argent. Cependant les résultats montrent des interactions fortes entre la couche de silicène et le substrat métallique, ce qui a pour conséquence de détruire les propriétés électroniques intrinsèques du silicène.

Dans le but de résoudre ce problème, nous proposons dans ce travail d'explorer d'autres substrats potentiels présentant de faibles interactions avec le silicene. Nous avons étudié la croissance de couches 2D de silicium sur un film mince isolant de NaCl.

Nous avons étudié les propriétés structurales et électroniques des couches de silicium 2D déposées sur un film mince de NaCl, lui-même déposé sur un substrat d'Ag (110). L'absorption d'atomes de silicium sur les films de NaCl révèle l'existence d'une couche de silicium 2D superficielle avec une structure très ordonnée en forme de nids d'abeilles. Cette couche présente une interaction faible avec le substrat tout en étant analogue au silicène.

Mots-clefs (5) : Science des surfaces, microscope à effet tunnel, silicène, LEED, XPS

Abstract (max 200 mots)

Silicene, the silicon-based analog of graphene which has a two-dimensional (2D) structure. It is expected to have attractive electronic properties such as massless Dirac fermions and high electron mobility. The existence of silicene has been shown recently on noble metal substrates such as Ag and Au. The results present strong interactions between the silicene ad-layer and the metallic substrate which destroy the intrinsic electronic properties of silicene.

In order to solve this problem, we propose in this work to explore other potential substrates that have weaker interactions with silicene. We studied the growth of a 2D silicon layer on insulating NaCl thin film.

We studied the structural and electronic properties of 2D silicon layer grown on a NaCl film deposited over Ag (110) substrate. The adsorption of silicon atoms on NaCl films reveals the existence of a 2D silicon sheet ad-layer with a highly ordered honeycomb-like structure. The silicon ad-layer has weak interactions with the substrate and it mimics the structure of silicene.

Key Words (5): Surface science, tunneling microscope, silicene, LEED, XPS

Acknowledgments

The work that is the subject of this thesis is the fruit of a cotutelle agreement between the University Mohammed V, Faculty of Sciences Rabat and the University Paris-Saclay. This work was supervised by **Mr. Abdallah EL KENZ** from the Condensed Matter and Interdisciplinary Sciences laboratory (LaMCScI) in Rabat and **Mr. Hamid OUGHADDOU** from the Molecular Sciences Institute of Orsay in the "Molecular Nanoscience" team.

First of all, I would like to express my sincere gratitude to my supervisor **Mr. Hamid OUGHADDOU** for giving me the opportunity to conduct my PhD thesis in the Molecular Nanoscience group at ISMO. I would like to thank him for the continuous support from day one, for his patience, motivation and immense knowledge. This work could not see the light without his guidance and help, not just from the scientific part but also from the financial part.

I am grateful to my co-supervisor **Mr. Abdallah EL KENZ** for accepting to supervise this thesis from the university of Mohammed V – Science faculty, Rabat and help make this work a cotutelle project between the France and Morocco universities. Thank you for the confidence he showed me from the beginning to the end of the work and for his availability.

I would also to thanks my co-supervisor **Mr. Nicolas TRCERA** (Synchrotron SOLEIL, Paris) for giving me the opportunity to work at LUCIA Beamline at Synchrotron SOLEIL, Paris. Thank you for all the explications regarding the XAS technique and all the encouragement during the experiments and during the thesis writing period.

My sincere thanks to the president of the jury **Mr**. **Abdelilah BENYOUSSEF** (Académie Hassan II des Sciences et Techniques Rabat) who do me the honor of chairing this jury.

I am grateful to **Mr. Haik JAMGOTCHIAN** (Centre Interdisciplinaire de Nanoscience de Marseille) who have done me the honor to study my work attentively and having accepted to be rapporteur of this thesis and for having provided me with multitude of research avenues for the coming years.

I am also grateful to **Mrs. Mimouna BAITOUL** (Université Sidi Mohammed ben Abdellah Faculté des sciences, Fez) for having accepted to be rapporteur of this thesis and help broadened my knowledge thanks to all the insightful comments.

I would also to thanks **Mr. Gregory CABAILH** (Institut des Nanosciences de Paris) for agreeing to examine this thesis as well as for the remarks he addresses me to improve my work.

I would like to express my gratitude to **Mr. Didier PRIBAT** (Ecole Polytechnique Palaiseau, Paris) for his attentive reading of my thesis and accepting to examine and judge this work.

I gratefully acknowledge the financial support received from LabEx via the SILCENE project (AAP Recherche 2015) and Synchrotron SOLEIL.

I am also grateful to **Mrs. Hanna ENRIQUEZ** (ISMO, Orsay), **Mr. Pierre LAGARDE** (Synchrotron SOLEIL, Paris), **Mr. Azzedine BENDOUNAN** (Synchrotron SOLEIL, Paris),

Mr. Abdelkader KARA (University of Central Florida, Orlando) and **Mrs. Karima LASRI** (University of Central Florida, Orlando) for the help regarding the experiments, the data analysis and the theoretical contribution performed during this thesis.

Special thanks to **Mr. Andrew MAYNE** (ISMO, Orsay) and **Mr. Jean Louis LE MAIRE** (ISMO, Orsay) for all the explications regarding UHV instruments, all the friendly talks and for helping to correct my thesis manuscript.

I would like to acknowledge honorary all the members of Molecular Nanoscience group at ISMO and Lucia Beamline at Synchrotron SOLEIL for all the friendly talks and for been a source of good advice and collaboration.

Abstract

Silicene, the silicon-based analog of graphene which has a two-dimensional (2D) structure. It is expected to have attractive electronic properties such as massless Dirac fermions and high electron mobility. The existence of silicene has been shown recently on noble metal substrates such as Ag and Au. The results present strong interactions between the silicene ad-layer and the metallic substrate which destroy the intrinsic electronic properties of silicene.

In order to solve this problem, we propose in this work to explore other potential substrates that have weaker interactions with silicene. We studied the growth of a 2D silicon layer on insulating NaCl thin film. Indeed, Alkali metal halides such as NaCl offer a great solution as an alternative surface because they behave as a dielectric layer, allowing characterization of silicene material.

We studied the structural and electronic properties of 2D silicon layer grown on a NaCl film deposited over Ag(110) substrate. A combined experimental investigation was performed with a large number of techniques which are used in surface science such as: low energy electron diffraction (LEED), auger electron spectroscopy (AES), scanning tunneling microscopy and spectroscopy (STM/STS), extended x-ray absorption fine structure (EXAFS), x-ray photoelectron spectroscopy (XPS) and angle resolved photoemission spectroscopy (ARPES). The adsorption of silicon atoms on NaCl films reveals the existence of a 2D silicon sheet ad-layer with a highly ordered honeycomb-like structure. The silicon ad-layer has weak interactions with the substrate, and it mimics the structure of silicene. Finally, preliminary experiments on the growth of silicene on dissociated NaCl films are presented. The effect of electron irradiation on the NaCl film and initial ARPES measurement on the silicene intercalated-Na atoms system are presented.

Table of Contents

Introduction

Silicene, the silicon-based counterpart of graphene has a two dimensional (2D) structure. It shows interesting electronic properties such as charge carriers that behave as massless relativistic particles with high electronic mobility [1]. Silicene is considered a particularly promising material for nanotechnology because it can be integrated into industry-based silicon electronics [2]. The existence of silicene has been achieved by epitaxial growth of silicon atoms on noble metal substrates such as Ag [3-5], Au [6,7] and Ir [8]. Most studies were focused on Ag surfaces, given that 2D silicon layer self-assembled to form silicene nanoribbons (NRs) on Ag(110) with a (2x5) superstructure and silicon layer sheet on Ag(111) with a dominant (4x4) superstructure. Both 2D silicon layers show a highly ordered honeycomb-like structure.

The fact that silicene has been synthesized only by epitaxial growth over metallic surfaces results on strong interactions between the silicene ad-layer and the metallic substrate. These interactions can alter the electronic properties of silicene. Indeed, it has been demonstrated [9] that in case of silicene grown on Ag surfaces, a hybridization state rises between the Si (3p) and Ag (4d). Another study [10] reported the existence of strong electrostatic interactions between the silicene and the Ag substrate due to charge transfer between the metallic surface and the 2D silicon ad-layer. Based on experimental and theoretical investigations [11,12], it has been proven that those interactions affect the electronic properties of silicene. As a consequence, no intrinsic linear crossing bands near the *K* point of silicene (Dirac cone) were observed. Indeed, a hot debate has been rising through the years about the electronic properties of silicene. A linear dispersion in the electronic band structure of silicene grown on Ag(111) has been reported [13]. This report proved to be incorrect as it raises more questions about the real potential of silicene compared to graphene and about the future of silicene as a promising material for nanotechnology applications.

In order to solve this problem we suggest in this work to explore other potential substrates having weaker interactions with silicene. To be more specific, we aim to grow and characterize 2D silicon layer on insulating thin films of alkali halides deposited on an

Ag(110) surface. As a result, we will be able to decouple the silicene states from the substrate which will allow us to access its intrinsic properties.

Alkali metal halides films such as sodium chloride (NaCl) offer an interesting solution as an alternative surface because it can behave as a dielectric layer, allowing characterization and integration of adsorbed nanostructures such as silicene. Furthermore, the growth of such insulating films can be obtained by molecular beam epitaxy (MBE) as it has been demonstrated from NaCl deposition on metallic substrates such as Cu [14,15], Al [16] and Au [17]. On the other hand, we should note that working with insulating thin films instead of bulk insulators provides a great advantage when using electron-based surface characterization techniques due to weak charging effects. Indeed, it has been shown that using scanning tunneling microscopy with NaCl thin films allows probing individual molecular orbitals [18,19] and manipulating single ad-atoms [20].

This thesis focuses on the study of the structural and electronic properties of 2D silicon layer grown on ultrathin insulating film deposited over an Ag(110) metallic substrate. To our knowledge, the observed silicon sheet identified in this work represents the first observation of 2D silicon layer assembly on insulating material. Although this is a fairly new avenue, we believe that the new output obtained from this work would contribute in understanding the fundamental features of silicene. A combined experimental investigation was performed with a large number of techniques which are used in surface science such as: low energy electron diffraction (LEED), auger electron spectroscopy (AES), scanning tunneling microscopy and spectroscopy (STM-STS), extended x-ray absorption fine structure (EXAFS), x-ray photoelectron spectroscopy (XPS) and angle resolved photoemission spectroscopy (ARPES).

In chapter 1, we describe the basis and practical features of the experimental setup and techniques used in our experiments.

In chapter 2, an overview about the interest in insulating ultrathin films is given. Furthermore, we report the crystallographic and electronic properties of NaCl films grown on Ag(110) surface. We show that upon optimizing the growth conditions we were able to cover almost completely the metallic substrate with an insulating NaCl film.

In chapter 3, we investigate the adsorption and self-assembly of silicon atoms deposited over the NaCl film. The experiments reveal the existence of a 2D silicon sheet with a highly ordered honeycomb-like structure. Furthermore, we show that this silicon ad-layer has weak

interactions with the substrate and that it mimics the structure of silicene grown directly on Ag surfaces.

In chapter 4, we present preliminary experiments investigating the growth of silicene on dissociated NaCl film. The effect of electron irradiation on the NaCl film and initial ARPES measurement on the silicene intercalated-Na atoms system are presented.

The last part of this manuscript is devoted for general conclusions and perspectives.

Bibliography

[1] Guzmán-Verri, G.G. and Voon, L.L.Y., 2007. Electronic structure of silicon-based nanostructures. *Physical Review B*, *76*(7), p.075131.

[2] Gupta, A., Sakthivel, T. and Seal, S., 2015. Recent development in 2D materials beyond graphene. *Progress in Materials Science*, *73*, pp.44-126.

[3] Lalmi, B., Oughaddou, H., Enriquez, H., Kara, A., Vizzini, S., Ealet, B. and Aufray, B., 2010. Epitaxial growth of a silicene sheet. *Applied Physics Letters*, *97*(22), p.223109.

[4] Enriquez, H., Vizzini, S., Kara, A., Lalmi, B. and Oughaddou, H., 2012. Silicene structures on silver surfaces. *Journal of Physics: Condensed Matter*, *24*(31), p.314211.

[5] Jamgotchian, H., Colignon, Y., Hamzaoui, N., Ealet, B., Hoarau, J.Y., Aufray, B. and Bibérian, J.P., 2012. Growth of silicene layers on Ag (111): unexpected effect of the substrate temperature. *Journal of Physics: Condensed Matter*, *24*(17), p.172001

[6] Enriquez, H., Mayne, A., Kara, A., Vizzini, S., Roth, S., Lalmi, B., Seitsonen, A.P., Aufray, B., Greber, T., Belkhou, R. and Dujardin, G., 2012. Adsorption of silicon on Au (110): An ordered two dimensional surface alloy. *Applied Physics Letters*, *101*(2), p.021605.

[7] Sadeddine, S., Enriquez, H., Bendounan, A., Das, P.K., Vobornik, I., Kara, A., Mayne, A.J., Sirotti, F., Dujardin, G. and Oughaddou, H., 2017. Compelling experimental evidence of a Dirac cone in the electronic structure of a 2D Silicon layer. *Scientific Reports*, *7*, p.44400.

[8] Meng, L., Wang, Y., Zhang, L., Du, S., Wu, R., Li, L., Zhang, Y., Li, G., Zhou, H., Hofer, W.A. and Gao, H.J., 2013. Buckled silicene formation on Ir (111). *Nano Letters*, *13*(2), pp.685-690.

[9] Johnson, N.W., Vogt, P., Resta, A., De Padova, P., Perez, I., Muir, D., Kurmaev, E.Z., Le Lay, G. and Moewes, A., 2014. The metallic nature of epitaxial silicene monolayers on Ag (111). *Advanced Functional Materials*, *24*(33), pp.5253-5259.

[10] Stephan, R., Hanf, M.C. and Sonnet, P., 2014. Spatial analysis of interactions at the silicene/Ag interface: first principles study. *Journal of Physics: Condensed Matter*, *27*(1), p.015002.

[11] Lin, C.L., Arafune, R., Kawahara, K., Kanno, M., Tsukahara, N., Minamitani, E., Kim, Y., Kawai, M. and Takagi, N., 2013. Substrate-induced symmetry breaking in silicene. *Physical Review Letters*, *110*(7), p.076801.

[12] Wang, Y.P. and Cheng, H.P., 2013. Absence of a Dirac cone in silicene on Ag (111): First-principles density functional calculations with a modified effective band structure technique. *Physical Review B*, *87*(24), p.245430.

[13] Vogt, P., De Padova, P., Quaresima, C., Avila, J., Frantzeskakis, E., Asensio, M.C., Resta, A., Ealet, B. and Le Lay, G., 2012. Silicene: compelling experimental evidence for graphenelike two-dimensional silicon. *Physical Review Letters*, *108*(15), p.155501.

[14] Repp, J., Meyer, G. and Rieder, K.H., 2004. Snell's law for surface electrons: Refraction of an electron gas imaged in real space. *Physical Review Letters*, *92*(3), p.036803.

[15] Repp, J., Meyer, G., Paavilainen, S., Olsson, F.E. and Persson, M., 2005. Scanning tunneling spectroscopy of Cl vacancies in NaCl films: strong electron-phonon coupling in double-barrier tunneling junctions. *Physical Review Letters*, *95*(22), p.225503.

[16] Hebenstreit, W., Redinger, J., Horozova, Z., Schmid, M., Podloucky, R. and Varga, P., 1999. Atomic resolution by STM on ultra-thin films of alkali halides: experiment and local density calculations. *Surface Science*, *424*(2-3), pp.L321-L328.

[17] Loppacher, C., Zerweck, U. and Eng, L.M., 2003. Kelvin probe force microscopy of alkali chloride thin films on Au (111). *Nanotechnology*, *15*(2), p.S9.

[18] Repp, J., Meyer, G., Stojković, S.M., Gourdon, A. and Joachim, C., 2005. Molecules on insulating films: scanning-tunneling microscopy imaging of individual molecular orbitals. *Physical Review Letters*, *94*(2), p.026803.

[19] Doppagne, B., Chong, M.C., Lorchat, E., Berciaud, S., Romeo, M., Bulou, H., Boeglin, A., Scheurer, F. and Schull, G., 2017. Vibronic Spectroscopy with Submolecular Resolution from STM-Induced Electroluminescence. *Physical Review Letters*, *118*(12), p.127401.

[20] Repp, J., Meyer, G., Olsson, F.E. and Persson, M., 2004. Controlling the charge state of individual gold adatoms. *Science*, *305*(5683), pp.493-495.

Chapter 1. Experimental Techniques and Methods

The experimental investigation performed in this thesis has been realized using:

- Low Energy Electron Diffraction (LEED)
- Auger Electron Spectroscopy (AES)
- Scanning Tunneling Microscopy (STM)
- Scanning Tunneling Spectroscopy (STS)
- Extended X-ray Absorption Fine Structure (EXAFS)
- X-Ray Photoelectron Spectroscopy (XPS)
- Angle Resolved Photoemission Spectroscopy (ARPES)

In this chapter a brief description about the basis and practical features of these instrumental techniques is presented.

1.1. Low Energy Electron Diffraction (LEED)

Low energy electron diffraction (LEED) is considered one of the most used techniques in materials science research to investigate crystallographic structures of surfaces. Though discovered in 1927 by Clinton Davisson and Lester Germer, LEED did not become a popular instrument for surface investigation until the 1960s. The main reasons were that observing spots of diffracted beams and construction of clean metal surfaces were a problematic experimental procedure because of the weak vacuum techniques.

1.1.1 General Aspects of LEED Theory

By the laws of wave-particle duality, the beam of electrons may be considered as a series of electron waves incident on the sample. These waves will be scattered by the atoms of the surface. The wavelength of the electrons is given by the De Broglie relation:

$$\lambda = h/p \tag{1.1}$$

Where,

$$p = (2mE_c)^{1/2} \tag{1.2}$$

$$\lambda = h/(2mE_c)^{1/2} \tag{1.3}$$

As a result,

$$\lambda = \sqrt{\frac{150.4}{E_c(eV)}} \tag{1.4}$$

In the relations above, m is the mass of the electron, h is the planck's constant and E_c is the kinetic energy of the electron. For low kinetic energies between a few ten and a few hundred electrons volts (20-200 eV), the electrons wavelengths are of the order of 0.1 nm, *i.e.* similar to the regular interatomic spacing of crystals. Apart from the suitable wavelength, a short penetration depth of the low energy electrons of LEED is considered as a crucial aspect in researching the crystallographic structure of ordered surfaces.

LEED's Kinematic Theory

To understand the essential features of LEED experiment, kinematic theory of diffraction [1] is needed. Kinematic theory describes the situation when only "single scattering" exists, in which circumstance an electron that has been scattered once by a surface atom will not be scattered again by another surface atom.

For an incident electron beam with wave vector $k_i = \frac{2\pi}{\lambda_i}$ and diffracted wave vector $k_d = \frac{2\pi}{\lambda_d}$, the rule for constructive interference and therefore diffraction of scattered electron waves is given by the Von Laue equations, which are considered as a substitute theory to the Bragg's law for diffraction. The interaction between the atoms of crystalline system and the incident electrons is most conveniently illustrated in reciprocal space.

Bragg's Law

Bragg's law was given by the English physicist W.H Bragg and his son W.L Bragg in 1913 to demonstrate X-ray diffraction (XRD) [2]. The Braggs were awarded the Noble Prize in physics in 1915 for their work. Despite the fact that Bragg's law was used first to interpret patterns of X-rays scattered by crystals, it has been sufficient when investigating the crystallographic structure of crystals with different kind of beams, e.g. neutrons, ions, electrons. As illustrated in figure 1.1, Bragg's diffraction takes place when a beam with wavelength similar to the interatomic spacing is scattered by the atoms of a well-ordered crystal with an inter-planar distance d. In order to achieve a constructive interference, the path difference between two waves must be equal to an integer multiple of the wavelength. Bragg's law is given by the equation:

$$2d\ sin\theta = n\lambda \tag{1.5}$$

Where, λ is the wavelength of the incident wave, n is an integer and θ is the angle of incidence.

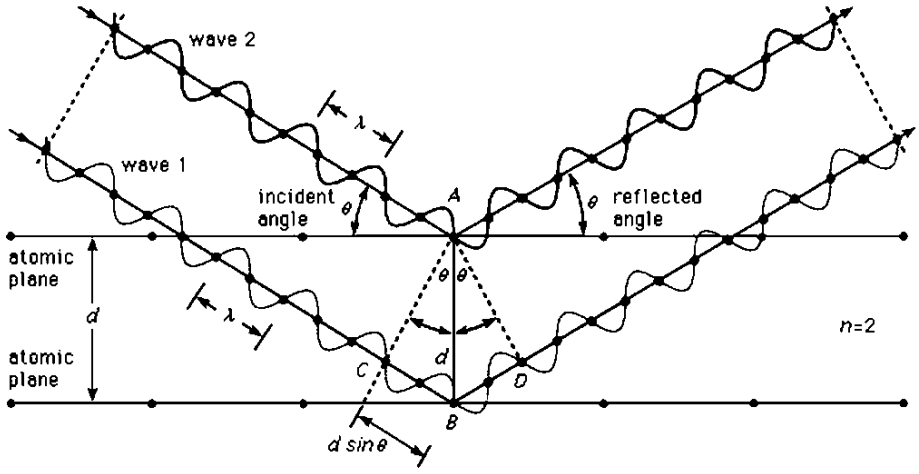

Fig. 1.1: Illustration shows Bragg's diffraction on crystal surface

From the perspective of Von Laue's theory, the difference between the wave vectors k_i and k_d must be equal to a reciprocal lattice vector, where:

$$\vec{k}_i - \vec{k}_d = \overrightarrow{\Delta k} \tag{1.5}$$

Here Δk is the scattering vector.

According to figure 1.2, the condition for constructive interference would be as follows:

$$d\,cos\theta + d\,cos\theta' = \vec{d}.(\hat{n} - \hat{n}') \tag{1.6}$$

$$\vec{d}.(\hat{n} - \hat{n}') = m\lambda \tag{1.7}$$

$$k = \frac{2\pi}{\lambda}\hat{n} \tag{1.8}$$

$$\vec{d}.\left(\vec{k}_i - \vec{k}_d\right) = 2\pi m \tag{1.9}$$

For 3D lattices

$$\vec{R}.\left(\vec{k}_i - \vec{k}_d\right) = 2\pi m \tag{1.10}$$

Or equivalently

$$e^{i(\vec{k}_i - \vec{k}_d).\vec{R}} = 1 \tag{1.11}$$

In crystallography, the reciprocal lattice of a Bravais lattice is the set of all vectors $\vec{G}$ such that

$$e^{i(\,\vec{G}.\vec{R})} = 1 \tag{1.12}$$

Therefore, the equation (1.5) can be defined as a reciprocal lattice vector such as:

$$\vec{k}_i - \vec{k}_d = \vec{G} \tag{1.13}$$

Where,

$$G_{hkl} = ha^* + kb^* + lc^* \tag{1.14}$$

In other words, this means that constructive interference will take place only if the scattered vector is a vector of the reciprocal lattice.

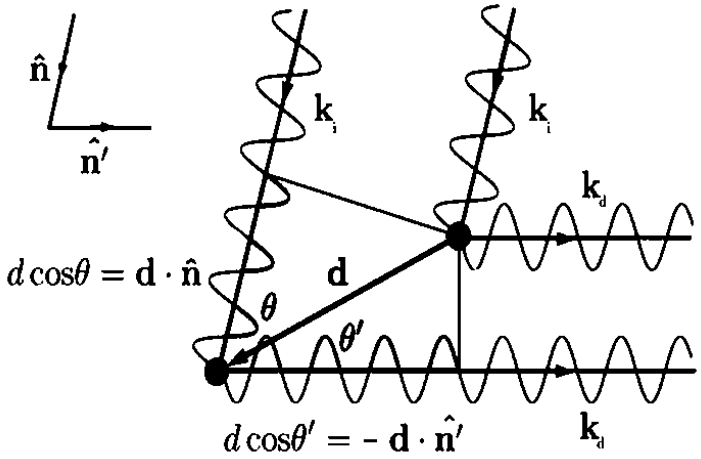

Fig. 1.2: Elastic scattering in terms of wave-vectors

Because of the short penetration depth of the low energy electrons of LEED [3], only the first few atomic layers contribute to the diffraction, this means that there are no diffraction conditions in the direction perpendicular to the crystal surface. As a result the reciprocal lattice of a surface can be described as a 2D lattice with rods extending perpendicular from each lattice point. Thus, the above equation is replaced by a two-dimensional equation such as:

$$k_i^{||} - k_d^{||} = G_{hk} = ha^* + kb^* \tag{1.15}$$

Where, $k^{||}$ presents the wave vector parallel to the sample surface.

The Ewald Sphere

The Ewald construction has been established as a great convenient approach to anticipate the occurrence of Von Laue's condition in equation (1.13), in which the scattering vector (momentum transfer) $\overrightarrow{\Delta k}$ must be a reciprocal lattice vector $\vec{G}$, and the energy conservation condition $|\vec{k}_i| = |\vec{k}_d| = |\vec{k}|$ for elastic scattering must be realized. This can be expressed graphically in reciprocal space by the requirement that a reflection will happen only if a reciprocal lattice point intersects with the Ewald sphere (see figure 1.3). The Ewald's

construction can be defined then as the sphere with radius $|\vec{k}|$ and origin at the center of the incident wave vector. By construction, every wave vector centered at the origin and terminating at an intersection between a rod and the sphere will then provide the Laue's law and thus produce an allowed diffracted radiation. As the incident energy is increased, the Ewald sphere radius will increase. Therefore, we will observe much bigger reciprocal space.

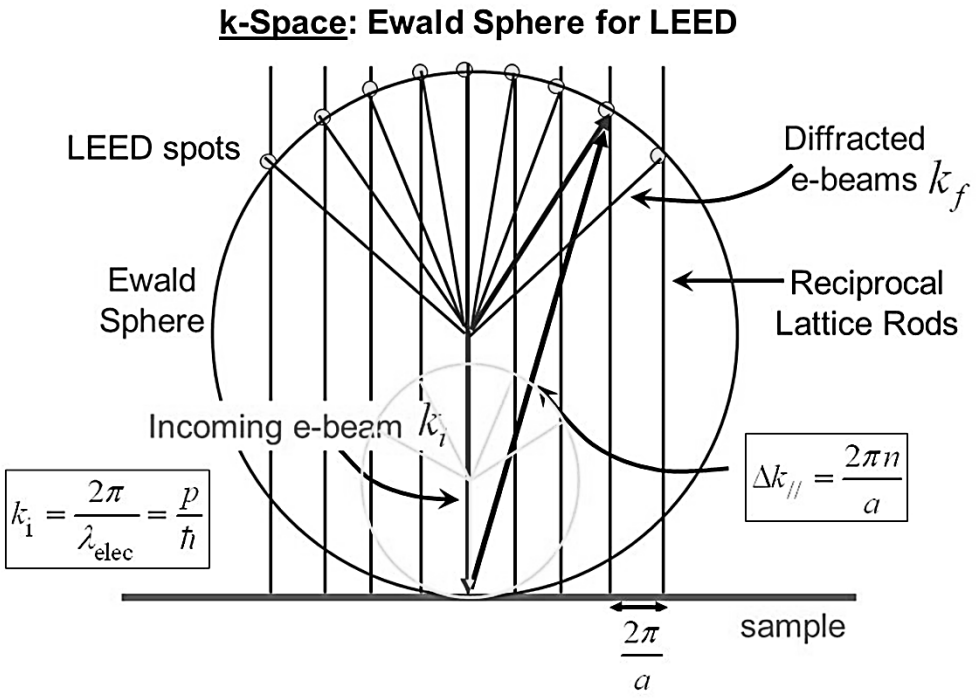

Fig. 1.3: Ewald sphere for elastic scattering for a 2D lattice

Two-Dimensional Periodicity and the LEED pattern

In Crystallography, the Bravais lattice, conceived by Auguste Bravais, is an infinite array of discrete points in three-dimensional space. Each point should have the same number of neighbors as every other point and the neighbors must always be found at the same distances and directions. In the case of diffraction from crystalline surfaces, the concept of infinite periodicity is accepted in two dimensions, but obviously not in the third dimension with direction perpendicular to the surface plane which is truncated by the existence of the surface itself. For 2D periodicity there are five two-dimensional lattices, as shown in figure 1.4.

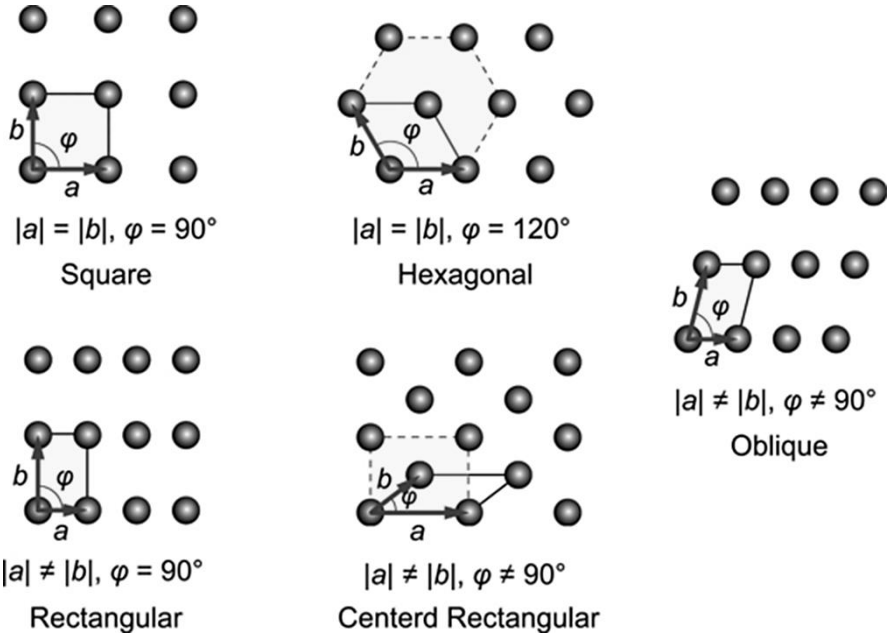

Fig. 1.4: Illustration shows two-dimensional Bravais lattices.

Interpretation of diffraction pattern

A two dimensional diffraction pattern can be illustrated in terms of the two dimensional reciprocal space. This allows identifying the real space lattice which should have generated the viewed diffraction pattern. The equations below present the relationship between the basis vectors in reciprocal and real space:

$$\overrightarrow{a_1}.\overrightarrow{a_1}^* = 2\pi \; ; \overrightarrow{a_2}.\overrightarrow{a_2}^* = 2\pi \tag{1.16}$$

$$\overrightarrow{a_1}.\overrightarrow{a_2}^* = 0 \; ; \; \overrightarrow{a_2}.\overrightarrow{a_1}^* = 0 \tag{1.17}$$

As a result of these equations $\overrightarrow{a_1}^*$ and $\overrightarrow{a_2}^*$ must be perpendicular to $\overrightarrow{a_2}$ and $\overrightarrow{a_1}$, respectively. Furthermore, in real space, as the length of the basis vector in any direction is increased, the reciprocal lattice vector will decrease. Figure 1.5 illustrates the corresponding reciprocal lattices for simple 2D structure of the (110) and (111) surfaces according to the equations above.

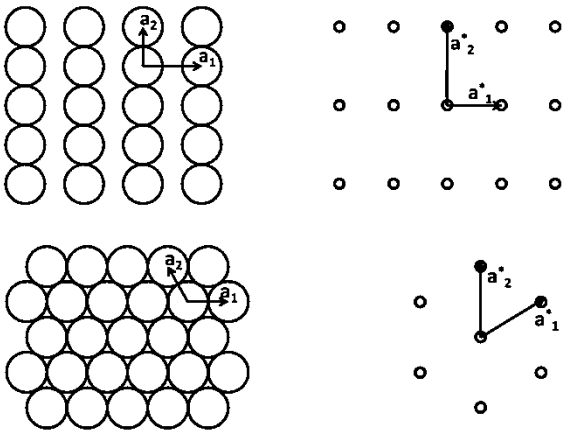

Fig. 1.5: Direct (left) and reciprocal (right) lattices for (110) and (111) surfaces of a simple face centered cubic crystal.

Superstructures

Superstructures (or superlattices) produce further spots in the LEED pattern. They could be due to an intrinsic reconstruction of the clean surface in which atoms at the surface form a different structure than that of the bulk or the existence of an ordered atomic overlayer (adsorbates). The nomenclature of the overlayer structure in terms of the underlying structure of the substrate is given by means of the relationship between the lattice vectors of the superstructure, b_1 and b_2, and the substrate, a_1 and a_2, is given by:

$$\overrightarrow{b_1} = m_{11}\overrightarrow{a_1} + m_{12}\overrightarrow{a_2} \tag{1.18}$$

$$\overrightarrow{b_2} = m_{21}\overrightarrow{a_1} + m_{22}\overrightarrow{a_2} \tag{1.19}$$

m_{ij} are coefficients of the superlattice matrix $M = [m_{11}\, m_{12};\, m_{21}\, m_{22}]$, which presents the translational vectors of the real space lattice of the overlayer in relation with that of the substrate. According to the numbers m_{ij} on whether they are integers, rational or irrational numbers, the superstructure is either labeled commensurate or incommensurate. Commensurate lattices can be seen in situations in which the superlattice generates a unit cell that is linked to the substrate lattice. While, incommensurate lattices present situations in which in the case of molecules weakly bonded to a substrate for example, the unit cell they maintain could be independent of the underlying structure of the substrate. There are two methods for characterizing the superstructure. In *the matrix notation*, the superstructure (substrate and overlayer) can be written as follows:

$$Substrate(hkl) - M - Overlayer \tag{1.20}$$

Here, (hkl) refers to the crystallographic plane of the substrate.

Wood notation [4] is a different notation alternative to the above matrix notation. This formulation is the simplest and most usually employed method for describing a surface crystallographic structure. Still, it only works if the two unit cells have identical symmetry (the angle between $\overrightarrow{b_1}$ and $\overrightarrow{b_2}$ must be the same as that between $\overrightarrow{a_1}$ and $\overrightarrow{a_2}$). In this situation, the superlattice can be labeled as:

$$Substrate(hkl) - i\left(\frac{b_1}{a_1} \times \frac{b_2}{a_2}\right) R\varphi° - \ Overlayer \tag{1.21}$$

In the notation above, i is either "p" (primitive) or "c" (centered) depending in how the unit cell of the overlayer is selected. Also, $R\varphi°$ is the rotation angle between the structure axis of the surface and the ad-layer.

Temperature effects

During LEED experiments it's very important to monitor the surface temperature which can affect the electron diffraction procedure [5]. As the temperature of the sample increases in a LEED experiment many changes can be seen on the diffraction pattern. The most observed changes are: decrease of the spots intensity and increase of the background intensity. These changes are due to the thermal vibrations of surface atoms (momentary shift of atoms from ideal periodicity). The loss of the intensity of spots is due to destructive interference between waves diffracted by disordered atoms, it is quantified by the Debye-Waller factor $\exp(-2M)$ [6]:

$$I = I_0 \exp(-2M) \tag{1.22}$$

The Debye-Waller factor can be expressed as:

$$M = \frac{3(\Delta k)^2 T}{2mk_B\theta_D^2} \tag{1.23}$$

Where, T presents the temperature, m the mass of the surface atoms, k_B the Boltzmann constant, and θ_D is the Debye temperature, which determines the rigidity of the lattice vis-à-vis of the vibration.

1.1.2 General Aspects of LEED Experiments

In principle the LEED experiment is pretty simple. A beam of mono-energetic electrons with energy in the range of 20 and 200 eV is focused onto a crystal surface at a fixed angle. The sample must be a well-ordered surface structure. Several diffracted beams of electrons with identical energy (elastic scattering) as the incident beam are produced as back-scattered electrons. Those electrons assist in the diffraction pattern. A typical four-grid LEED system is presented below in figure 1.6.

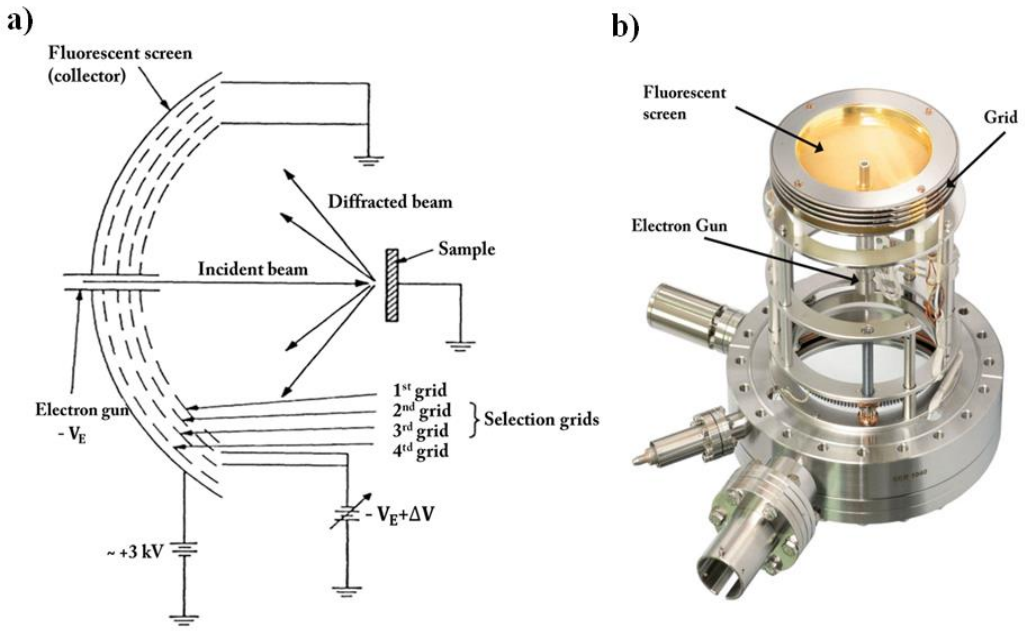

Fig. 1.6: a) Schematic of four-grid LEED, b) Image of the LEED instrument

The instrument parts of a LEED experiment are located in a vacuum chamber and consist of a hemispherical fluorescent screen (display system) and a fixed electron source (electron gun) adjusted along the middle of the screen. We should note that the electron beam used in the diffraction could be deflected by magnetic fields. As a result the beam becomes curved. Usually, an unavoidable magnetic field comes from the earth. This magnetic field may be canceled by building the vacuum chamber from a metal with high permeability.

The electron gun

The typical structure of an electron gun is illustrated in figure 1.7. Generally, heating a hot cathode will produce an electron-beam. The heating material is mostly a tungsten filament. There are two kinds of hot cathode. The first one is a directly heated cathode, where the tungsten filament plays the role of the cathode and provides the electron-beam. The second one is an indirectly heated cathode, in which the filament heats a separate metal cathode which emits the electrons. The produced electron-beam from the cathode should be accelerated to an anode. The energy range of the electrons, from around 20 to 200 eV for LEED, is established by the potential between the cathode and the anode. The gun lens system containing focus and shield allows the electron beam to stay in focus.

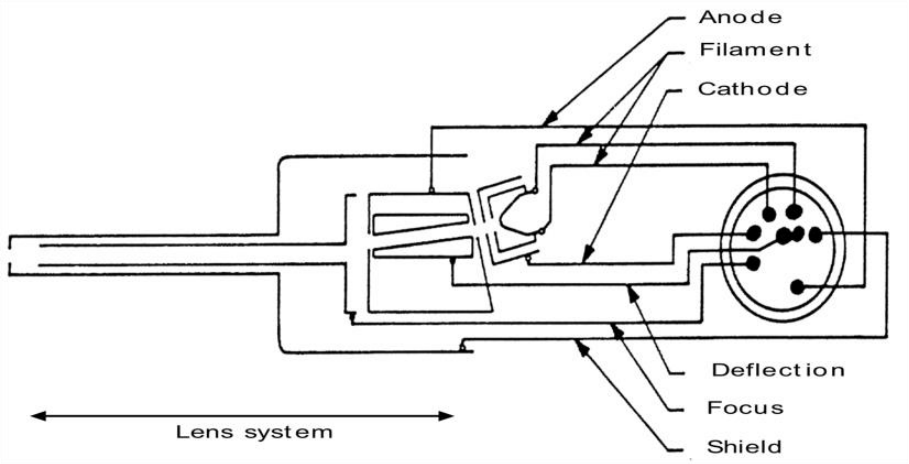

Fig. 1.7: simplified illustration of a LEED electron gun

The Display System

The electron beam diffracted from the crystal surface will impinge on a hemispherical fluorescent screen (collector). This mechanism has the benefit of creating a pattern that can be observed by eye (visual advantage). Preferably, the sample should be placed at the center of the hemispherical screen. With this adjustment, diffraction beams coming out from the sample travel radially towards the collector. Generally, the collector is metallic and coated with a fluorescent material. The metallic aspect of the screen is required in order to allow the electrons to be conducted away, preventing the charging effects [7]. It has to be biased positively to 3-5 kV in order to obtain a final acceleration of the coming electrons. In addition to elastic scattering, inelastic scattering also takes place at the surface of the crystal [8].

To solve this problem, a series of three or four hemispherical grids placed just before the fluorescent screen will block the inelastically scattered electrons from reaching the collector.

The first grid is generally grounded so that the diffracted electrons travel in field free space. The second and third grids are maintained at a potential a few volts below the incident electron beam. As a result, electrons which have lost a few volts (inelastic electrons) cannot reach the collector because they have insufficient energy to cross through these grids. The fourth grid is normally grounded, to isolate the collector potential from the energy selection potential.

1.2. Auger Electron Spectroscopy (AES)

Auger electron spectroscopy (AES) is a common analysis tool in surface science. It is used mostly to:

- Verify the cleanliness of a newly prepared surface under UHV conditions.
- Investigate the surface chemical composition
- Study the surface ad-layer growth mode

Typically, AES is an electron core-level spectroscopy and it can be used for many surface materials and all elements except for hydrogen and helium as at least two electron shells are needed.

1.2.1 General Aspects of AES Theory

Auger electron spectroscopy (AES) is based on the Auger effect discovered by Auger in 1923 [9]. The principle of the Auger process can be explained by means of the diagram of electron energy levels as illustrated in figure 1.8. Basically, the primary ionizing electron can generate an initial hole by ionization of a deep core atomic shell (K in figure 1.8). Then, the primary electron and core electron will be ejected. An electron from an energetically higher shell will replace the emitted core level electron. Atomic relaxation can be achieved by the emission of an x-ray photon (fluorescence phenomena [10]), or there can be another process where the de-excitation could be radiation-less where another electron gain the extra energy and is emitted from the atom, it is the Auger electron. The ejected Auger electron can be characterized by a kinetic energy that corresponds to differences in core-level energies. Therefore, measurement of the Auger kinetic energy can be used to characterize the investigated surface elements. It has been demonstrated that for heavier elements, x-ray fluorescence relaxation process becomes dominant over the Auger process [11].

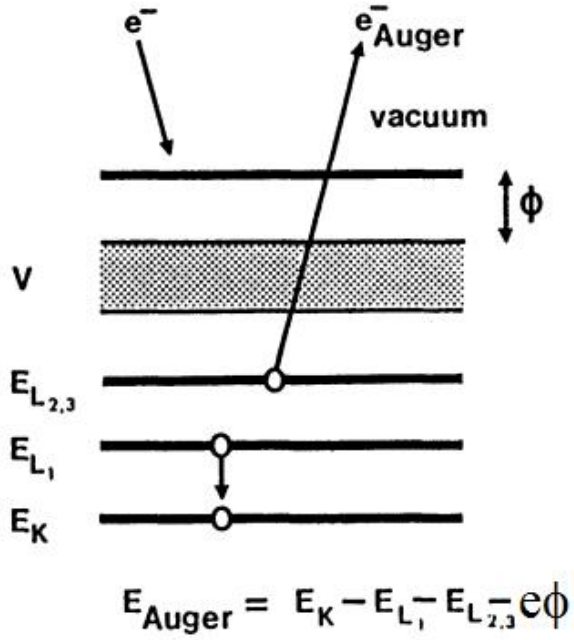

Fig. 1.8: Illustration of the energy level diagram showing the origin of the Auger electron for a $KL_1L_{2,3}$ transition.

The nomenclature of Auger transitions corresponds to the atomic shells associated with the process (see figure 1.8). For single energy levels, if the primary beam ejects electron from the K shell, the Auger transition will be maintained by an electron from the L shell, such an Auger transition is called a $KL_1L_{2,3}$ transition. The measurement of the characteristic energy of an Auger emitted electron can be illustrated by the following equation:

$$E_{kin} = E_K - E_{L_1} - E_{L_{2,3}} - e\phi \qquad (1.24)$$

E_K, E_{L_1} and $E_{L_{2,3}}$ are the bonding energies of the K, L_1 and $L_{2,3}$ atomic shells. ϕ is the work function.

The source energy of the primary electron beam used during AES experiment is typically 5 keV. In this case, electrons have a short mean free path in a solid resulting in an extreme surface sensitivity [12].

1.2.2 General Aspects of AES Experiment

The standard AES equipment consists of an electron gun irradiating the sample surface, and an electron energy analyzer to collect, and analyze the emitted Auger electrons. The most popular analyzers are the cylindrical mirror analyzer (CMA) [13], and the concentric hemispherical analyzer (CHA) [14]. Typically as illustrated in figure 1.9, CMA analyzers are composed of two concentric cylinders, the inner cylinder at ground and the outer cylinder at a negative potential. Electrons arriving at the CMA analyzer will have been focused through the concentric cylinders. The transmitted electrons are then collected by an electron multiplier. During AES experiment, the energy resolution and accurate electron detection is highly affected by the sample/analyzer horizontal position and separation.

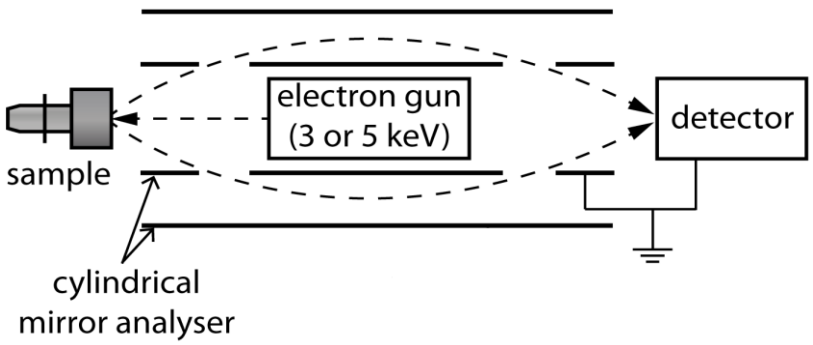

Fig. 1.9: Simple schematic illustration of an AES experimental setup using a cylindrical mirror analyzer (CMA).

The detected Auger electrons by the electron multiplier are presented as a function of energy variation across predefined values. Auger spectra are generally produced by two modes. The counting mode $N(E)$, can be plotted as shown in figure 1.10. But, because of the small Auger signals that can be perturbed by the noise of the secondary electron background spectrum, AES is commonly performed in the derivative mode $\frac{dN(E)}{dE}$ in order to eliminate the background noise and then highlight only the Auger signals. The derivative mode is achieved by modulating the electron collection current via the application of a small voltage to the spectrometer energy (sinusoidal energy modulation):

$$v = v_o \sin \omega t \tag{1.24}$$

As a result, the collection current can be given as follows:

$$I(V + v_o \sin \omega t) = I_o + I'(V + v_o \sin \omega t)) + O(I^{"}) \tag{1.25}$$

Thus, detecting the signal at a given frequency (ω) will give a value for I' which is related to $\frac{dN(E)}{dE}$.

After recording the AES spectra, in order to analyze and identify the chemical nature of each Auger peak produced we use a handbook of Auger electron spectroscopy [16] in which Auger energies are tabulated and presented as a function of each element. Our AES spectra results are recorded using a CMA analyzer with a primary electron beam of 3 keV, an emission current of 5 μA and the Auger electrons are collected in the derivative mode.

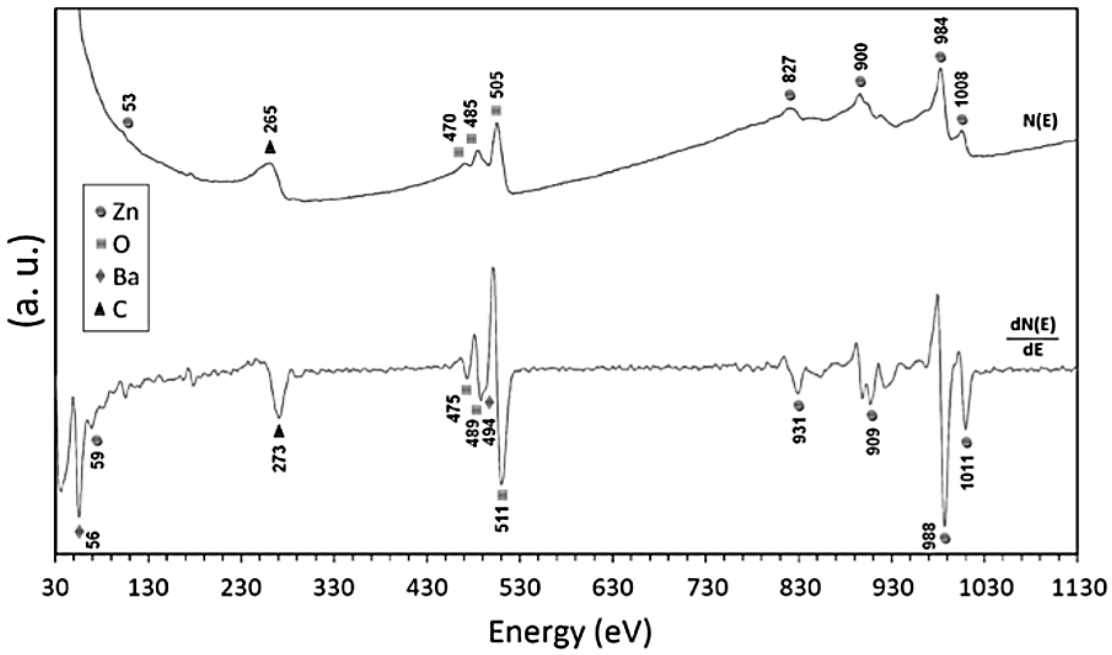

Fig. 1.10: Auger spectra taken from [15]. The upper spectrum is performed in counting mode, and the derivative mode is presented in the lower spectrum. The most benefit of using the derivative mode is that background slope is removed.

1.3. Scanning Tunneling Microscopy (STM)

Scanning tunneling microscopy (STM) is an extremely powerful instrument developed at the IBM Zurich Research Laboratory in 1981 by Gerd Binnig and Heinrich Rohrer [17]. Five years later, these two researchers were awarded the Nobel Prize in physics for their pioneering work. After that STM quickly proved to be one of the most promising experimental techniques for studying and investigating surface materials.

Today, STM has three main applications:

- Imaging instrument to study the topographic aspects of a given surface starting from several µm down to a highly atomic resolution (nm).
- Spectroscopic tool to analyze the electronic properties of the surface (scanning tunneling spectroscopy).
- Lithographic device to customize surfaces on the nano-scale [18].

The STM principle is very simple, a sharp metal tip (usually from tungsten) is brought close to a given metallic or semi-metallic sample and a small bias potential U is applied between the tip and the surface (see figure 1.11). As a result, electrons can "jump" or "tunnel" between the two electrodes. This mechanism is a purely quantum mechanical phenomenon and it is known under the name of tunneling effect.

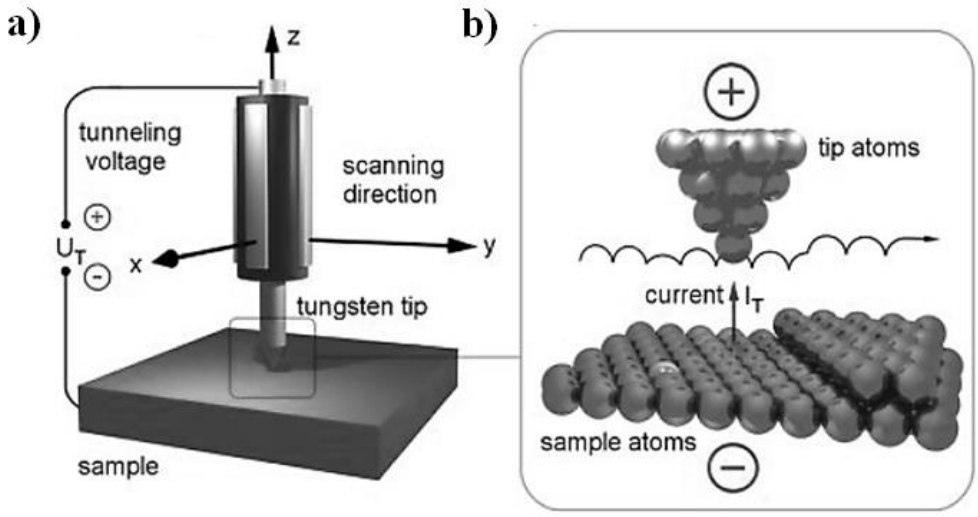

Fig. 1.11: Schematics of STM work principle on (a) macroscopic scale (b) atomic scale in the constant current mode.

Here, the tunneling current is the most important physical value measured in the STM experiment. Based on this value the STM can be used in two modes (see figure 1.12). The constant current mode is the commonly used one. In this mode, the tip scans over the sample and a regulation system (feedback loop) maintains a fixed current parameter by modifying the tip/surface separation (z). The changes of the tip height z are recorded and an image of the scanned area of the sample can be created by plotting z(x,y) in real space. The second mode is the constant height mode, the tip will scan the sample at a constant height (z) and this time the tunneling current is monitored instead of the tip height. The measured current as a function of lateral position presents the scanned surface area topography. Here, the feedback loop should be deactived. In our STM experiments, all the scannings were done in the constant current mode, given the fact that the constant height mode is very risky for the tip and should be used only for atomically flat surfaces.

STM experiments can be performed in air [19] or in a vacuum chamber [20], at high temperature [21] or at low temperature (lower than 80 K) [22]. As stated before, since the tunneling current is the most important measured parameter in STM, the conductivity of the sample is an essential condition to carry out such experiments.

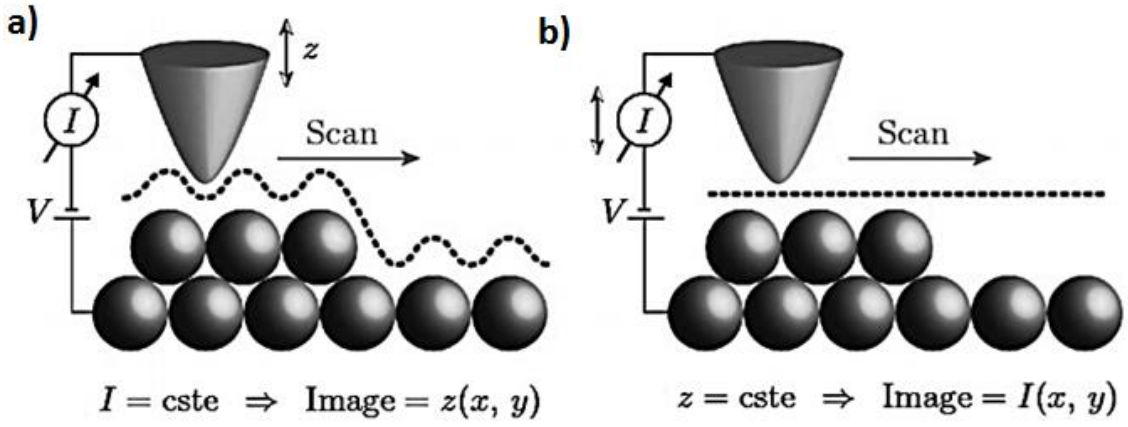

Fig. 1.12: Schematic of STM operating modes (a) constant current (b) constant height.

1.3.1 General Aspects of STM Theory

The Tunneling Effect

The principle of electron tunneling was first proposed by Giaver [23]. Electron tunneling takes place when two electrodes (tip/sample) come into near contact, separated by an

insulating barrier such as vacuum, air or liquid. Studying this effect under quantum theory perspective, the electrons can be seen as a wave function. If the tip and sample are close enough, their wave functions can overlap. The application of a bias voltage will result in an offset between the two electrodes Fermi levels generating a current in which its direction depends on the polarity of the applied voltage.

The theoretical description of the STM tunneling process was given by Tersoff and Hamann [24]. In this theory, the tip, the vacuum and the sample are considered as a single system in which each subsystem interact strongly with the others. Here, the tip and sample potential energies are inserted into a time dependent Schrödinger equation:

$$i\hbar\frac{\partial\Psi_\mu}{\partial t} = (T + \mathrm{U}_S(t) + \mathrm{U}_T(t)\,)\Psi_\mu \tag{1.25}$$

Where,

T corresponds to the kinetic energy, U_S and U_t are sample and tip potential energies, respectively. Ψ_μ is the wave function of the complete system and $\hbar$ is the Planck constant.

Using,

$$\Psi(x,t) = \Psi(\mathrm{x})\exp(\tfrac{-iEt}{\hbar}) \tag{1.26}$$

As a solution for the wave function, the transition probability of an electron tunneling between μ and v states can be given as follows:

$$P_{\mu v} = \frac{2\pi}{\hbar}\left|M_{\mu v}\right|^2\delta(\mathrm{E}_v - \mathrm{E}_\mu) \tag{1.27}$$

Here, $M_{\mu v}$ presents to the matrix element of the transition probability. Using the theory of Bardeen [25] in which each subsystem is supposedly weakly interacting, the matrix element is presented as follows:

$$M_{\mu v} = -\frac{\hbar^2}{2m}\int \overrightarrow{dS}(\,\Psi_v{}^*\nabla\Psi_\mu - \Psi_\mu\nabla\Psi_v{}^*) \tag{1.28}$$

Where, m is the mass of the electron and *dS* is the surface element.

Using the density of states (DOS) (ρ_S, ρ_T) of the sample and tip near the Fermi level, the tunneling current can be written as:

$$I = \frac{4\pi e^2}{\hbar}\, U_b \rho_S(E_F)\rho_T(E_F)\, |M|^2 \tag{1.29}$$

U_b is the applied bias potential between the two electrodes. Considering the classical problem of a single electron tunneling through a 1D potential barrier, the solution of the Schrodinger equation is given by:

$$\Psi(\mathrm{x}) = \Psi(0)e^{-kd} \tag{1.30}$$

Where d is the tip/sample separation distance. As a result, the transmission probability of an electron can be written as:

$$|M|^2 \sim |\Psi(0)|^2 e^{-2kd} \tag{1.31}$$

Here, k is the decay coefficient of the wave function and is given as a function of the tunnel barrier height ϕ as follows:

$$k = \frac{\sqrt{2m\phi}}{\hbar} \tag{1.32}$$

In their theory, Tersoff and Hamann describe STM tip model by means of only s-like wave functions which can be seen as a spherical potential with a radius R. Supposing a point-like tip (atomic apex) where usually $\rho_T \approx const$ and that only the sample electronic states at the center of the tip curvature contribute to the tunnel effect, the tunneling current can be written as:

$$I \sim U_b \rho_S(E_F) e^{-2kd} \tag{1.33}$$

The tunneling current here is in function of the bias potential U_b and the density of states ρ_S near Fermi level. For a typical metal ($\phi \sim 5\ eV$) and from the exponential dependence on the

separation d, one can conclude that the current will decrease by a factor of 2 as the distance is increased by 0.2 nm between the electrodes. This demonstrates that the tunneling current is very sensitive to the variation of the tip-sample separation, which also explains the STM instrument vertical high spatial resolution.

1.3.2 General Aspects of STM Experiment

Mainly, as can be seen from the figure 1.13, the STM consists of 3 main parts: the piezoelectric driver which drives the movement of the scanner in three dimensional space (x,y,z), the preamplifier circuit for the tunneling current and the tip which plays a huge role on the STM topographic and spectroscopy quality. Furthermore, we should note that it is necessary to have a vibration isolation system [26] which will help to eliminate most of the external mechanical perturbations and also a coarse positioning device [27] which will approach the tip to the surface.

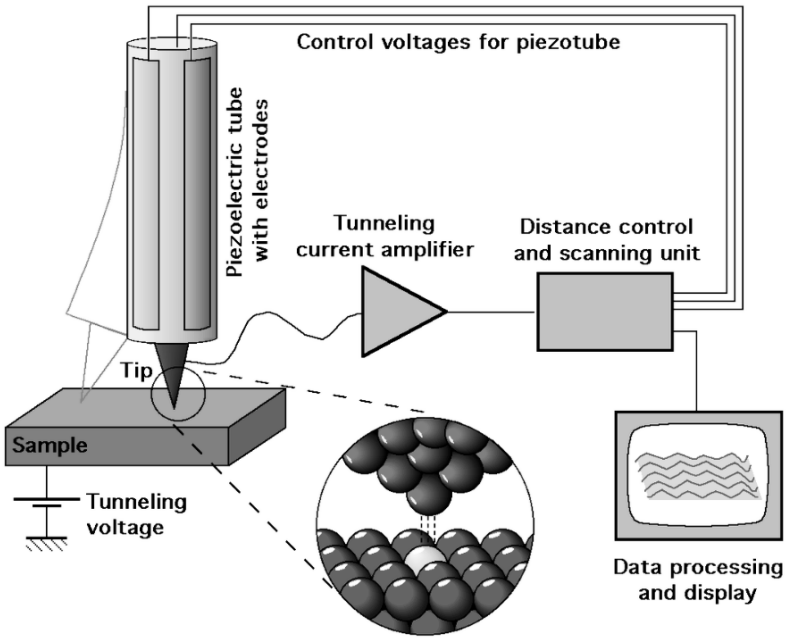

Fig. 1.13: A simplified schematic of an electronic network of STM

Piezoelectric driver

The extremely small movements needed to scan a surface using a sharp atomic wire (tip) can be conducted using piezoelectric materials. A piezoelectric material is a special material that elongates or compresses when certain voltages are applied across the crystal. Usually,

piezoelectric scanners are polycrystalline solids based on ceramics and the most used one is lead zirconate titanate (PZT) $Pb[Zr_xZr_{1-x}]O_3$ [28].

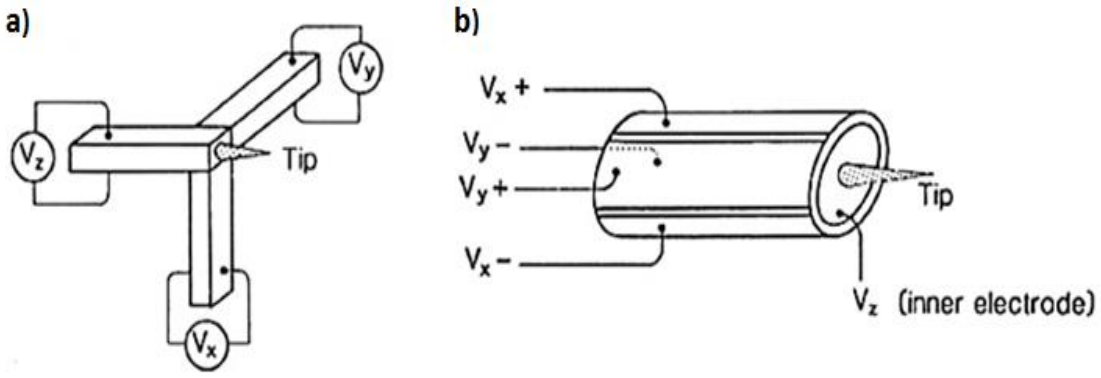

Fig. 1.14: Drawing of a) tripod scanner b) tube scanner

In STM instruments there are mostly two types of piezoelectric drivers, the XYZ tripod (figure 1.14a) and the tube scanner (cylindrical tube) (figure 1.14b). The tripod was used in the first made STM by Binnig and Rohrer, it has three independent displacements of orthogonal axes (x,y,z), while in the tube scanner proposed by Binnig and Smith [29], few years later, four external electrodes were used. By applying potentials to the various electrodes, a mechanical three dimensional movement is achieved. Their piezoelectric scanner has a response of 5nm/V in each orthogonal direction.

Assuming that the same equal and opposite voltages are applied on the opposite piezo electrodes (-X; +X) or (-Y; +Y) we can measure the X and Y movement /volt using the equation given below [30]:

$$\Delta X = 2d_{31}V_X L/(O_D - I_D) \tag{1.34}$$

Where,

ΔX presents the scanner piezo response along X-axis, d_{31} is the transverse piezoelectric coefficient (m/V), L presents the length of the cylindrical scanner, V_X is the applied voltage along X-axis., I_D corresponds to the inner diameter of the cylindrical scanner and O_D is the outer diameter of the cylindrical scanner.

If we take for example: d_{31}= -171 10^{-12} m/V for PZT5A [31] and applying V_X = 1 V

With, L =20 mm, I_D= 5 mm and O_D= 6 mm

Therefore, if we apply a voltage of 1V we anticipate a response in the piezo tube scanner in the X direction of **6.8 nm/V**.

STM electronics

STM control and data acquisition electronics consist of common elements such as: a high-gain low-noise current amplifier [32], a proportional-integration (PI) digital feedback controller [33] and a set of high-voltage amplifiers that control the piezo-tube scanner. Electronics are needed to monitor the current and digitize this information into a form that we can present as an STM topographic image. STM software such as MATRIX from OMICRON (used in this thesis) is also of great help to control and handle various STM instrumentation and parameters.

Tip Preparation

During STM scanning, a high quality sharp tip is essential to achieve good STM images or spectroscopic signals. In this manner, taking great care at the tip preparation is an extremely important experimental factor in STM before starting the actual experiment. Mostly, metallic materials are used as a wire to make the STM tip. Despite the huge selection options only a limited number of metals are really ideal for such a task. Based on the experiments of Chen [34], only d-band metal tips can achieve atomic resolution. If the tip is made of noble metals (Cu, Ag, Au) or alkali metals, high resolution cannot be obtained.

On the other hand, tungsten (W) is the most used material for tip fabrication because of its strong mechanical properties and d-band electronic structure [35]. As shown in figure 1.15, using W tip including a d_{z^2} dangling bond could behave like a filter since its charge-density distribution is narrower than that of an s-state. As a result, clearer atomic resolution features can be obtained.

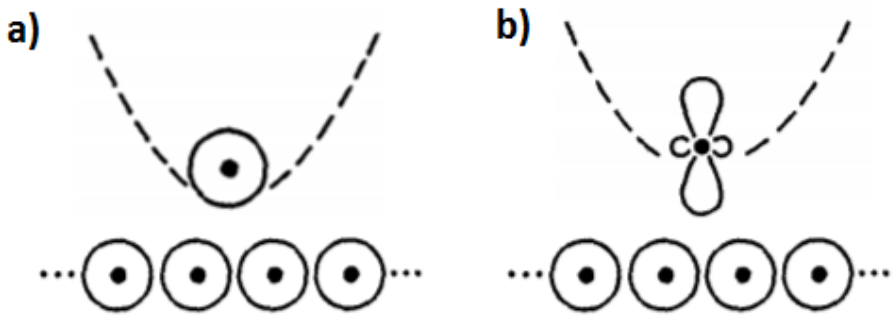

Fig. 1.15: Simple drawing of a tip with a) s state b) d_{z^2} state

Generally, the tungsten tips are prepared by electrochemical etching and the basic idea here is to dip a small solid W wire into an hydroxide ion solution (electrolyte). As a result, a dissolution reaction will start producing a sharp W tip shape at the end. It is possible to fabricate tungsten tips under both alternating current (AC) and direct current (DC). For our tip preparation, a tungsten wire is immersed in a sodium hydroxide electrolytic solution (Na^+, HO^-) which acts as an anode. The second electrode, a stainless steel rod used as the cathode is immersed in this solution. A potential is applied between these two electrodes (see figure 1.16). During this process the following chemical reactions take place:

$$W_{(s)} + 8HO^-_{(aq)} \rightarrow WO^{2-}_{4(aq)} + 4H_2O_{(l)} + 6e^- \quad (1.35)$$

$$6H_2O_{(l)} + 6e^- \rightarrow 3H_{2(g)} + 6HO^-_{(aq)} \quad (1.36)$$

$$W_{(s)} + 2HO^-_{(aq)} + 2H_2O_{(l)} \rightarrow WO^{2-}_{4(aq)} + 3H_{2(g)} \quad (1.37)$$

From these reactions we can conclude that the tungsten metal undergoes an oxidative dissolution to become tungstate anions which are soluble in water. Furthermore, reduction of water and formation of hydrogen gas ($H_{2(g)}$) is also expected in which small bubbles will be produced subsequently. Once the etching is done, it is important to clean the tip immediately by washing it with distilled water. To verify if the etching process has been successful, the

freshly made tungsten tip is observed under an optical microscope to check the length and the tip head shape.

For our tip preparation, we did use AC and DC voltages for the etching process. Generally, an AC applied voltage will produce a longer taper length which is more vulnerable to mechanical vibrations resulting then in a bad STM measurements. In fact, when using AC voltage (10V applied during 150 ms with a separation of 2.5 s) the amount of hydrogen bubbles increases which will cause the etching to extend above the air/solution interface [36]. On the other hand, a DC voltage (3V) produces better, sharper W tips. It is recommended to use lower DC voltages since the high chemical reaction rate can etch the bottom of the wire even before a good necking effect is completed [37].

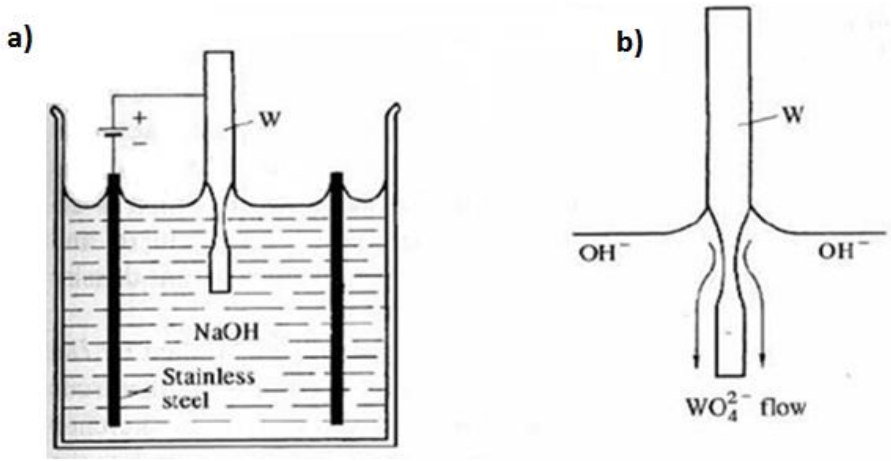

Fig. 1.16: Illustration of an electrochemical station showing the experimental tip-etching method where a) small tungsten wire is immersed in NaOH solution b) beginning of the drop-off mechanism.

Before using the tip in actual STM experiments, it should be degassed in UHV by indirect heating in order to remove any contaminants (H_2O, O_2, and tungsten oxide WO_3) that cannot be removed by rinsing in water or ethanol. Generally, other cleaning methods [38] could be used for the etched tungsten tip such as: Ar-ion sputtering, heating by electron bombardment or applying a low reverse voltage. The process of cleaning the etched tip before starting the actual scanning is very important because any contaminants or oxide can cause an unstable tunnel junction which leads to irregularities in STM topography and spectroscopy. After the

cleaning, in order to make sure that the STM tip is suitable for scanning experiment, usually a scanning tunneling spectroscopy (STS) test is performed as a sign of the presence of any contamination on the tip. When using a metallic sample, if the W tip is oxidized the STS data will show a gap-like electronic structure instead of the metallic tunnel junction, i.e. the I–V curve would not be linear.

1.4. Scanning Tunneling Spectroscopy (STS)

Scanning tunneling spectroscopy (STS) can provide complementary information to the topographic profile obtained by STM imaging. With STS the local electronic structure of a surface can be accessed. Most of the STS experiments are performed in $I(U)$ mode in which the tip/sample separation is kept constant by turning the feedback controller off. Then, the bias voltage is ramped over the chosen limits from U_{set} to $-U_{set}$ and the tunneling current $I(U)$ is recorded during the voltage ramp. Theoretically, Tersoff and Hamman [24] (assuming that the tip density of states (DOS) is constant) suggested that the ratio of the differential conductivity dI/dU to the total conductivity I/V should be proportional to the local density of states of the investigated surface:

$$\frac{dI}{dU} \propto \rho_s(E_F - eV) \tag{1.38}$$

Another mode to perform STS is $I(z)$ spectroscopy. Here, starting from the tunneling current in equation (1.33) we can evaluate the apparent barrier height as follows:

$$\phi = \left[\frac{1}{1.025}\frac{d\ln(I/U_b)}{dz}\right]^2 \tag{1.39}$$

The measured value of ϕ presents the work function of the surface. As a result, it can be used to characterize the chemical nature of the sample surface.

1.5. Synchrotron Radiation

Synchrotron radiation is an electromagnetic radiation produced mainly in synchrotrons, which are sophisticated instruments built to perform physics experiments. Their main objective is to accelerate charged particles up to relativistic speeds, i.e. the particle velocity become closer to the speed of light. The type of charged particles used in synchrotrons is generally electrons, which emit radiation more easily than the more massive protons [39]. Accelerating radially,

the electrons produce electromagnetic radiation, and they do so as they are focused around curved paths by magnetic fields using bending magnets, undulators or wigglers [40]. These magnetic devices bend, undulate or wiggle the direction of the electrons as long as they turn around the storage ring of the synchrotron. As a result, the electrons emit an intense radiation. The electrons which orbit around the storage ring and produce the light beam are at first provided by an electron gun. Here, a high voltage cathode considered as an injection system is heated under vacuum, giving the electrons. A linear accelerator is used to increase the kinetic energy of the primary emitted electrons by passing groups of these electrons called "bunches" through a metallic chamber that contains confined resonant electromagnetic waves called radiofrequency (RF) cavity [41,42]. Electrons going through the RF cavities sense the electromagnetic force which gives them a push forward into the circular accelerator (booster). Before transferring the electron beam to the storage ring, boosters accelerate the electrons using dipole bending magnets. In the storage ring, big electromagnets (bending magnets) [43] are used to change the path of the electron beam in the zone between the straight sections. Anytime the path of the electrons bends, they decelerate, and as a result they produce synchrotron radiation. On the other hand, insertion devices (undulators/wigglers) are inserted in straight sections between the bending magnets. They also generate synchrotron radiation (see figure 1.17a for visual illustration of the work principle of synchrotrons).

As can be seen on figure 1.17b, undulators/wigglers consist of a sequence of magnets of opposite polarity (dipole magnets) in a row. Electrons going through such device undergo a magnetic field of alternating polarity which makes them follow a wavy path. So for N poles, the quantity of photons generated is enhanced by the factor N, giving off more x-ray or UV radiation than in the case of a single bending magnet is used. Radiation polarization is possible, i.e. if the electrons wavy trajectory is confined to a plane the radiation will be linearly polarized. If the oscillation of the electrons is helical the radiation will be circularly polarized.

The main difference between undulators and wigglers is that the deflections caused by an undulator are small enough that radiations emitted at each of the poles can then overlap and interfere with the photons produced at the other poles. This generates a much more focused, brilliant beam of radiation.

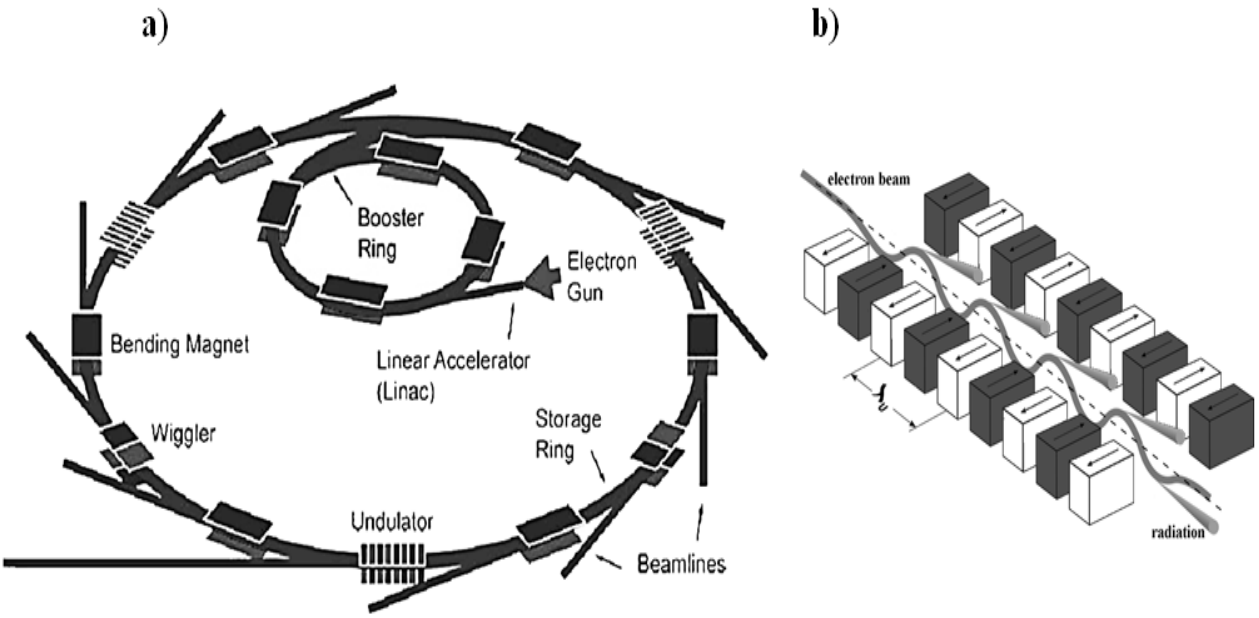

Fig. 1.17: Schematic illustration of a) synchrotron facility showing the key components to generate synchrotron radiation, b) undulator with magnetic poles of alternating polarity. The ring parameters of synchrotron SOLEIL are: linear accelerator "Linac" (100 Mev), the booster (2.75 GeV), the ring (2.75 GeV) with 354 m circumference [44]

1.6. Extended X-Ray Absorption Fine Structure (EXAFS)

EXAFS is a powerful technique for investigating the atomic structure of elements in a material. The EXAFS is integrated from x-ray absorption spectroscopy (XAS) technique which is based on measuring the x-ray absorption coefficient $\mu(E)$, which characterizes the quantity of x-rays absorbed as a function of x-rays energy. By changing the energy of the incoming photons, a spectrum is produced as shown in the figure 1.18. Typically, $\mu(E)$ smoothly diminishes as the energy increases which means the x-rays become more penetrating.

The x-ray absorption spectrum is generally composed of two regimes: x-ray absorption near-edge structure (XANES) and extended x-ray absorption fine-structure spectroscopy (EXAFS). Even if the two regimes share the same physical cause (XAS), the interpretations and conclusions extracted from both are different [45]. XANES in one hand is more sensitive to oxidation state and coordination environment of the absorbing atom, while on the other hand EXAFS is more convenient to measure the inter-atomic distances, coordination number of the surrounding atoms and the nature of the neighbor atoms around the excited atom.

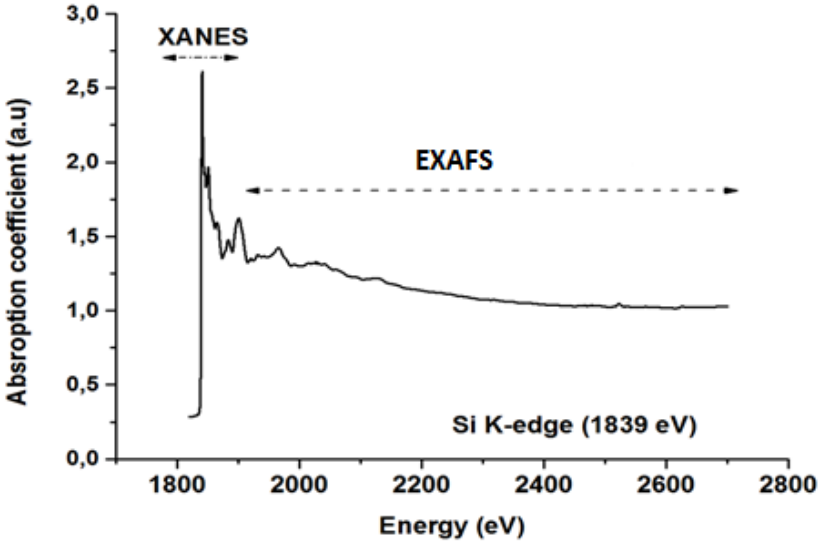

Fig. 1.18: X-ray absorption spectrum of Silicon wafer showing the near edge (XANES) and extended (EXAFS) regions.

1.6.1 General Aspects of EXAFS Theory

As explained in the previous paragraph EXAFS is a result on the x-ray photoelectric process, in which an x-ray photon incident on an atom within a material is absorbed and releases a photoelectron. The photoelectron can be seen as a wave radiating and interacting with all the neighbors of the absorbing atom, with a wavelength λ given by:

$$\lambda = \frac{h}{p} \tag{1.40}$$

Where, p is the momentum of the electron and h is Planck's constant.

The photoelectron wave can scatter and interfere constructively or destructively with the backscattering waves created by the surrounding atoms when returning to the absorbing atom. This interference leads to a relation between the photon energies and the x-ray absorption probability $\chi(k)$, which is related to the X-ray absorption coefficient. If it is correctly interpreted the $\chi(k)$ oscillations give structural information about the surrounding atoms.

Based on the model in which the photoelectron is a sinusoidal plane wave, the probability of absorption could be given as follows [46]:

$$\chi \propto sin(2Ak) \tag{1.41}$$

Where, A is the distance between the excited atom and scattering ones.

Giving that

$$p = \hbar k \tag{1.42}$$

$$T = \frac{p^2}{2m_e} \tag{1.43}$$

The kinetic energy of the photoelectron is given by the difference between the energy E of the incident photon, less the binding (ionization) energy, which we call E_o:

$$T = E - E_o \tag{1.44}$$

$$k = \frac{1}{\hbar}\sqrt{2m_e(E - E_o)} \tag{1.45}$$

Where, k is the wave number and A is the distance between the absorbing atom and the surrounding atoms.

EXAFS equation

The EXAFS oscillations can be defined by an equation generally called the EXAFS equation [47]:

$$\chi(k) = \sum_R S_0^2 N_R \frac{|f(k)|}{kR^2} \sin[2kR + \delta(k)] e^{-2R/\lambda(k)} e^{-2k^2\sigma^2} \tag{1.46}$$

Where,

$f(k)$ and $\delta(k)$ are the backscattering amplitude and the phase shift of the surrounding atoms.

R is the distance to the surrounding atoms.

N is the coordination number of surrounding atoms.

σ^2 presents the thermal motion or structural disorder. Typically $0.003 \leq \sigma^2 \leq 0.03$.

S_o^2 is the amplitude reduction factor generally varies between 0.7 and 1.0.

$\lambda(k)$ is the mean free path of the emitted photoelectron. This term guarantees the local behavior of EXAFS.

1.6.2 General Aspects of EXAFS Experiment

In order to perform EXAFS experiment, we need to select an x-rays domain with energies able to excite the investigated atom. For example to study a system with silicon atoms, a range between 1800-2400 eV can be used. To achieve this, a monochromator is required. This device based on diffraction from crystals can ensure that only x-rays with the good energy are used to probe the sample. The type of the materials used for the monochromator and their geometrical considerations ensure that only a range of usable energies will reach the sample. The experiments presented in this manuscript were carried out on the LUCIA beamline [48] of the synchrotron SOLEIL facility. The schematic view of LUCIA beamline is given in figure 1.19.

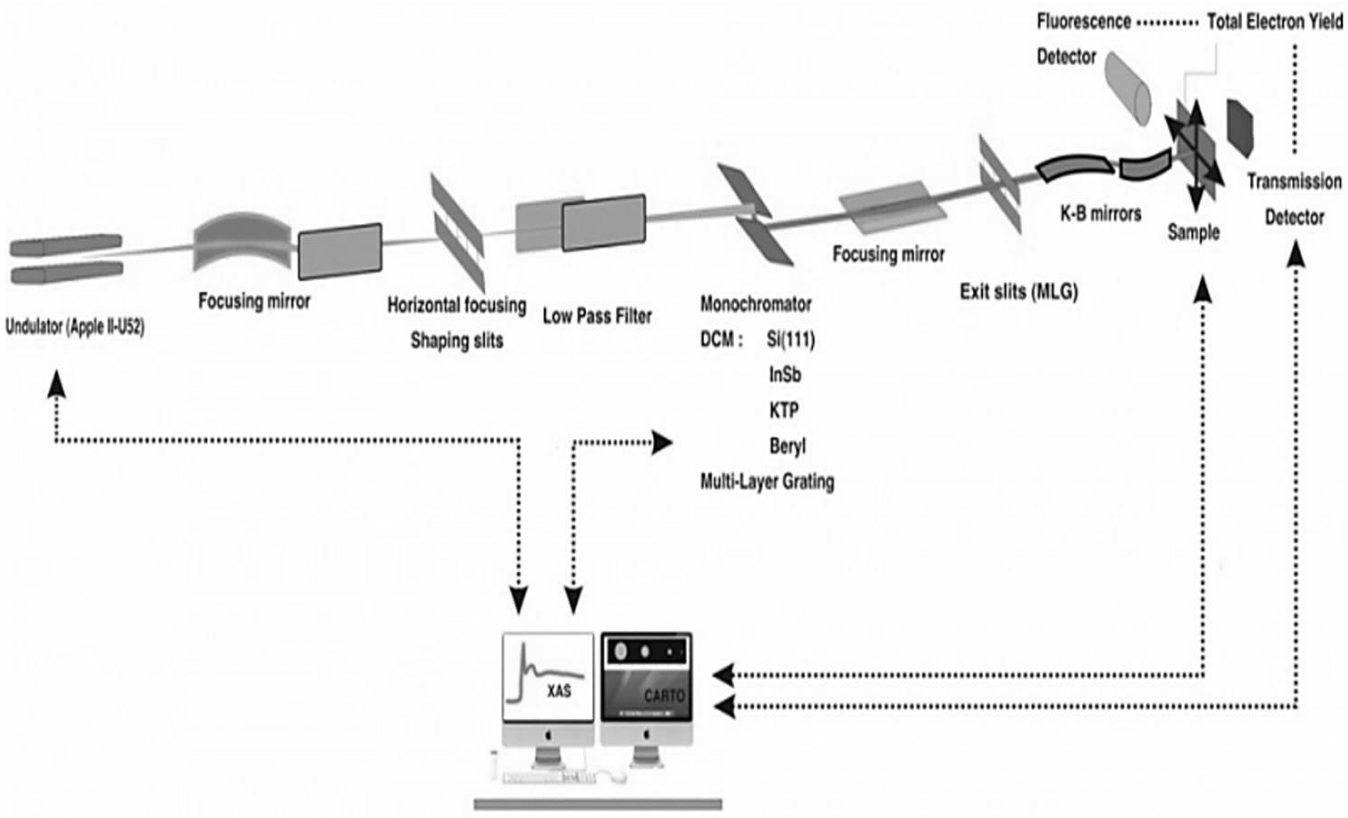

Fig. 1.19: Schematic view of LUCIA beamline [48] at SOLEIL which can generate photons in the energy range between 0.8 and 8 KeV. Several double crystal monochromator can be used to obtain various energy domains and a focusing system in "Kikpatrick-Barz" (KB) configuration is used to focuse the x-ray beam down to 3x3 μm².

During EXAFS experiments, there are three frequent approaches by which the quantity of absorption is measured:

1. The transmission mode: evaluating the X-ray flux before and after crossing the sample. In this case, the relation between the transmitted and the flux is given by the beer-lambert law $I = I_o e^{-\mu(E)x}$. A simple plot of ln(I_o/I) allows us to obtain XAS spectra.
2. The fluorescence mode: in this case, after absorbing an incident x-ray, the decay of the excited atomic states results in fluorescence photon carrying low energy. The fluorescence energies emitted are characteristic of the excited atom, and can be used to identify the atoms in a sample and to determine their concentrations.
3. The total electron yield mode: rather than releasing a fluorescence photon, the excited atom can relax by emitting a high energy electron (Auger electron) resulting from refilling the vacancy at the core-hole. The number of electrons released can be quantified by measuring the charge compensation with a multi-meter which means that a non-insulator sample is mandatory. Next, the quantified intensity should be compared to the one of the incident x-rays. Generally, this mode is more convenient for light elements (Z<30) [49]. The results presented in this thesis have been collected by using the TEY mode.

1.7. X-Ray Photoelectron Spectroscopy (XPS)

Currently, XPS [50] is considered an essential spectroscopic technique to the study of the physics of a surface material. Its popularity comes from its capability to:

- Identify and quantify what elements are present within a sample surface
- Check the contamination state of a sample material
- Reveal the chemical state and environment of the elements in the investigated material and provide information about the bonding energy and bonding mechanism of surface atoms

1.7.1 General Aspects of XPS Theory

In XPS, the most important mechanism is the photoemission process [51] (figure 1.20), i.e., the emission of an electron from a core level of an atom by x-ray photon energy higher than the binding energy of that electron. The energy of the ejected photoelectrons is then resolved with the help of an electron spectrometer [52] and the produced data is presented as a graph of

two axes: intensity (number of counts) versus the electron binding energy (E_B). In general, the principle and most important equation of XPS is the one given by A. Einstein [53]:

$$E_B = h\nu - E_k - e\phi \tag{1.47}$$

With, $h\nu$ the incident photon energy, E_k is the kinetic energy of the emitted photoelectron and ϕ is the work function of the investigated material which presents the necessary energy an electron requires to travel from the Fermi level to the vacuum. However, in the actual experiment, the energies of photoelectrons are measured by the electron analyzer. Thus, the measured kinetic energy is relative to the work function (ϕ) of the analyzer, which can be measured by calibrating the photoemission data [54].

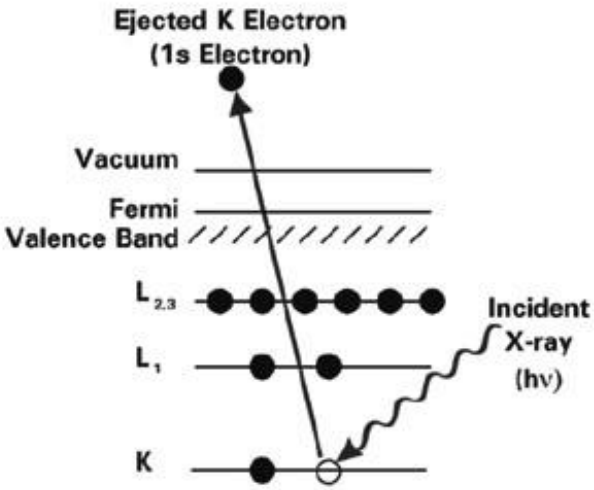

Fig. 1.20: Schematic illustration of photoemission process in XPS experiment showing ejection of 1s electron from a K shell.

For XPS, the soft x-ray radiation with energies varies from 50-1500 eV allows to reach a value of low inelastic mean-free path (λ_m) between 5-20 Å. However, the real escape depth (λ) of the ejected electrons is related also to the angle of emission to the surface normal (θ) such as [55]:

$$\lambda = \lambda_m \cos\theta \tag{1.48}$$

As a result, photoelectrons emitted perpendicular to the surface ($\theta = 0°$) will be associated to the maximum escape depth (bulk), while in the case of ($\theta \approx 90°$) the emitted photoelectrons will be related to the outermost surface layers.

1.7.2 General Aspects of XPS Experiment

As shown from figure 1.21, surface analysis by XPS requires irradiating a solid in an ultra-high vacuum (UHV) chamber with monochromatic soft X-rays and analyzing the energies of the photoelectrons. In general, there are two kinds of electron energy analyzer, the cylindrical mirror analyzer (CMA) and the hemispherical sector analyzer (HSA). Typically, HSA analyzer is more used in XPS experiments because it can provide higher energy resolution [56]. The hemispherical analyzer is shown in figure 1.22, it contains mainly a transfer lens that serve to maximize the collection angle and to retard and decrease the energy of emitted photoelectrons, which helps to achieve better resolution and sensitivity. Also, the HSA analyzer contains two concentric hemispherical electrodes (inner and outer hemisphere) with a gap between them in which the photoelectrons pass while traveling. The addition of a multi-channel detector to the analyzer provides a tool to count the number of the emitted photoelectrons (intensity) during the acquisition of a spectrum.

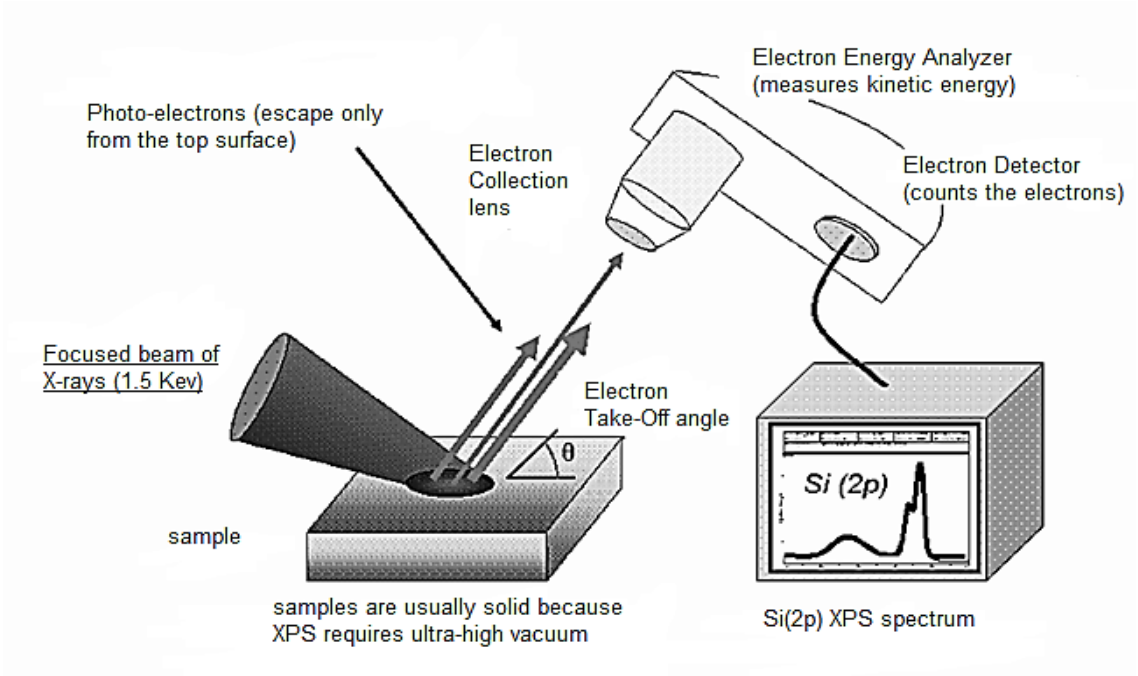

Fig. 1.21: Schematic illustration of a typical XPS instrumentation with photon source (synchrotron radiation), electron optics (transfer lens), hemispherical energy analyzer and an electron detector, and computer system to convert the detected data into a readable spectrum.

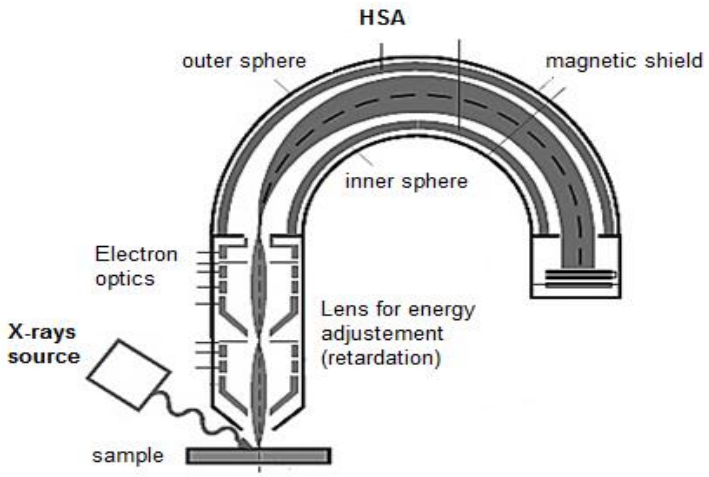

Fig. 1.22: Simple schematic showing the components of a hemispherical energy analyzer.

The XPS experiments reported in this thesis have been performed at the TEMPO beamline [57] at SOLEIL synchrotron. The beamline (see Figure 1.23 for visual illustration) is equipped with an undulator "Apple II" with two periods 44 mm (high energy) and 80 mm (low energy) and can generate circular, linear polarization. High resolution photoemission measurements in the 50 to 1500 eV range were conducted using a SCIENTA SES2002 electron spectrometer.

Analysis of XPS Spectrum

In general, raw XPS spectrum can provide only some generic information. To reveal the chemical state and environment of the elements in the investigated solid material, the XPS raw data should be decomposed to a sum of different environments for each element. This is also true for a perfect pure element, because the atoms located on the outermost surface does not possess the same environment as the atoms located in the bulk. Each peak in an XPS spectrum could be characterized with several parameters:

- Binding energy.
- Intensity.
- Spin-orbit splitting, only possible for orbitals with angular momentum quantum number $l > 0$.
- Branching ratio, used in the case of spin-orbit splitting. This parameter gives the occupation ratio between the spin-orbit components when performing a peak fitting.

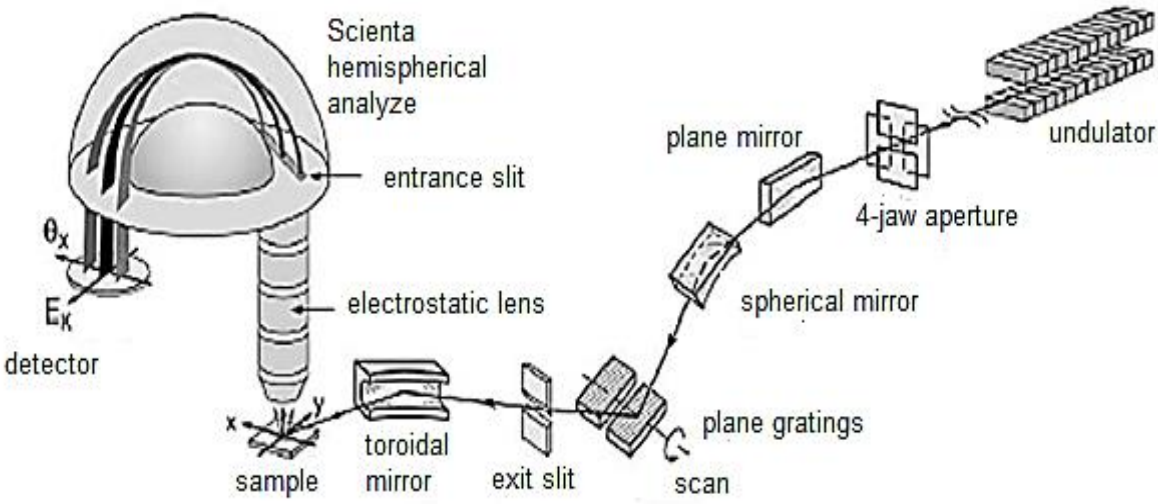

Fig. 1.23: Schematic view of a typical photoelectron spectroscopy synchrotron beamline that consists mainly of an undulator, optical components (mirrors and slits), sample, hemispherical analyzer and finally a detector.

Each component could be defined by a Voigt function, a convolution of Gaussian and a Lorentzian. Full width at half maximum (FWHM) of a Gaussian represents the instrumental contribution, phonon excitation and inhomogeneity of the surface. The effect of phonon could be reduced by cooling down the sample. On the other hand, FWHM of the Lorentzian is associated to the intrinsic life-time broadening of the core level hole state. Moreover, In the case of a metallic sample, the photoelectron when travelling can excite some valence band electrons that are just below Fermi level and loose a part of its energy. This mechanism of energy loss shows as a small shift of the principal peak in the XPS spectrum towards higher binding energies giving an asymmetric peak. In this case, the XPS spectrum fitting is better performed with a Doniach-Sunjic function [58].

The Doniach-Sunjic function is given as follows:

$$f_{DS}(\Delta E) = A\frac{\cos[\frac{\pi\alpha}{2} + (1-\alpha)\arctan\frac{\Delta E}{\gamma}]}{((\Delta E)^2 + \gamma^2)^{\frac{1-\alpha}{2}}} \tag{1.49}$$

Where, α is the asymmetry parameter, A is the amplitude and γ is the full width at half maximum parameter. When analyzing our raw XPS data, the fitting of the peaks was done with components that are defined with a convolution of Doniac-Sunjic and Gaussian function:

$$f_{Ga}(\Delta E) = A\ \exp(-4\ln 2\frac{(\Delta E)^2}{(I_{Ga})^2}) \tag{1.50}$$

With I_{Ga} is the Gaussian FWHM. Using IGOR software tool to analyse the data, the function (1.50) is given by:

$$f_{Ga}(\Delta E) = A\exp\left(-\frac{(\Delta E)^2}{(W)^2}\right) \tag{1.51}$$

With
$$W = \frac{I_{Ga}}{2\sqrt{\ln 2}} = 0.6\ I_{Ga} \tag{1.52}$$

Generally, analyzing an XPS peak is a matter of adjusting and fitting the experimental peak with the theoretical one by changing the parameters listed above. Then, assign each components of fitting to a certain chemical environment of the investigated element.

1.8. Angle Resolved Photoemission Spectroscopy (ARPES)

ARPES is an extension to the classic photoemission spectroscopy and is based on the same equation (1.53) given above. In general, ARPES provides information about the distribution, direction and speed of valence electrons within a solid material [59]. In ARPES experiment, the momentum of photoelectrons that reach the angle resolved electron energy analyzer is given by:

$$p = \sqrt{2mE_k} \tag{1.53}$$

$$p = \hbar k \tag{1.54}$$

$$k = \frac{\sqrt{2mE_k}}{\hbar} \tag{1.55}$$

Here, m is the mass of electron. This equation can be used to get information about the band structure and establish an energy-momentum dispersion relationship.

The momentum of the photoelectron is composed of two components, perpendicular and parallel to the sample surface:

$$\overrightarrow{k_{\parallel}} = \overrightarrow{k_x} + \overrightarrow{k_y} \tag{1.56}$$

and

$$\overrightarrow{k_{\perp}} = \overrightarrow{k_z} \tag{1.57}$$

For each component the momentum-energy relationship can be given as follows:

$$k_x = \frac{\sqrt{2mE_k}\sin\theta\, cos\varphi}{\hbar} \tag{1.58}$$

$$k_y = \frac{\sqrt{2mE_k}\sin\theta\, sin\varphi}{\hbar} \tag{1.59}$$

$$k_z = \frac{\sqrt{2mE_k}\cos\theta}{\hbar} \tag{1.60}$$

θ and φ rotation angles are illustrated in Figure 1.24. The parallel part of the momentum is given by:

$$k_{\parallel} = \frac{\sqrt{2mE_k}\sin\theta}{\hbar} \tag{1.61}$$

Whereas, the perpendicular component $k_{\perp}$ is more problematic because of the existence of a surface potential (V_o) that arises between the surface of the solid and the vacuum. $k_{\perp}$ can be written as:

$$k_{\perp} = \frac{\sqrt{2mE_k + V_o}\cos\theta}{\hbar} \tag{1.62}$$

In general, when investigating 2D systems $k_{\perp}$ can be ignored and only $k_{\parallel}$ considered [60].

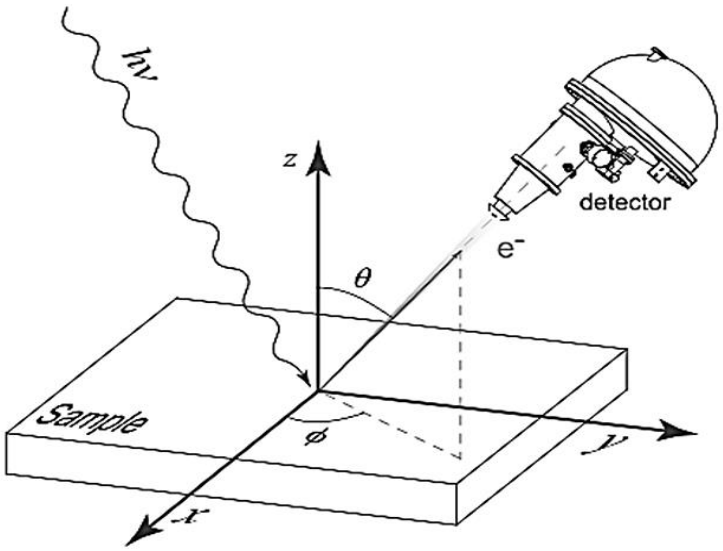

Fig. 1.24: Schematic diagram of emitted photoelectrons in an ARPES setup

Bibliography

[1] Reimer, L. (1993). Kinematical and Dynamical Theory of Electron Diffraction. In *Transmission Electron Microscopy* (pp. 266-320). Springer, Berlin, Heidelberg.

[2] Bragg, W. H., & WL Bragg, B. A. (1913). The reflection of X-rays by crystals. *Proc. R. Soc. Lond. A*, *88*(605), 428-438.

[3] Van Hove, M. A., & Tong, S. Y. (2012). *Surface crystallography by LEED: theory, computation and structural results* (Vol. 2). Springer Science & Business Media.

[4] Wood, E. A. (1964). Vocabulary of surface crystallography. *Journal of applied physics*, *35*(4), 1306-1312.

[5] Woodruff, D. P., & Seah, M. P. (1969). The temperature dependence of the energy of leed intensity peaks and its effect on the surface debye temperature. *Physics Letters A*, *30*(4), 263-264.

[6] Lipkin, H. J. (2004). Physics of Debye-Waller Factors. *arXiv preprint cond-mat/0405023*.

[7] Pesty, F., & Garoche, P. (2005). Low-energy electron beam on an insulator surface: Impact of the charging process on the diffraction by mica muscovite. *Surface science*, *580*(1-3), 153-162.

[8] Rundgren, J. (1999). Electron inelastic mean free path, electron attenuation length, and low-energy electron-diffraction theory. *Physical Review B*, *59*(7), 5106.

[9] P. Auger: Comptes Rendus 177, 169 (1923).

[10] Jablonski, A. (2005). Determination of the electron inelastic mean free path in solids from the elastic electron backscattering intensity. *Surface and interface analysis*, *37*(11), 1035-1044.

[11] Oura, K., Katayama, M., Zotov, A. V., Lifshits, V. G., & Saranin, A. A. (2003). Elementary Processes at Surfaces I. Adsorption and Desorption. In *Surface Science* (pp. 295-323). Springer, Berlin, Heidelberg.

[12] Jablonski, A. (2005). Determination of the electron inelastic mean free path in solids from the elastic electron backscattering intensity. *Surface and interface analysis*, *37*(11), 1035-1044.

[13] Yamamoto, S., Yokogawa, H., & Hashimoto, H. (1985). Cylindrical Mirror Analyzer for Measuring Energy Spectrum of Photostimulated Exoelectrons. *Japanese Journal of Applied Physics*, *24*(S4), 281.

[14] Browning, R., Bassett, P. J., El Gomati, M. M., & Prutton, M. (1977). A digital scanning Auger electron microscope incorporating a concentric hemispherical analyser. *Proc. R. Soc. Lond. A*, *357*(1689), 213-230.

[15] Zak, A. K., Hashim, A. M., & Darroudi, M. (2014). Optical properties of ZnO/BaCO 3 nanocomposites in UV and visible regions. *Nanoscale research letters*, *9*(1), 399.

[16] Davis, L. E., MacDonald, N. C., Palmberg, P. W., Riach, G. E., & Weber, R. E. (1976). Handbook of Auger electron spectroscopy. *Physical Electronics Industries, Eden Prairie, MN*, *27*(6), l.

[17] Binnig, G., & Rohrer, H. (1983). Scanning tunneling microscopy. *Surface science*, *126*(1-3), 236-244.

[18] Garcia, R., Knoll, A. W., & Riedo, E. (2014). Advanced scanning probe lithography. *Nature nanotechnology*, *9*(8), 577.

[19] Bhushan, B., & Blackman, G. S. (1991). Atomic force microscopy of magnetic rigid disks and sliders and its applications to tribology. *Journal of tribology*, *113*(3), 452-457.

[20] Meyer, G., & Amer, N. M. (1988). Novel optical approach to atomic force microscopy. *Applied physics letters*, *53*(12), 1045-1047.

[21] Liu, H., & Bhushan, B. (2002). Investigation of nanotribological properties of self-assembled monolayers with alkyl and biphenyl spacer chains. *Ultramicroscopy*, *91*(1-4), 185-202.

[22] Giessibl, F. J., Gerber, C., & Binnig, G. (1991). A low-temperature atomic force/scanning tunneling microscope for ultrahigh vacuum. *Journal of Vacuum Science & Technology B: Microelectronics and Nanometer Structures Processing, Measurement, and Phenomena*, *9*(2), 984-988.

[23] Giaever, I. (1960). Energy gap in superconductors measured by electron tunneling. *Physical Review Letters*, *5*(4), 147.

[24] Tersoff, J., & Hamann, D. R. (1985). Theory of the scanning tunneling microscope. In *scanning tunneling microscopy* (pp. 59-67). Springer, Dordrecht.

[25] Bardeen, J. (1961). Tunnelling from a many-particle point of view. *Physical Review Letters*, *6*(2), 57.

[26] Okano, M., Kajimura, K., Wakiyama, S., Sakai, F., Mizutani, W., & Ono, M. (1987). Vibration isolation for scanning tunneling microscopy. *Journal of Vacuum Science & Technology A: Vacuum, Surfaces, and Films*, *5*(6), 3313-3320.

[27] Anders, M., Thaer, M., & Heiden, C. (1987). Simple micropositioning devices for STM. *Surface Science*, *181*(1-2), 176-182.

[28] Maeder, M. D., Damjanovic, D., & Setter, N. (2004). Lead free piezoelectric materials. *Journal of Electroceramics*, *13*(1-3), 385-392.

[29] Binnig, G., & Smith, D. P. (1986). Single-tube three-dimensional scanner for scanning tunneling microscopy. *Review of Scientific Instruments*, *57*(8), 1688-1689.

[30] G. Binnig, H. Rohrer: Surf. Sci. 126,236 (1983)

[31] Modern Piezoelectric Ceramics, Vemitron Piezoelectric Division, 232 Forbes Road, Bedford, Ohio 44146, USA.

[32] Kim, D. J., & Koo, J. Y. (2005). A low-noise and wide-band ac boosting current-to-voltage amplifier for scanning tunneling microscopy. *Review of scientific instruments*, *76*(2), 023703.

[33] Morgan, B. A., & Stupian, G. W. (1991). Digital feedback control loops for scanning tunneling microscopes. *Review of scientific instruments*, *62*(12), 3112-3113.

[34] Chen, C. J. (1989). Role of tip material in scanning tunneling microscopy. *MRS Online Proceedings Library Archive*, *159*.

[35] Ohnishi, S., & Tsukada, M. (1989). Molecular orbital theory for the scanning tunneling microscopy. *Solid State Communications*, *71*(5), 391-394.

[36] Fotino, M. (1993). Tip sharpening by normal and reverse electrochemical etching. *Review of Scientific Instruments*, *64*(1), 159-167.

[37] Melmed, A. J. (1991). The art and science and other aspects of making sharp tips. *Journal of Vacuum Science & Technology B: Microelectronics and Nanometer Structures Processing, Measurement, and Phenomena*, *9*(2), 601-608.

[38] Ekvall, I., Wahlström, E., Claesson, D., Olin, H., & Olsson, E. (1999). Preparation and characterization of electrochemically etched W tips for STM. *Measurement Science and Technology*, *10*(1), 11.

[39] Gooden, J. S., Jensen, H. H., & Symonds, J. L. (1947). Theory of the proton synchrotron. *Proceedings of the Physical Society*, *59*(4), 677.

[40] Wille, K. (1998). Introduction to insertion devices.

[41] Padamsee, H. (2001). The science and technology of superconducting cavities for accelerators. *Superconductor science and technology*, *14*(4), R28.

[42] Som, S., Seth, S., Mandal, A., Paul, S. and Duttagupta, A., 2013. Radio frequency cavity analysis, measurement, and calibration of absolute Dee voltage for K-500 superconducting cyclotron at VECC, Kolkata. *Review of Scientific Instruments*, *84*(2), p.023303.

[43] Codling, K., Gudat, W., Koch, E. E., Kotani, A., Lynch, D. W., Rowe, E. M., ... & Toyozawa, Y. (2013). *Synchrotron radiation: techniques and applications* (Vol. 10). Springer Science & Business Media.

[44] Baudelet, F., Belkhou, R., Briois, V., Coati, A., & Dumas, P. (2005). SOLEIL a new powerful tool for materials science. *Oil & Gas Science and Technology*, *60*(5), 849-874.

[45] Van Bokhoven, J. A., & Lamberti, C. (Eds.). (2016). *X-ray absorption and X-ray emission spectroscopy: theory and applications* (Vol. 1). John Wiley & Sons.

[46] Calvin, Scott. XAFS for Everyone. CRC press, 2013.

[47] Koningsberger, D.C., Mojet, B.L., Van Dorssen, G.E. and Ramaker, D.E., 2000. XAFS spectroscopy; fundamental principles and data analysis. *Topics in catalysis*, *10*(3-4), pp.143-155.

[48] Vantelon, D., Trcera, N., Roy, D., Moreno, T., Mailly, D., Guilet, S., ... & Flank, A. M. (2016). The LUCIA beamline at SOLEIL. *Journal of synchrotron radiation*, *23*(2), 635-640.

[49] Chakarian, V., & Idzerda, Y. U. (1997). Total electron yield method in x-ray absorption spectroscopy: A closer look at the saturation/self-absorption effects. *Journal of Applied Physics*, *81*(8), 4709-4709.

[50] Hollander, J.M. and Jolly, W.L., 1970. X-ray photoelectron spectroscopy. *Accounts of chemical research*, *3*(6), pp.193-200.

[51] Santana, J.A.C., 2015. Brief theory of photoemission spectroscopy. In *Quantitative Core Level Photoelectron Spectroscopy*. Morgan & Claypool Publishers.

[52] Mårtensson, N., Baltzer, P., Brühwiler, P.A., Forsell, J.O., Nilsson, A., Stenborg, A. and Wannberg, B., 1994. A very high resolution electron spectrometer. *Journal of Electron Spectroscopy and Related Phenomena*, *70*(2), pp.117-128.

[53] Einstein, A. (1905). Einstein, A., 1905, Ann. Phys.(Leipzig) 31, 132. *Ann. Phys.(Leipzig)*, *31*, 132.

[54] Schlaf, R. (2014). Calibration of photoemission spectra and work function determination.

[55] Van der Heide, P. (2014). *Secondary Ion Mass Spectrometry: An Introduction to Principles and Practices*. John Wiley & Sons.

[56] Sherwood, P. M. A., Briggs, D., & Seah, M. P. (1990). Practical surface analysis. *Auger and X-ray Photoelectron Spectroscopy*, *1*, 555.

[57] Polack, F., Silly, M., Chauvet, C., Lagarde, B., Bergeard, N., Izquierdo, M., ... & Basset, C. (2010, June). TEMPO: a new insertion device beamline at SOLEIL for time resolved photoelectron spectroscopy experiments on solids and interfaces. In *AIP Conference Proceedings* (Vol. 1234, No. 1, pp. 185-188). AIP.

[58] Doniach, S., & Sunjic, M. (1970). Many-electron singularity in X-ray photoemission and X-ray line spectra from metals. *Journal of Physics C: Solid State Physics*, *3*(2), 285.

[59] Damascelli, A. (2004). Probing the electronic structure of complex systems by ARPES. *Physica Scripta*, *2004*(T109), 61.

[60] Palczewski, A. D. (2010). *Angle-resolved photoemission spectroscopy (ARPES) studies of cuprate superconductors*. Iowa State University.

Chapter 2. Growth of NaCl Ultra-Thin Film on Ag(110) Metallic Substrate

In this chapter the growth and characterization of insulating films of NaCl grown on Ag(110) surface is reported. The brief overview presented here shows the interest in insulating ultra-thin films which has been rising in the last decade. A great part of this thesis is devoted to the investigation of NaCl insulating films. Specifically, scanning tunneling microscopy (STM), scanning tunneling spectroscopy (STS), x-ray photoelectron spectroscopy (XPS) and low energy electron diffraction (LEED) have been used to investigate the morphology, crystallography, electronic and chemical properties of the grown NaCl films. Significant consideration has been given to different growth conditions allowing us to prepare a metallic substrate that is almost covered with insulating films in order to study the adsorption of silicon 2D layer in the next part of the thesis.

2.1. Motivation

In the last decade a huge interest has been devoted to thin insulating films because of their promising applications in the field of surface science and nanotechnology. Furthermore, the improvement of many surface experimental techniques led researchers to investigate more and more on insulating materials. This is due mainly to the fact that the majority of surface investigation instrumental techniques such as STM, LEED, PES, AES work only on conductive surfaces.

To overcome such limitations when working with insulators, the idea of using insulating thin films rather than bulk insulating material is very interesting. One of the key advantages of using such an alternative is that electron-based surface characterization techniques will work for thin insulating layer due to the weak charging effects. For example, scanning tunneling microscopy investigations of these surfaces are possible because the electron wave function

can penetrate through the ultra-thin dielectric layers (1 nm thick or less) allowing the current to flow [1].

One of the most promising applications that drive us to use NaCl alkali-halide insulating films in this thesis is the fact that they are an ideal solution to the problem of decoupling the electronic states of adsorbed nanostructures or atomic-molecular species. This will also help to avoid charging issues that one can face when using the bulk insulator. Indeed, it has been demonstrated recently by Husseen and coworkers [2] that, NaCl and KCl thin films can be used with STM, since the electrons can tunnel through the films into the underlying conducting substrate. Reported studies show that such 2D insulating surfaces have been employed successfully to study and enhance the intrinsic features of atomic-scale structures. In another study, thin insulating films have been used as atomically controlled spacers allowing individual molecular orbitals to be probed, e.g. decoupled pentacene molecules from metallic Cu(111) using NaCl films [3]. This NaCl layer on metallic Cu(111) surface allows to access important information related to molecular spectroscopy that could be complementary to the one acquired on metal substrate. In fact, due to the weaker interactions with the substrate, the intrinsic molecular states can be investigated with or without weak perturbations that can cause strong distortion of the molecular states [3,4]. The same approach can be applied on 2D systems such as silicene or graphene.

In addition, ultra-thin insulating films can also be used to develop new charge manipulation scheme or to stabilize the charge states of ad-atoms [5]. An experimental work performed by Steurer et al. [6] on Au ad-atoms on NaCl films deposited on metallic substrate shows that by attaching or detaching electrons from the Au atoms using an atomic force microscope tip, the lifetime of the neutral and positive charge state of Au ad-atoms increases with NaCl film thickness. This allows a longer and better charge manipulation experiment. Other advanced experiments performed by Nilius et al. [7] showed that ultra-thin films can have an influence on the catalytic activity of metals and on the spatial distribution of ad-atoms or molecular systems.

2.2. NaCl Thin Film Growth: State of the Art

The reason of using alkali-halide NaCl as an insulator material is due to the small mismatch between the NaCl (100) plane and Ag(110) surface lattice parameters as will be seen from the LEED results in section 2.4 of this chapter. Obviously, rock-salt NaCl offers a great flexibility when selecting the surface on which the insulating layers can be grown. Various

substrates have already been used for the growth of NaCl insulating films including metals surfaces such as Cu(111) [8], Cu(100) [9], Ag(100) [10], Ag(111) [11], Al(100) [12] and Au(111) [13], as well as semiconductors such as Ge(001) [14] and Ge(111) [15].

In the majority of the reported studies, NaCl films are obtained using simple physical vapor deposition (PVD) process. Generally, NaCl crystal melts at 800 °C [16] and it can easily be sublimated at a comparably lower temperature in ultra-high vacuum conditions (Pressure $<10^{-10}$ mbar). In these conditions, the formed insulating layers have been investigated using multiple surface-sensitive techniques such as STM [17-18], STS [19], non-contact atomic force microscopy and Kelvin probe force microscopy [20]. It was reported by Cabailh et al. [20] that the size of NaCl islands could be increased by annealing the substrate during the growth (see figure 2.1). Indeed, the annealing induces NaCl molecules diffusion on the surface.

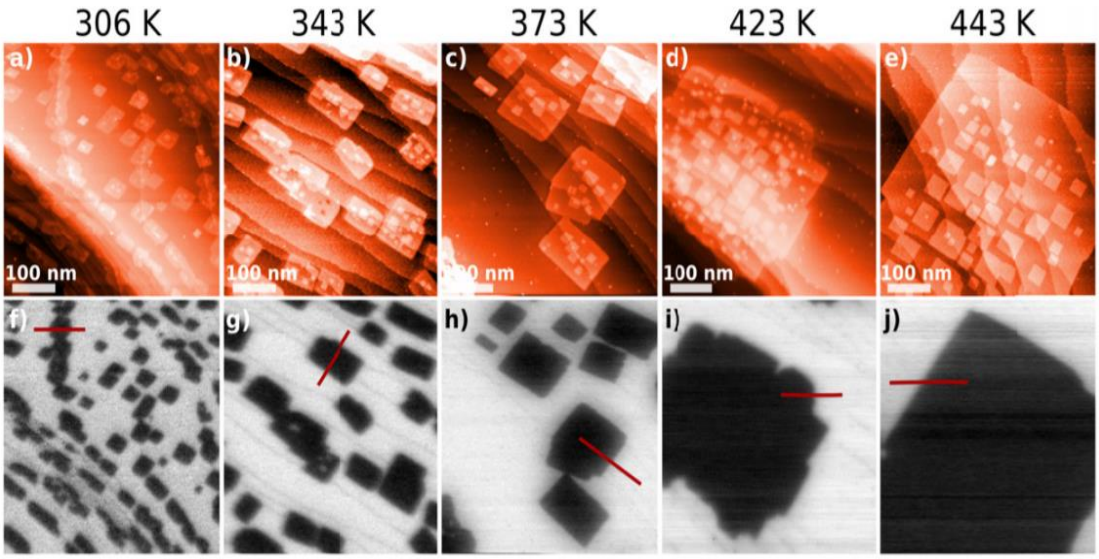

Fig. 2.1 nc-AFM (top) and KPFM (bottom) images of 0.75 ML NaCl deposited on Ag(001) surface showing the influence of the substrate temperature on the size and morphology of NaCl islands. Image from [20].

It is also interesting to note that, generally NaCl growth is not altered by the substrate. This is due to the strong ionic bond of rock-salt NaCl (cohesive energy of 6.62 eV per ion pair [21]) that strongly dominates and drives the NaCl film formation. Furthermore, due to the strong

Coulomb interaction between Na^+ and Cl^-, the crystallographic structure which minimizes the energy for the NaCl film should mimics the (100) plane of the bulk salt [22].

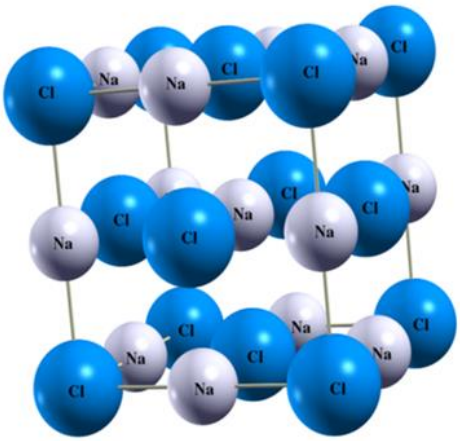

Fig. 2.2 NaCl crystal bulk structure showing its ionic cubic symmetry in which chlorine has a negative charge (Cl^-) and sodium has a positive charge (Na^+). The NaCl bulk lattice parameter is 0.564 nm and its neutral facet (100) has a Cl-Cl distance of 0.399 nm. Each ion (Cl^- or Na^+) on the bulk crystal has six neighboors with opposite charge in a cubic packed (ccp) structure.

NaCl film growth on different substrates shows a common relaxation effect of the 2D film where a layer buckling of the Na-Cl in-plane is reported on Cu(111) [23]. This relaxation effect is due mainly to the high compressibility of alkali halides (NaCl crystal modulus is 0.24 10^{11} N/m^2 [24]) and not the effect of the underlying substrate. Another remarkable observation associated with NaCl insulating film growth on metallic substrates is the so called carpet-like growth mode. Such growth mode has been observed on substrates such as Al(100) [12] and Ag(001) [2] in which step edges seem to be the preferred nucleation sites for the NaCl islands growth. In this case, the formation of these NaCl “carpets” extending across two adjacent terraces appears to be energetically favorable.

2.3. Sample Preparation

NaCl ultra-thin layers have been deposited on the metallic substrate Ag(110). The crystal has a cylindrical shape with diameter of 8 mm and height of 1 mm. It has been prepared according to regular surface science procedures using multiple cycles of Ar^+ ion bombardment (sputtering) and thermal annealing. Before each new deposition, the substrate has been cleaned again with two Ar^+ sputtering-annealing cycles:

- Sputtering is obtained by bombardment of the Ag(110) surface with Ar^+ energetic ions in order to remove contamination and previously deposited film residue. For sputtering we used the following parameters (Ar^+ ions energy = 650 eV, chamber pressure ~ 10^{-5} mbar, substrate at room temperature and a continuous 45 min of bombardment).
- Annealing: after sputtering, we use thermal annealing mainly to recrystallize the atomic structure of the Ag(110) substrate. The annealing is performed at 480 °C for 15 min by heating the sample by Joule effect using a tungsten filament located 2 mm behind the sample.

The sample preparation described here, allows to produce an atomically flat and clean metallic Ag(110) substrate. The quality of the clean surface has been periodically verified using STM, LEED and AES (see figure 2.3). STM topographic images reveal atomically flat terraces. The atomic resolution images show a perfect crystallographic structure of the Ag(110) substrate. The surface has been crosschecked using LEED which reveals a clear rectangular diffraction pattern which characterizes the plane (110) of the Ag substrate. The absence of contamination on the newly prepared substrate has also been verified using the AES technique. Further analysis of the recorded Auger spectrum shows the existence of the Ag element peaks only at 351 and 356 eV and the absence of any other contaminant such as carbon at 272 eV or oxygen at 503 eV (see figure 2.3).

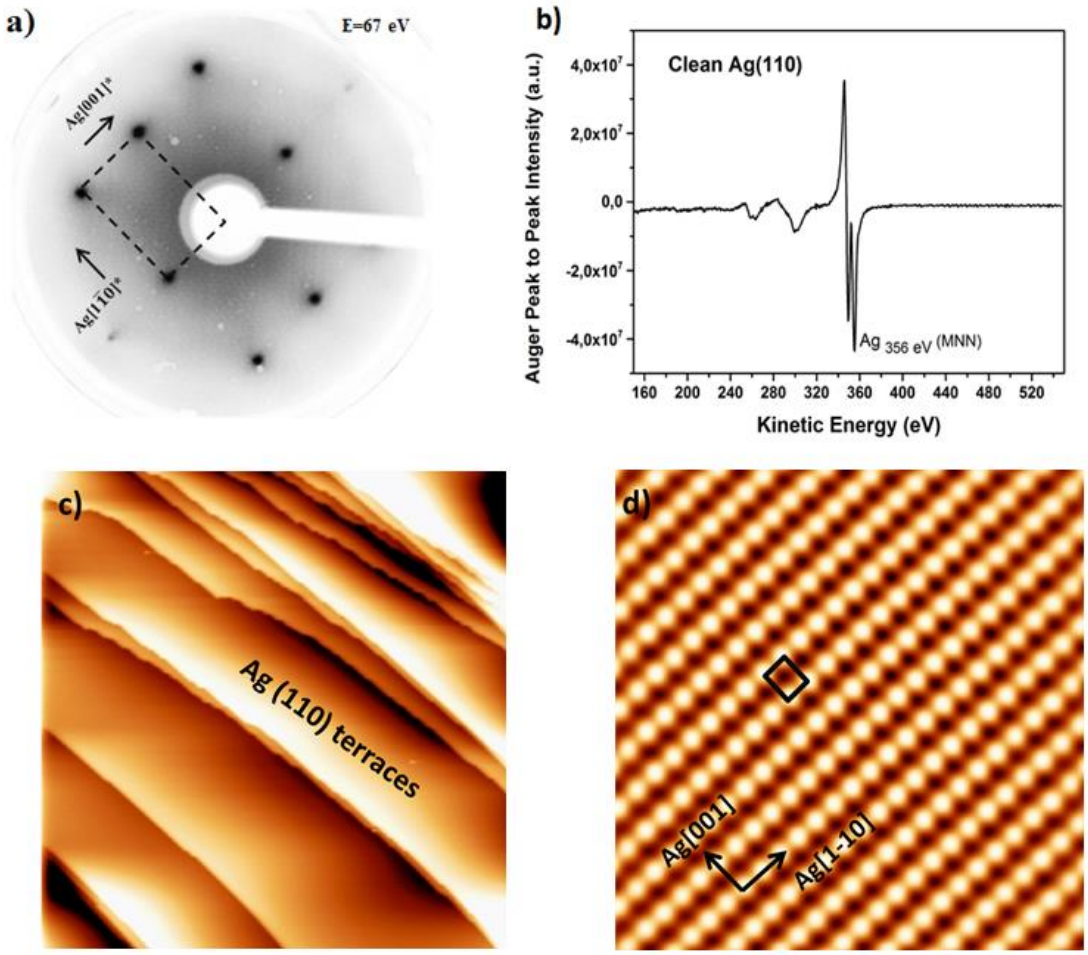

Fig. 2.3 Clean Ag(110) substrate investigated after applying the sample preparation described above showing a) LEED diffraction pattern b) Auger electron spectroscopy c) STM topography recorded at LT-STM with the tunneling parameters (100x100nm², V_b= -0,3V, I_t=1,15 nA) and d) Atomically resolved STM image showing the rectangular structure of the surface (110) with 5x5nm², V_b= -0,04V, I_t=2,5 nA).

For the insulating film growth, we used rock-salt sodium chloride (NaCl) powder of 99.99% purity. After cleaning the substrate using the parameters mentioned above, we evaporated the NaCl powder from a Knudsen effusion cell. Prior to NaCl deposition, cycles of degassing of the Knudsen cell were performed in order to remove water and other contaminants. The degassing was made by heating the cell gradually until reaching 200 °C. Simultaneously, the vacuum pressure inside the chamber was kept below 10^{-8} mbar. The deposition rate was

controlled using a quartz microbalance placed a few centimeters away from the manipulator holding the sample and the vapor pressure upon heating the NaCl cell was kept below 10^{-9} mbar. Prior to NaCl deposition, we kept the evaporation shutter closed until reaching the NaCl powder sublimation temperature. Different evaporation rates have been tested but, for the majority of the results presented in this thesis, NaCl films have been prepared using the following parameters:

- Deposition rate of ~ 0.04 NaCl monolayer per minute
- Cell temperature = 520 °C (before opening the shutter) and 500 °C (after opening the shutter)

During deposition, the sample temperature can be controlled by resistive heating of the sample manipulator using a thermocouple. For our experiments, thermal annealing during evaporation and post-annealing proved to be an important factor to control the quality of the grown film. The thermal annealing increases the diffusion of the NaCl molecules and allows to control the size of the islands which cover the Ag(110) surface. The optimal temperature of the substrate we used during the NaCl growth is 140 °C as will be seen from the experimental results.

2.4. LEED Measurements

Figure 2.4 shows the recorded LEED pattern of the substrate before and after the deposition of ~ 1 Monolayer (ML) of NaCl with an evaporation rate of 0.04ML/min. During the evaporation the substrate was kept at room temperature (RT). Figure 2.4a clearly shows the expected rectangular symmetry of the Ag(110) surface without any spots indicating the cleanliness and homogeneity of the surface. After NaCl deposition, the LEED pattern starts to show a new (4x1) superstructure, which can be explained by means of a small lattice mismatch between the structural parameters of Ag(110)-(1x1) and NaCl(100)-(1x1) surfaces. Indeed, if we consider the substrate [1-10] direction, we find that 4x $a_{Ag[1-10]}$ =1.155 nm is very close to 3x $a_{NaCl[100]}$=1.196 nm, with a small lattice mismatch of 3.55%. As for the other substrate direction Ag[001], the NaCl lattice parameter $a_{NaCl[01-1]}$ = 0.4 nm is close to $a_{Ag[001]}$ = 0.408 nm with a small lattice mismatch of 2.00%.

From the LEED pattern, a lattice constant of 0.54 nm for the NaCl film has been measured using the Ag diffraction spots as a reference. It is quite close to the bulk lattice constant of NaCl of 0.564 nm. In addition to the mismatch and the periodicity between the two surfaces,

we can also conclude from this result that the epitaxial growth of NaCl on Ag(110) forms with a (100)-surface symmetry. NaCl films present a parallel orientation with respect to Ag(110) directions where NaCl[011]//Ag[1-10] and NaCl[0-11]//Ag[001] as shown in the LEED pattern (see figure 2.4b).

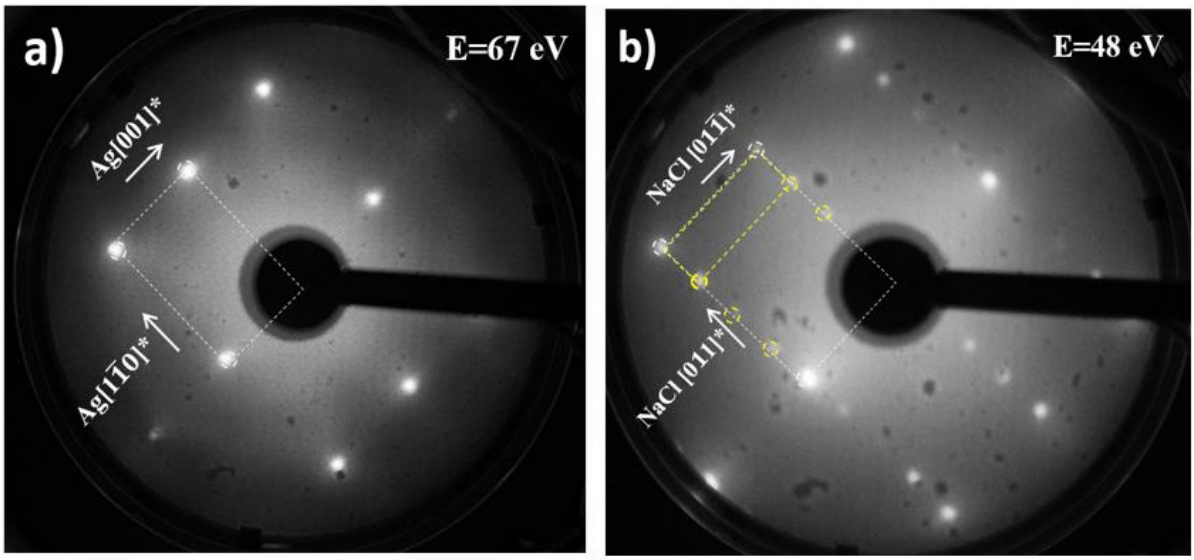

Fig. 2.4 LEED patterns of (a) clean Ag (110) surface, (b) after NaCl deposition at room temperature. The white dashed rectangle shows the Ag-(1x1) and the yellow one shows the new (4x1) superstructure of NaCl/Ag(110).

The preferred NaCl (100)-surface growth has also been observed on other metallic surfaces and has been found to be independent of the substrate plane symmetry [25,26] because the surface energy of the (100) plane is lower than that of the (111) plane [27]. In addition to the lower surface energy, NaCl (100) is electrically neutral in contrast to the (111) plane which is polar due to the alternation of the Na and Cl planes in the NaCl [111] direction.

We should note that during our first NaCl evaporation experiments we did find that lower coverages in the 0.2 – 0.7 ML range result in the same crystalline (4x1) superstructure, and that only the intensity of the spots changed with the amount of surface area as it will be shown with STM topographic images of the surface.

The substrate temperature for the evaporation process is also an important factor in the growth process. Figure 2.5 presents LEED patterns of NaCl film grown at 140 °C, NaCl film grown after a post annealing of ~220 °C for 10 min and NaCl bulk crystal. From figure 2.5a we can notice that "3/4" spots (highlighted by yellow circles) in the Ag[1-10] direction are more intense than Ag diffraction spots (highlighted by white circles).

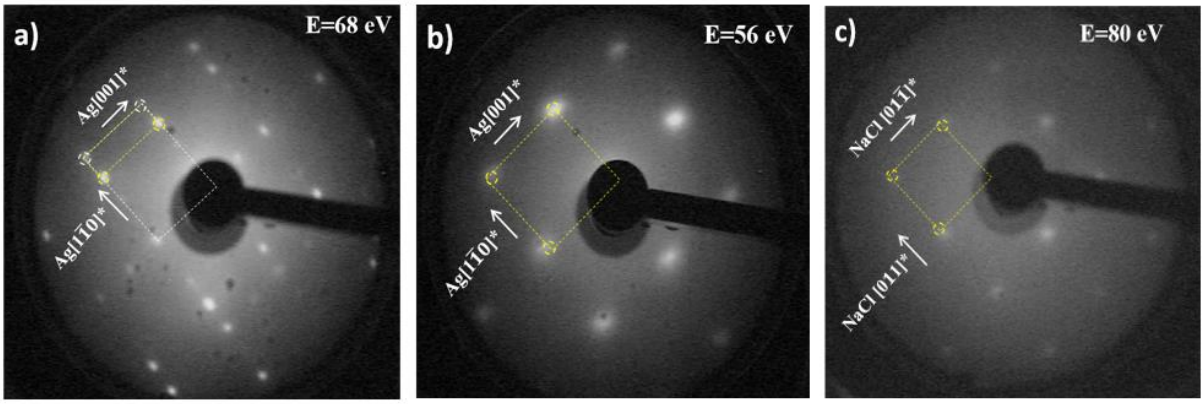

Fig. 2.5 LEED patterns recorded at room temperature of (a) ~1ML NaCl deposited on Ag(110) surface held at 140°C, (b) ~1ML NaCl deposited into Ag(110) with a post annealing at 220°C for 30 min, (c) NaCl (100) surface recorded from NaCl crystal bulk. The white and yellow circles refer to Ag and NaCl diffraction spots, respectively.

During our experiments we found that not only the amount of NaCl coverage affects the diffraction spot intensity but also the annealing temperature used during the deposition process. This is due to the coalescence effect resulting from the heating of the substrate. In figure 2.5a the coalescence effect is partial and only the "3/4" spots are intense. These"3/4" spots have a square symmetry which shows that the NaCl films start to form a NaCl bulk-like structure. Furthermore, when applying a post annealing on the surface at ~220°C the NaCl films coalesce completely and the Ag substrate diffraction spots disappear (see figure 2.5b). Figure 2.5c shows a LEED pattern recorded on the NaCl bulk crystal, in which the square diffraction symmetry of the NaCl (100) surface is observed and can be compared with the pattern of figure 2.5b. The LEED patterns of both these surfaces look fuzzy and blurry due to the charging effect of the sample.

2.5. AES Measurements

We use Auger electron spectroscopy to check the cleanliness of the substrate, investigate the surface chemical composition and estimate the necessary time in order to grow ~1ML of sodium chloride. Figure 2.6 shows two Auger spectra before and after deposition of NaCl on the Ag(110) substrate kept at 140 °C. The first spectrum in figure 2.6a shows that the surface is perfectly clean after sample preparation without any contaminants such as oxygen or carbon. In the second spectrum, the chlorine Auger peak appears at 181 eV. We can also note, that the silver Auger Peak (356 eV) is attenuated by about 41% after NaCl deposition (the measured Auger peak to peak intensity for $Ag_{356\ eV}$ (MNN) before and after NaCl deposition is 8.0 10^8 and 3.3 10^8, respectively). This attenuation agrees with the theoretical value (38%) expected from the empirical equation below [28] in which the intensity of the Auger electrons emitted from a substrate, I_s, covered by a uniform over-layer film of thickness d is given by:

$$I_s = I_s^o \exp(-\frac{d}{\lambda \cos(\alpha)}) \qquad (2.1)$$

Where,

I_s^o is the signal intensity from the bare substrate. For an over-layer film of 1 ML NaCl, the theoretical thickness value is $d = 0.28\,nm$.

α presents the geometric factor related to the CMA analyzer instrument, it is the angle of emission of Auger electrons from the surface (with respect to the surface normal). For our Auger spectroscopy instrument $\alpha = 42.1°$.

λ refers to the inelastic mean free path of Ag Auger electrons through an NaCl film which is given by the empirical law as follows [29]

$$\lambda \cong \sqrt{E}/2 \qquad (2.2)$$

Here, E is the peak energy position of the substrate chemical element. This estimation of the inelastic mean free path is only valid for energies higher than 40 eV.
We should note that we were not able to detect the Na Auger peak in the spectrum in figure 2.6. This is because the Na Auger peak is located at higher energy (KLL transition around 990 eV) and the peak intensity of Na is four times smaller than the peak intensity of Cl according to the Auger electron spectroscopy handbook [30].

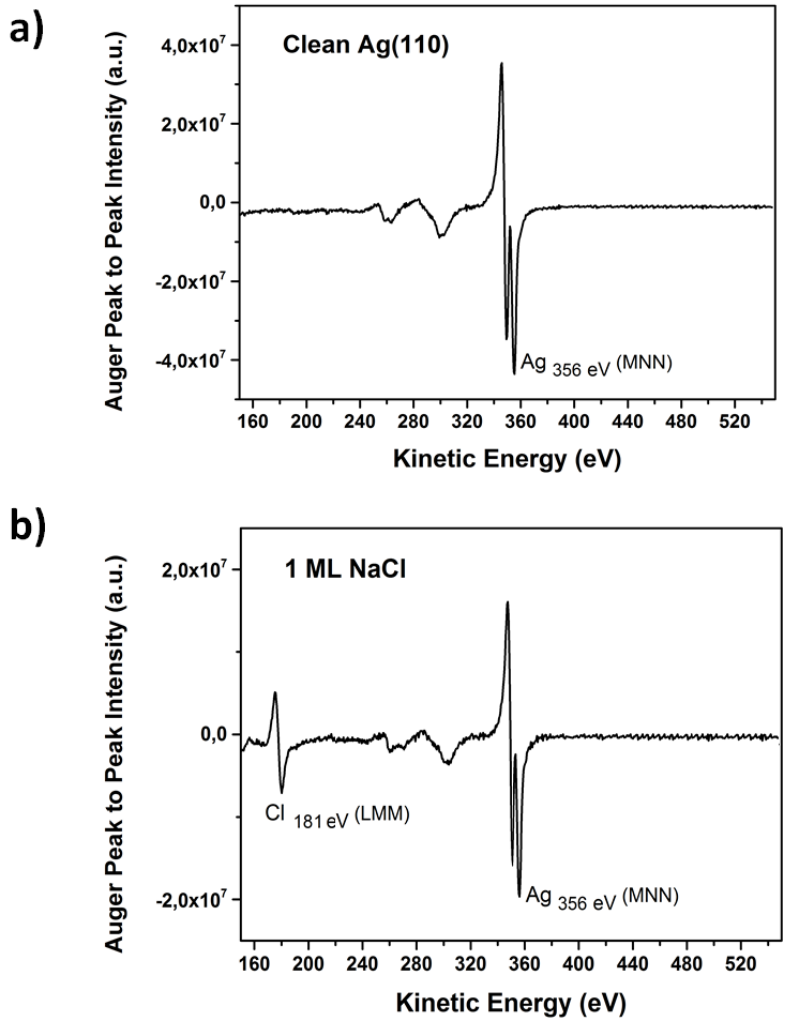

Fig. 2.6 Differential AES mode spectra recorded for a) clean Ag(110) substrate, b) after deposition of ~1ML NaCl at 140°C.

AES can also be used to investigate and control the growth mechanism of adsorbates or molecular films on surfaces. Figure 2.7 is a plot of the AES peak to peak intensity of Ag at 356 eV and Cl at 181 eV as a function of deposition time. We can see an increase of the Cl Auger signal and a decrease of the Ag Auger signal without any breaks. This is a strong indication of a Volmer-Weber-type growth, in which the nucleation of a second NaCl layer will start even before the initial NaCl layer is complete. This NaCl growth mode on silver is in agreement with the STM observations which will be shown in the next section. Generally, in Volmer-Weber (VW) growth, ad-atom/ad-atom interactions are stronger than those of the ad-atom/surface, leading to the formation of ad-atom clusters or islands [31]. Moreover, a weak ad-atom surface interaction means a relatively low binding energy between the adsorbate atoms and the substrate.

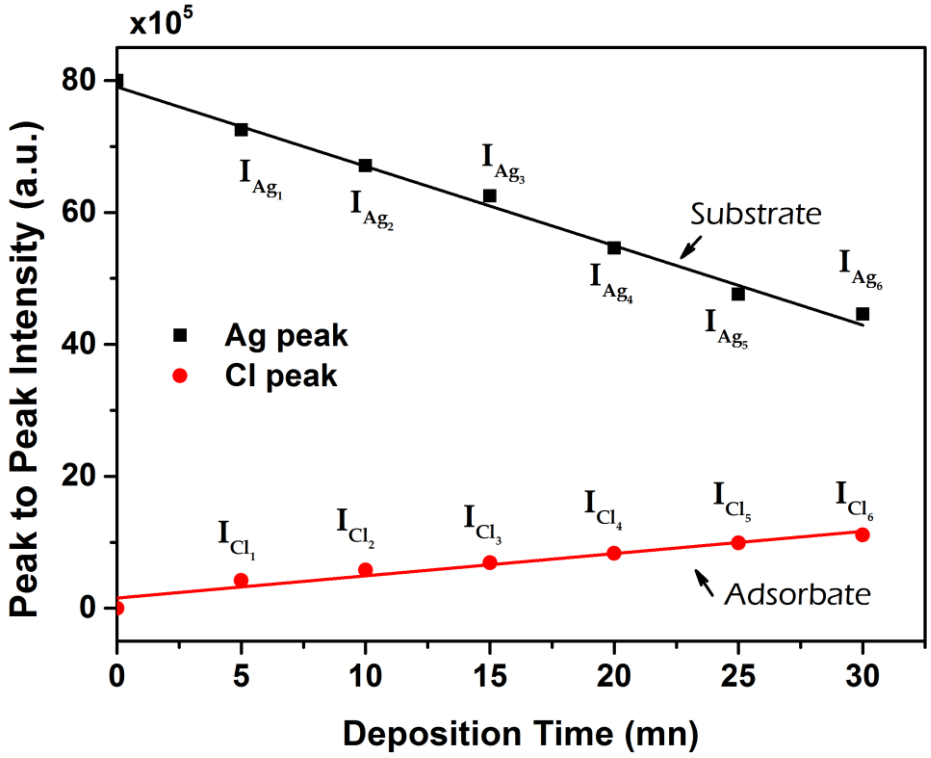

Fig. 2.7 Peak to peak Auger intensity of Ag (356 eV) and Cl (181 eV) as function of the deposition time. The substrate was kept at room temperature.

2.6. STM Observations

Generally, STM experiments on insulating materials are possible when one of the following conditions is fulfilled:

- Electron transport through the dielectric film is possible via tunneling, as the wave functions of the underlying metal substrate penetrate the insulating material overlaping with the tip electronic states. This conduction mechanism is only applicable on ultra-thin dielectric layers with a thickness less than 10 Å [1].

- Thermal annealing of the insulating materials during measurement could provide a sufficient conductivity to perform an STM imaging experiment. In fact, this has been proven for wide-gap insulators such as NiO [32] when a small number of its valence electrons are excited into the conduction band. These electrons behave like free electronic charges that can contribute to the tunneling effect. With our experimental

setup, performing elevated temperature scanning tunneling microscopy is not possible as we are using an LT-STM microscope.

Scanning tunneling microscopy is used to investigate the geometry and morphology of the ultra-thin NaCl films grown on the Ag(110) substrate. We note that deposition of NaCl at room temperature (27 °C) results in small islands showing that the substrate temperature is not sufficient to induce the formation of large islands due to the limited diffusion of NaCl molecules on the surface (see figure 2.8a). Different substrate temperatures starting from room temperature to 220 °C have been tested and the surface subsequently imaged with STM. As discussed above, the LEED diffraction pattern shows a clear (4x1) superstructure in all cases expect for temperatures around 220 °C where the deposited NaCl islands tend to form an NaCl bulk structure due to the strong coalescence effect.

NaCl Films Grown At 140°C

Figure 2.8b presents an STM topography image of an ultrathin NaCl film grown on Ag(110) at 140 °C after deposition of about 1ML of NaCl. It can be seen that the NaCl film consists of islands with square or rectangular shapes ranging between 150 to 200 nm in size. The islands have straight nonpolar edges and they often grow on the top of silver step edges indicating that silver step edges are the preferred nucleation sites as has been demonstrated on other metallic substrates [10-13]. Furthermore, the islands borders that are aligned along the [100] direction can also lead to NaCl films with rectangular shape. This can be explained by the surface energy which is favorable for NaCl molecules to rearrange in the [100] direction of the substrate and which is unfavorable for the [111] NaCl direction [33].

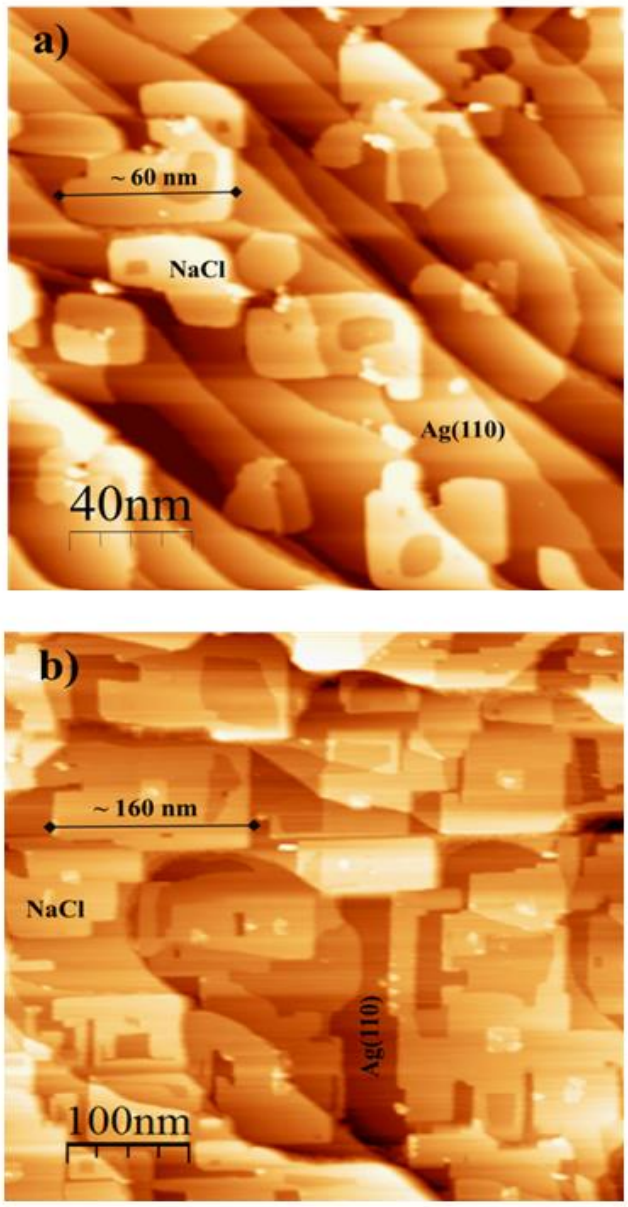

Fig. 2.8 LT-STM topography of NaCl deposited on Ag(110) a) 0.4 ML NaCl at room temperature (200x200 nm² , -1.5 V, 0.8 nA) and b) ~1 ML when substrate was held at 140 °C (500x500 nm^2, -1.05 V, 0.7 nA)

Figure 2.9 presents an STM topography that shows the atomic resolved lattice of the NaCl film and the adjacent clean Ag(110) terrace. From the silver substrate lattice structure close to the NaCl island (see figure 2.9a) we conclude that the well-known NaCl square unit cell is aligned with the Ag[1-10] and Ag[001] directions. This is in agreement with the LEED observations, in which it has been shown that NaCl[011]//Ag[1-10] and NaCl[01-1]//Ag[001]. This also could explain the epitaxial growth of sodium chloride films as NaCl(100) plane on

the Ag(110) surface. From figure 2.9a we can also notice some atomic-size vacancies in the NaCl film. These small defects have been reported previously [3] for NaCl(100) films on Cu(111) and they were identified as missing Cl^- ions in the NaCl ad-layer, which are labeled Cl vacancies.

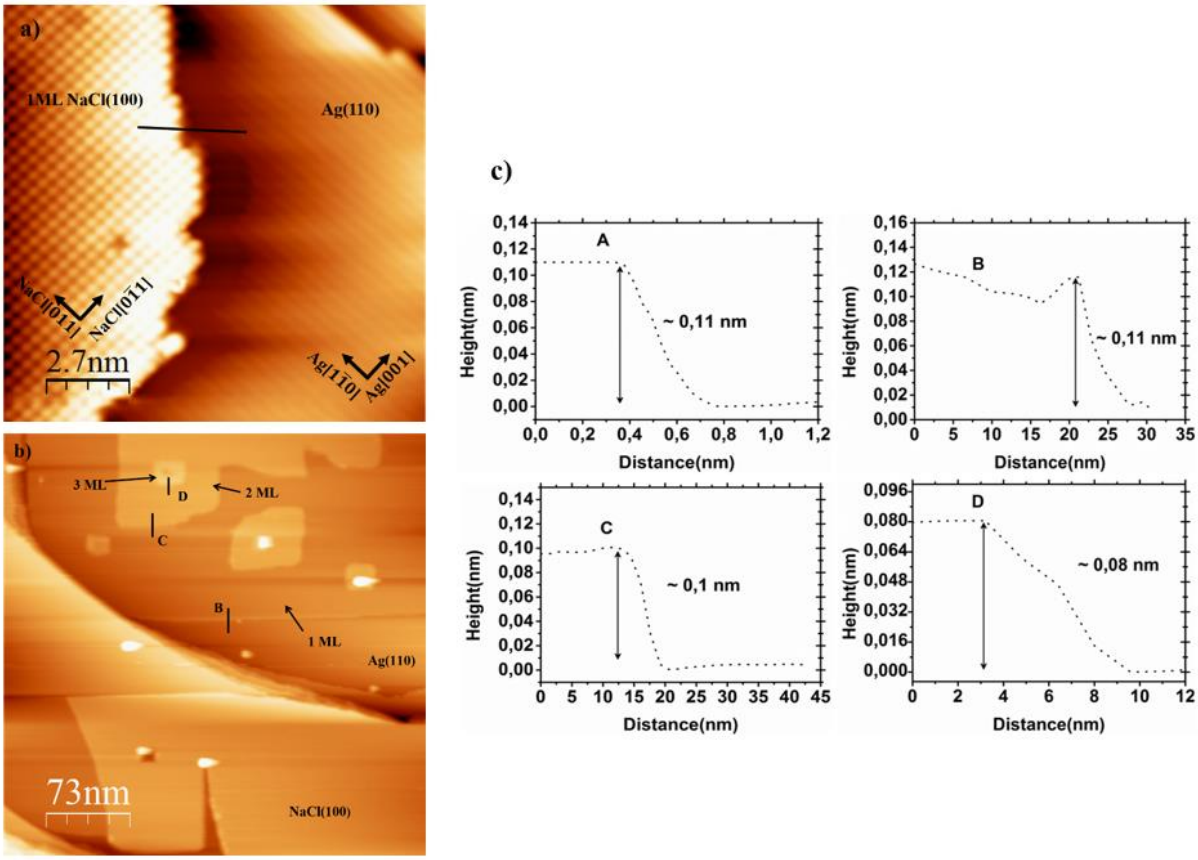

Fig. 2.9 STM images recorded at low temperature (78 K) of (a) ~0.3 ML NaCl film grown on Ag(110) with tunneling parameters (13.5 x 13.5 nm^2, U_b = -1.0 V, I_t = 0.4 nA), (b) ~1ML NaCl imaged with (366 x 366 nm^2, U_b = -1.0 V, I_t = 1.0 nA), (c) apparent height profiles along the lines in the STM images (a) and (b). During NaCl deposition the Ag(110) was held at 140 °C.

The local thickness of the NaCl islands could be estimated from the apparent height measured by STM. From figure 2.9a, the height profile measured on 0.3 ML coverage of NaCl film is ~0.11 nm which corresponds to one NaCl atomic layer. As can be seen from figure 2.9b, upon further deposition, the measured apparent heights of NaCl overlayers (mono-, bi-, and tri-layer) are 0.11, 0.10 and 0.08 nm, respectively. The observed decrease of the measured height is due to the increase of the number of NaCl ad-layers and it has already been found on NaCl

grown over Cu(311) substrate [25]. From the small value measured on the 0.3 ML NaCl coverage we conclude that the initial thickness of NaCl islands is one atomic layer. This observation is in agreement with the results of the growth of NaCl films on Al(111) and Al(100) [12], in which it has been demonstrated that the initial thickness of NaCl islands is one atomic layer and that the growth of the second and third ad-layers starts when depositing more than ~ 0.4 ML.

However, this conclusion disagrees with the case of NaCl grown on Ge (100), in which the growth mechanism is quite different because it has been found that the initial thickness of NaCl islands is two monolayers [34] without the need to reach a given amount of coverage. This difference is probably due to the different preparation conditions such as the substrate temperature.

We should also note that the measured apparent height for the NaCl layer of 0.11 nm is much smaller than the expected interlayer separation in bulk NaCl of 0.282 nm. This could be explained by the fact that, for insulating films such as NaCl, the tunneling barrier is not only determined by the vacuum between the tip and the NaCl film but also that the NaCl ad-layer itself should be taken into consideration as a barrier. The insulating character of the NaCl layers can perturb the tunneling between the STM tip and the Ag(110) metallic surface. Therefore, NaCl film grown over Ag(110) combined with the vacuum gap can be seen as a double barrier tunnel junction [35].

Figure 2.10a shows an atomic resolved STM image recorded on a NaCl island. The imaged atomic structure consists of a square lattice. We observe that NaCl consists of two configurations presenting the same (4x1) superstructure cell indicated by the dashed rectangles. The detail inside the (4x1) cell for each of the configurations is shown in figures 2.10a.1 and 2.10.a2 where we observe that the atomic pattern of intensities is different. The configuration in figure 2.10.a2 is the most commonly observed. In this configuration the measured distance between the first nearest neighbor bright spots is 0.395 nm along both [1-10] and [001] directions. This corresponds to the distance between the same ionic species in the NaCl(100) plane.

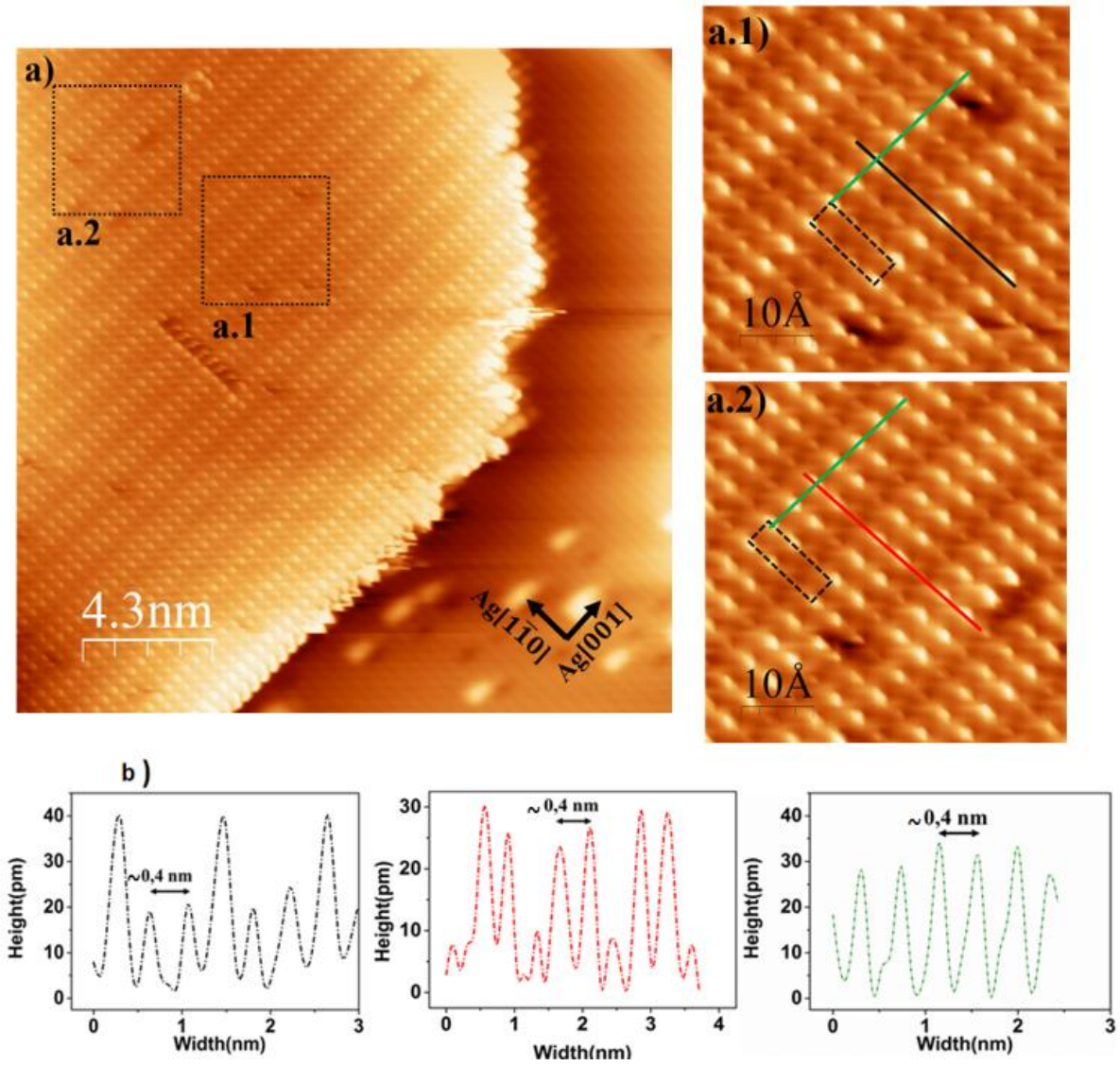

Fig. 2.10 (a) Atomically resolved STM image of NaCl island on Ag(110) surface recorded with the tunneling parameters (21.5 x 21.5 nm^2, U_b = -1.0 V, I_t = 0.4 nA); (a.1) and (a.2) (5 x 5 nm^2) showing parts of STM image (a); (b) line scans extracted from (a.1) and (a.2). The superstructure (4x1) is presented by the rectangular cell with black dashed line.

Our observation fits very well a previous assumption where it has been suggested that Na^+ and Cl^- ions arrange on the metallic surface in the same way as on the (100) plane of NaCl bulk. The atomic measured distance of NaCl films grown on Ag(110) indicates a lateral contraction of around 1.5% compared to the (100) plane NaCl lattice constant that can be calculated as follows $\frac{a_{NaCl}}{\sqrt{2}} = \frac{0.564}{\sqrt{2}} nm \approx 0.4\, nm$. This lateral contraction can be due to NaCl (100) surface reconstruction. From the analysis of the STM images of the figure 2.10, we

conclude that in STM, one type of ions (Na^+ or Cl^-) in NaCl film is imaged as protrusion, whilst the second atom is imaged as depression. That is in agreement with what is reported in the literature [36].

Based on the STM topography alone, it is not possible to determine which one of the two atoms of NaCl is imaged as a protrusion or depression. One can assume here that the imaged bright spots are Cl^- ions as their van der Waals radius is much bigger than the radius of Na^+ ($R_{Cl^-} = 181\ pm$ while $R_{Na^-} = 95\ pm$) [37]. This assumption is in agreement with DFT calculations performed by Hebenstreit et al. [12] where it has been confirmed that the imaged protrusions are the anions (Cl^-) considering the higher total density of occupied states at the chlorine sites.

Further density functional theory (DFT) calculations [38] have been performed to support the experimental results in this thesis. The theoretical investigation has been performed with and without van der Waals effects for four suggested NaCl/Ag(110) surface models, where one of the Cl atoms (labeled Cl_1) sits :

a) On atop site (see configuration 1 from figure 2.11)
b) On bridge site (see configuration 2 from figure 2.11)
c) On top site of the second silver layer (see configuration 3 from figure 2.11)
d) On bridge site of the second silver layer (see configuration 4 from figure 2.11)

The four optimized structures of NaCl monolayer on Ag(110) are shown in figure 2.11.

Analyzing the relative atomic positions of the silver, chlorine and sodium atoms resulting from the DFT calculations [38] it has been found that the NaCl monolayer grown on Ag(110) shows a buckling effect with an inter-layer Cl-Na separation around 0.26-0.27 Å for the configuration 1 and 2. Here, the Cl layer atoms sits higher than the Na layer about 2.8 Å above the Ag surface while the Na layer is about 2.6 Å above the substrate. The effect of Cl film buckling and its location higher than the Na layer may also support our assumption regarding that the atoms imaged with STM are the Cl atoms and not the Na atoms.

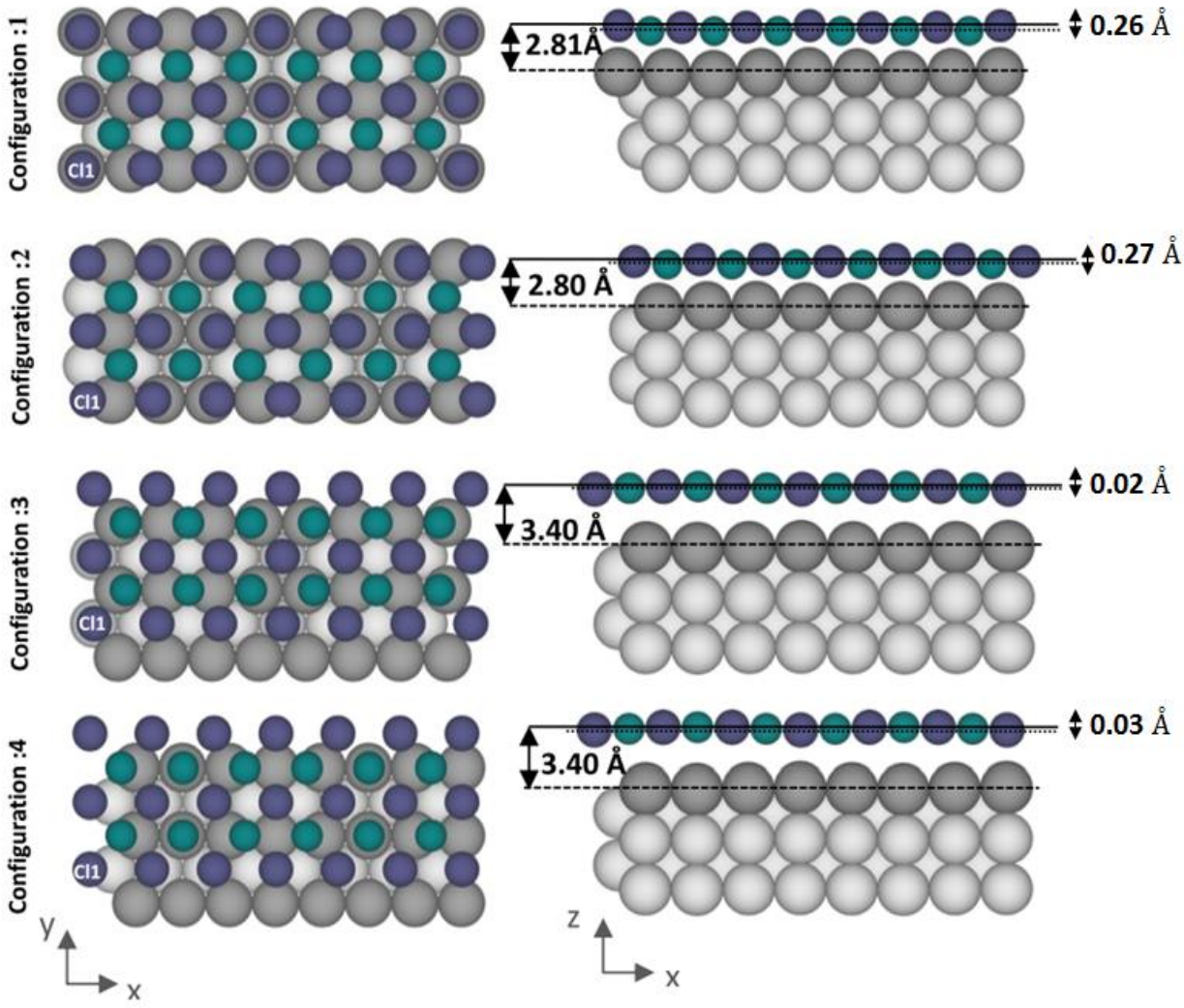

Fig. 2.11 Top and lateral view of the optimized four configurations of NaCl monolayer on Ag(110) used in DFT calculations. Dark gray, light gray, dark purple and green spheres correspond to Ag atoms in the first layer, Ag atoms in second layer, Cl atoms and Na atoms, respectively.

Further analysis of NaCl layer STM atomically resolved images in figure 2.10a1 and figure 2.10a2 shows clearly two configurations which we assign to the (4x1) superstructure already observed by LEED diffraction which demonstrated that the 4x1 Ag(110) surface can accommodate a slightly deformed 3x1 NaCl (100) surface. The two configurations are indicated by dashed rectangles and as can be seen, the spot intensities inside each configuration are different. Simulated STM images of NaCl film grown on Ag(110) surface agree with the experimental observations (see figure 2.12) and show two configurations in which the first one has a very bright spot (Cl_1 atom sits directly above an Ag substrate atom)

followed by two spots of lesser brightness (the other Cl atoms are near a bridge site). As for the second configuration, the simulated STM image shows a spot with weak brightness (Cl_1 atom on a bridge) and two very bright spots (the other Cl atoms sit nearly on top of the Ag surface atoms).

We should note that upon further STM surface imaging of NaCl films we noticed that these configurations looking like a Moiré pattern disappear for thicker islands. In fact, thicker islands will contribute to decrease the strain between the insulating ad-layer and metal substrate. As a result, the small lattice mismatch "3/4" between the Ag(110) surface and the NaCl(100) ad-layer will be reduced.

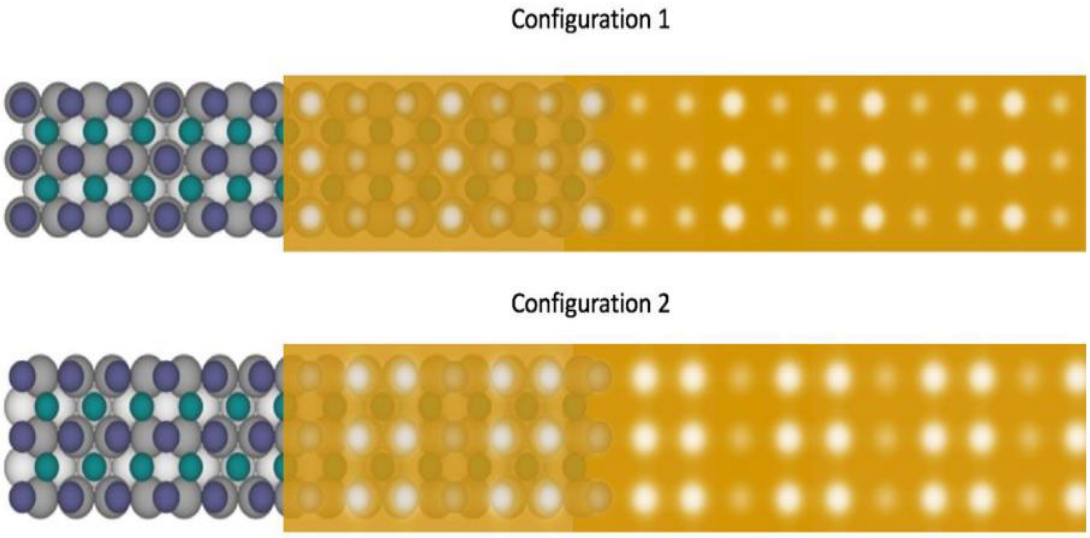

Fig. 2.12 calculated STM images using Hamman-Tersoff approach of NaCl on Ag(110) showing two configurations as observed with the atomically resolved STM topography. Dark gray, light gray, dark purple and green spheres correspond to Ag atoms in the first layer, Ag atoms in the second layer, Cl atoms, and Na atoms, respectively.

2.8. STS Measurements

Figure 2.13 shows a differential conductance $\frac{dI}{dU}$ spectrum as a function of U_{bias} recorded in constant height mode at low temperature (78 K) and taken with the tip positioned above a 1ML NaCl island. For tunneling out of occupied electronic states (negative sample bias), the density of states increases at -0.75 V, while for tunneling into the unoccupied states (positive

sample bias), a small LDOS peak is observed around +0.25 V. Between -0.75 and +0.25, the $\frac{dI}{dU}$ is essentially flat, which could be assigned to a small band gap of about 1 eV related to the thin film of NaCl grown on Ag(110). We should note that the measured gap value is lower than the expected band gap of bulk NaCl 8.7 eV [39]. However, it is known that the band structure of wide band gap materials such as NaCl or KCl could be strongly reduced when their size is changed from the macroscopic single bulk crystal to an ultra-thin film [40]. The peak around +0.25 V detected in STS for 1 ML NaCl could be associated to NaCl-Ag interface states or to the pure electronic states of the NaCl film.. In addition, the STM results presented above, in which the atomic resolution of the NaCl layer can be achieved at low tunneling parameters ($U_b = 1$V, $I_t = 0.4$ nA) may indicate the existence of localized metal-induced gap states at the NaCl-Ag interface which would allow imaging the insulating NaCl film even at low tunneling parameters [41].

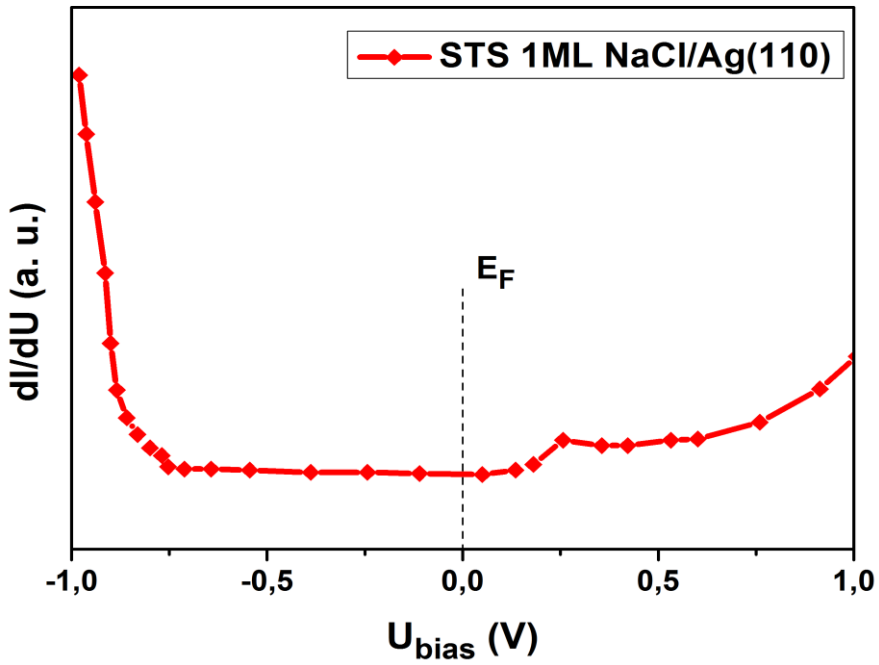

Fig. 2.13 Differential conductance STS spectra of ultrathin NaCl/Ag(110) film. Tip placed above 1ML NaCl island with tunneling parameters I_t=0.4 nA, U_b= -1V in open-loop conditions.

Through extensive STS investigation, it has been shown that upon deposition of NaCl ad-layers on Ag(001), the field emission resonances of the metallic substrate which occur at

energies ≥ 4.5 eV on bare surface will shift to lower energies [2]. The field emission resonances originate from image-potential states, i.e. unoccupied states which are above the metallic surface and have a free electron like dispersion. The shifted lower energy of these states is due to the reduction of the work function of the clean Ag surface upon adsorption of insulating films [42]. Our DFT calculations for NaCl grown on Ag(110) are in agreement with the previous reports and shows that upon NaCl deposition a reduction of Ag surface work function in the range of 0.4-0.7 eV is measured.

2.9. XPS Measurements

To provide chemical insights into the NaCl films, X-ray photoelectron spectroscopy has also been used as a complementary tool. By analyzing XPS spectra, the stoichiometry of the insulating film and the presence of potential contaminants can be inspected. High-resolution photoemission measurements were carried out on the TEMPO beamline at Synchrotron SOLEIL using a SCIENTA SES2002 electron spectrometer for variable incident x-ray photon energies. Photoemission spectra were collected with a high energy resolution of 50 meV resolving power, between 60 eV and 1100 eV. Figure 2.14 shows the Ag 3d core level spectra recorded at normal emission before and after deposition of the NaCl film. For the clean Ag(110) substrate, the Ag 3d spin-orbit split pair are located at binding energies of 368.27 and 374.2 eV for the $3d_{5/2}$ and $3d_{3/2}$, respectively, and are very close to that reported in literature (367.9 and 373.9 eV) [43]. As seen, after the deposition of NaCl the Ag 3d peaks are still located at the same energies with a negligible energy shift of ~0.08 eV. The unchanged position of the spin-orbit pair demonstrates that the Ag(110) surface atoms interact weakly with NaCl ad-layer atoms. Indeed, the DFT calculations [38] performed on NaCl/Ag(110) shows low binding energy between Ag surface and NaCl film in the range of 0.18-0.19 eV. Furthermore, the red circles in figure 2.14 indicate the plasmon loss peaks of silver. Those peaks are associated with a loss of a specific amount of energy as a result to the interaction between the photoelectron and other electrons (conduction band electrons). In this case the incident photoelectron will excite collective oscillations in the conduction band of the metal (free electron gas). After deposition of 1ML of NaCl, the plasmon peaks can still be detected. This can be seen as an indication of weak binding between the Ag(110) surface and the NaCl ad-layer.

Moreover, we should note the reduction of the silver XPS signal in figure 2.14 is due to the limited electron escape depth in the material (the loss of electrons travelling through the NaCl film).

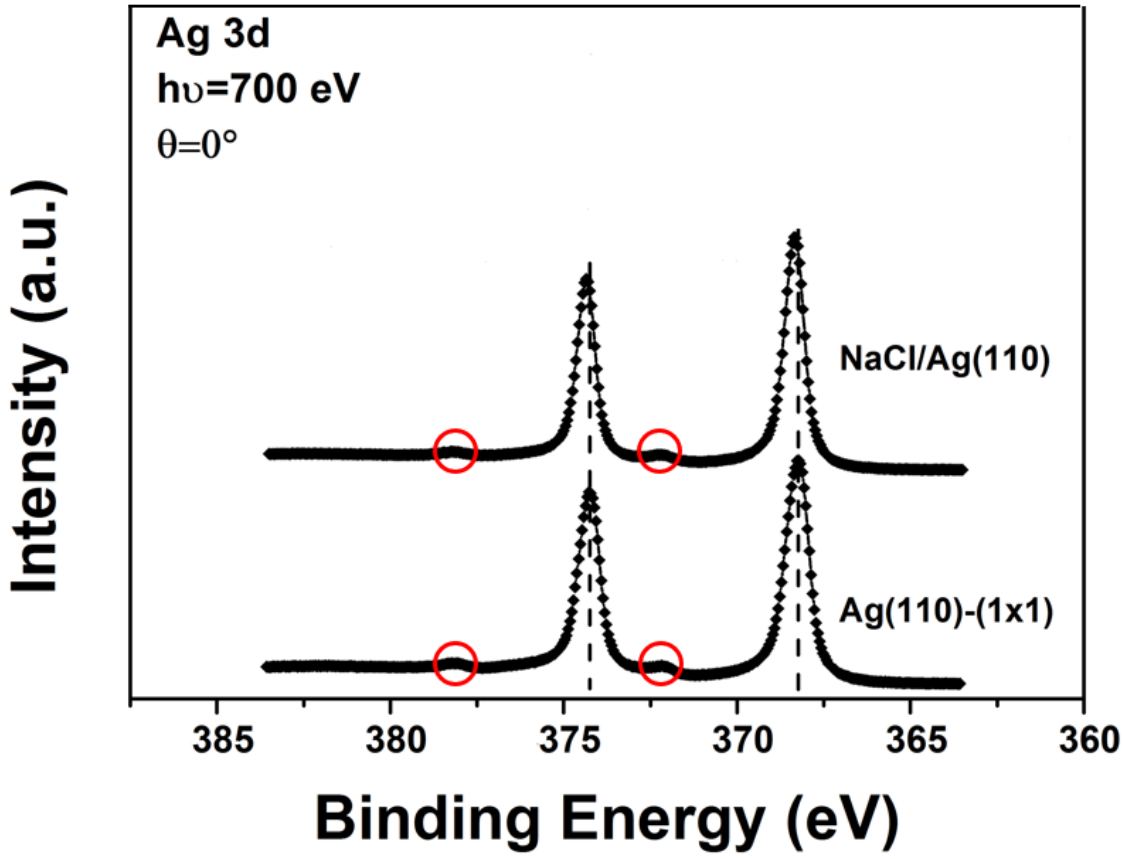

Fig. 2.14 XPS spectrum for Ag 3d peak measured on clean Ag(110) surface and after deposition of NaCl insulating films. Red circles indicate the plasmon loss peaks of Ag.

From a detailed analysis of the Na and Cl XPS spectrum (see figure 2.15) the following positions of the peaks can be obtained: Na2s 65.17 eV, $Cl2p_{1/2}$ 201.6 eV. These peak positions are different from the ones expected for each pure element (Na2s 63.5 eV and $Cl2p_{1/2}$ 202 eV) [44]. The chemical shift of the Na2s peak toward higher binding energy and $Cl2p_{1/2}$ toward lower binding energy is clearly in favor of a positive and negative charging of the Na and Cl, respectively, as expected for an ionic crystal such as NaCl.

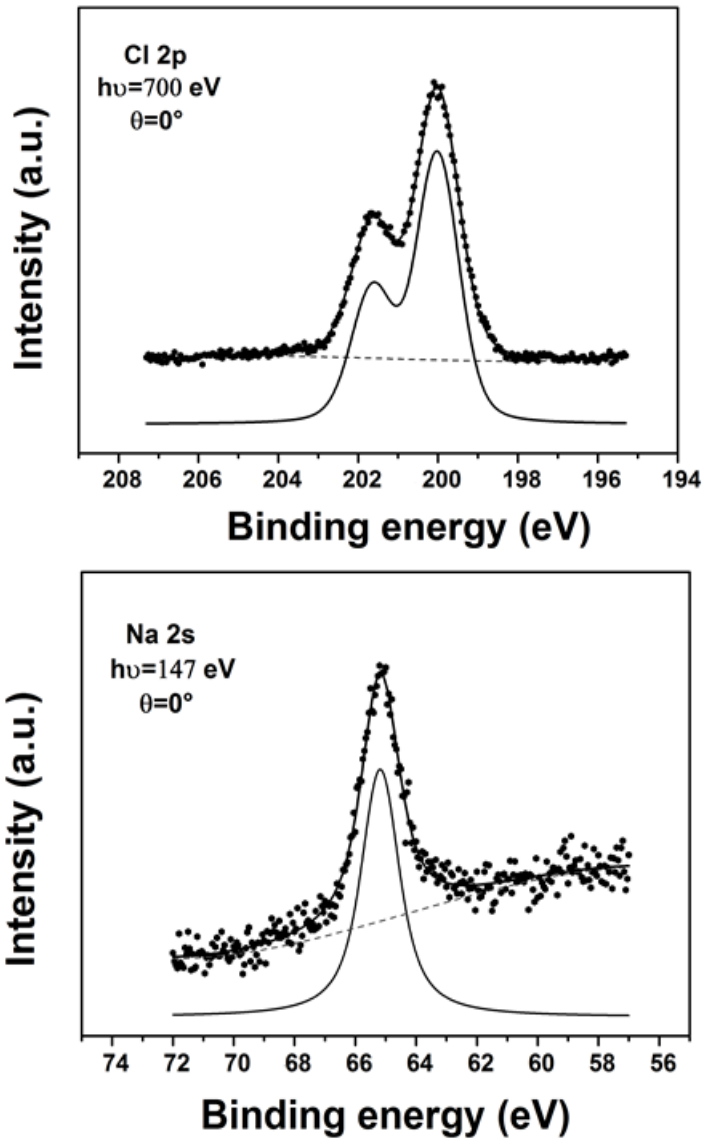

Fig. 2.15 XPS spectrum for Cl2p (top), Na2s (bottom) peaks measured on the 1ML NaCl deposited on Ag(110) sample.

The NaCl core level photoemission lines are analyzed with Doniach-Sunjic function line shape as described in the methods chapter (chapter 1). The parameters listed in table 2.1 are used.

	Na(2s)	Cl(2p)
Gaussian width	0.53 eV	0.83 eV
Lorentzian width	0.55 eV **0.45**[a] **0.79**[b]	0.12 eV **0.105**[c] **0.126**[d]
Asymmetry parameter	0	0
Spin-Orbit splitting	_____	1.63 eV
Branching ratio	_____	0.49

Table 2.1 Fitting parameters used for NaCl core levels Na(2s) and Cl(2p). Other reported values are a[45], b[46], c and d [47]. There are no spin-orbit splitting or branching ratio for s orbitals.

The fitting with one spin-orbit split component located at 201.6 eV and 199.99 for Cl($2p_{1/2}$) and Cl($2p_{3/2}$), respectively, indicates one Cl environment within the NaCl film. Its full width at half maximum (FWHM) is 0.56 eV which is in good agreement with other reported values [48]. On the other hand, fitting the Na(2s) spectra with one component (single peak) located at 65.17 eV and with a FWHM of 1.5 eV (in comparison with 1.65 already reported in [49]) demonstrates that Na ions have only one chemical environment which is the Cl ions. The best fit for both elements is obtained when the asymmetry parameter is set to 0. This is a clear evidence of the insulating behavior of NaCl given the fact that the asymmetry parameter characterizes the asymmetry contribution for a metal-like material

We should note that due to the highly ionic character of NaCl, adsorption is often governed by electrostatic interactions [22]. This adsorption often involves a charge exchange between the metallic substrate and ionic NaCl films in order to strengthen the Coulomb interaction. This charge transfer between the NaCl film and Ag surface has been demonstrated from DFT calculations of NaCl/Ag(110) [38] in which a small charge transfer value has been determined of around 0.24e from the ad-layer to the substrate.

2.10. ARPES Measurements

ARPES band mappings were made on a clean Ag(110) substrate and after deposition of 1ML NaCl. They were recorded at room temperature at low photon energy (60 eV) along the $\overline{\Gamma} - \overline{X}$ direction of the substrate and were acquired simultaneously at an angular range of $\mp 10°$. On the bare Ag(110) we observe the Ag *sp* band as indicated in figure 2.16a. Moreover,

Shockley-type surface states with a parabolic dispersion shape are localized close to the Fermi level. In general, any modification of the surface will be reflected on the existence and intensity of such Shockley states. Figure 2.16b shows the same ARPES measurement after the deposition of 1ML NaCl over the metallic surface. As we can see, the Ag *sp* band is still observed but we notice the absence of Shockley surface states. This indicates that the metallic surface is almost fully covered with NaCl layer.

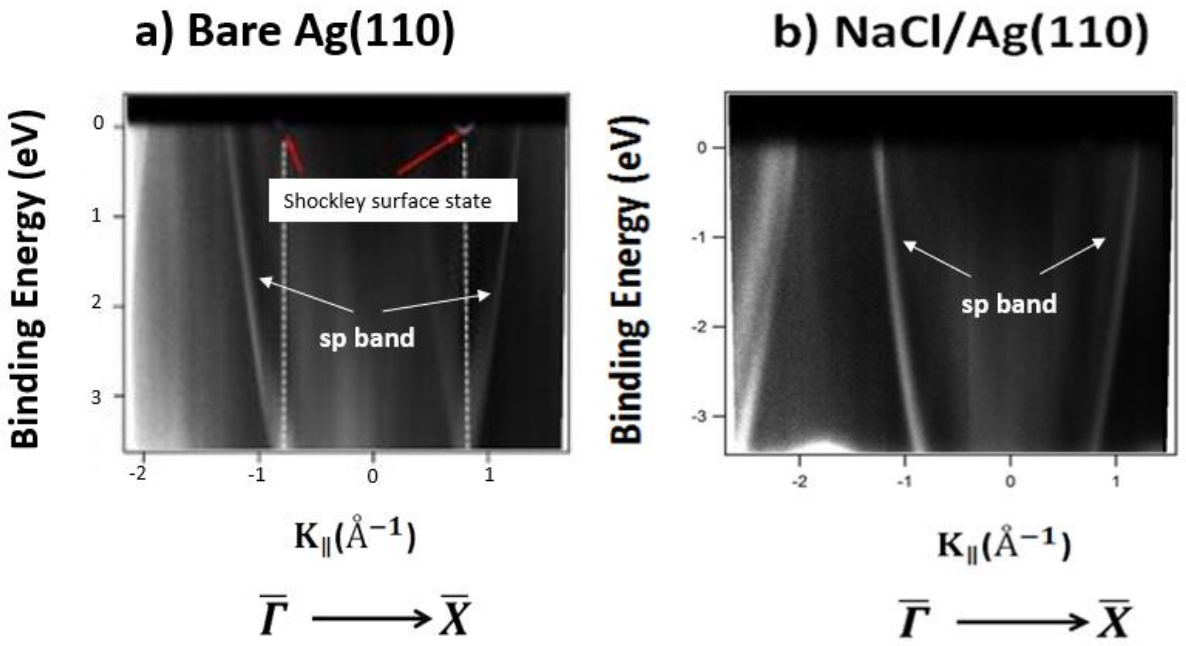

Fig. 2.16 High resolution ARPES measurements on a) clean Ag(110) and b) upon deposition of 1ML NaCl. The experiments were performed at room temperature at low photon energy of 60 eV.

Figure 2.17 shows the valence band photoemission spectra recorded at normal emission in the region close to the Fermi level for both the clean Ag substrate and after deposition of about 1ML NaCl. The peak with a binding energy around 0.3 eV in the upper curve corresponds to the Ag(110) Shockley-type surface state with the well-known nearly free-electron-like parabolic dispersion shape. In the subsequent spectrum we observe that the silver surface state has completely vanished. This indicates that deposited NaCl islands are covering the Ag(110) substrate which prevents the metallic surface state detection. Moreover, no extra states close to the Fermi level can be found and a decrease of the measured spectra intensity was observed (see figure 2.17). This could be due to the effect of the NaCl insulating film. Furthermore, if we assume that the Fermi level is located at the middle of the band gap of our insulating film

a small band gap around 2 x 0.28 = 0.56 eV can be estimated from the valence band spectra. This value is in the range of the measured band gap values using STS.

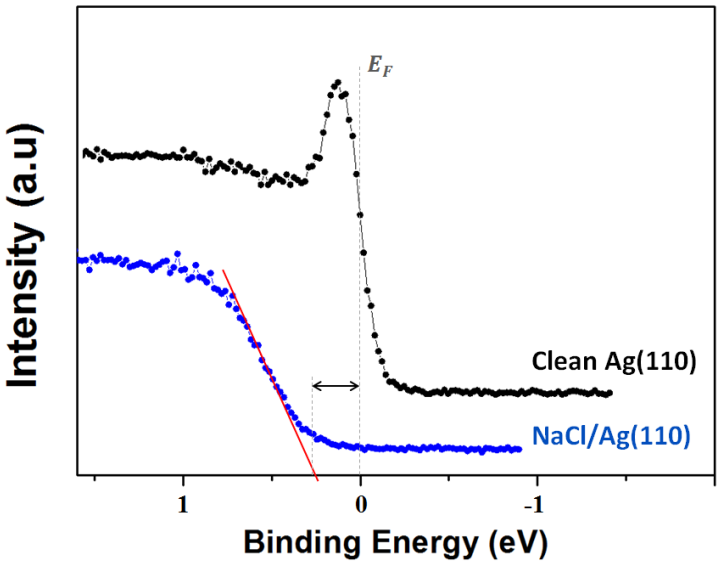

Fig. 2.17 Normal emission photoemission spectra obtained using low photon energy (60 eV) at room temperature for clean Ag substrate and after deposition of 1ML NaCl. The clean Ag(110) spectrum shows the Shockley-type surface at a binding energy around 0.3 eV. For 1ML NaCl deposition the peak corresponding to the Ag(110) surface state vanishes. Binding energies are referred to the Fermi level.

2.11. Conclusion

In this chapter, the experimental procedure, topography and electronic structure of epitaxial NaCl insulating films grown on Ag(110) substrate are studied.

We demonstrated that by optimizing the deposition parameters, large NaCl islands can be obtained. Indeed, keeping the Ag surface at 140°C during NaCl deposition produces NaCl islands large enough to start covering the metallic substrate. LEED pattern shows that the grown NaCl film have a (4x1) superstructure. This indicates a long range order for the NaCl film on Ag(110). The AES experiments reveal a Volmer-Weber growth mode for the NaCl islands. In such mode the growth of a second NaCl layer will start even before the initial NaCl layer is far from being complete. The STM images agree with the AES data and shows that the initial thickness of the NaCl film is one atomic layer and that the nucleation of the second

layer starts when reaching coverage of about 0.4 ML. A band gap of about 1 eV was measured using STS. This demonstrates the insulating character of the grown NaCl film. The XPS measurements reveal a weak interaction between the Ag surface and the NaCl film. The DFT calculations based on the calculated low binding energy between NaCl/Ag of about 0.18 eV support this observation.

Bibliography

[1] Schintke, S., Messerli, S., Pivetta, M., Patthey, F., Libioulle, L., Stengel, M., De Vita, A. and Schneider, W.D., 2001. Insulator at the ultrathin limit: MgO on Ag (001). *Physical Review Letters*, *87*(27), p.276801.

[2] Husseen, A., Le Moal, S., Oughaddou, H., Dujardin, G., Mayne, A. and Le Moal, E., 2017. Reaction kinetics of ultrathin NaCl films on Ag (001) upon electron irradiation. *Physical Review B*, *96*(23), p.235418.

[3] Repp, J., Meyer, G., Stojković, S.M., Gourdon, A. and Joachim, C., 2005. Molecules on insulating films: scanning-tunneling microscopy imaging of individual molecular orbitals. *Physical Review Letters*, *94*(2), p.026803.

[4] Cochrane, K.A., Schiffrin, A., Roussy, T.S., Capsoni, M. and Burke, S.A., 2015. Pronounced polarization-induced energy level shifts at boundaries of organic semiconductor nanostructures. *Nature communications*, *6*, p.8312.

[5] Leoni, T., Guillermet, O., Walch, H., Langlais, V., Scheuermann, A., Bonvoisin, J. and Gauthier, S., 2011. Controlling the charge state of a single redox molecular switch. *Physical Review Letters*, *106*(21), p.216103.

[6] Steurer, W., Repp, J., Gross, L., Scivetti, I., Persson, M. and Meyer, G., 2015. Manipulation of the charge state of single Au atoms on insulating multilayer films. *Physical review letters*, *114*(3), p.036801.

[7] Nilius, N., Rienks, E.D., Rust, H.P. and Freund, H.J., 2005. Self-organization of gold atoms on a polar FeO (111) surface. *Physical Review Letters*, *95*(6), p.066101.

[8] Repp, J., Meyer, G. and Rieder, K.H., 2004. Snell's law for surface electrons: Refraction of an electron gas imaged in real space. *Physical review letters*, *92*(3), p.036803.

[9] Mauch, I., Kaindl, G. and Bauer, A., 2003. Formation of NaCl stripes on Cu (1 0 0). *Surface Science*, *522*(1-3), pp.27-33.

[10] Pivetta, M., Patthey, F., Stengel, M., Baldereschi, A. and Schneider, W.D., 2005. Local work function Moiré pattern on ultrathin ionic films: NaCl on Ag (100). *Physical Review B*, *72*(11), p.115404.

[11] Calupitan, J.P.D.C., Guillermet, O., Galangau, O., Yengui, M., Echeverría, J., Bouju, X., Nakashima, T., Rapenne, G., Coratger, R. and Kawai, T., 2018. Adsorption of Terarylenes on Ag (111) and NaCl (001)/Ag (111): A Scanning Tunneling Microscopy and Density Functional Theory Study. *The Journal of Physical Chemistry C*, *122*(11), pp.5978-5991.

[12] Hebenstreit, W., Redinger, J., Horozova, Z., Schmid, M., Podloucky, R. and Varga, P., 1999. Atomic resolution by STM on ultra-thin films of alkali halides: experiment and local density calculations. *Surface Science*, *424*(2-3), pp.L321-L328.

[13] Loppacher, C., Zerweck, U. and Eng, L.M., 2003. Kelvin probe force microscopy of alkali chloride thin films on Au (111). *Nanotechnology*, *15*(2), p.S9.

[14] Zielasek, V., Hildebrandt, T. and Henzler, M., 2004. Measurement of NaCl/Ge (001) interface states by inelastic low-energy electron scattering with high momentum resolution. *Physical Review B*, *69*(20), p.205313.

[15] Fölsch, S., Barjenbruch, U. and Henzler, M., 1989. Atomically thin epitaxial films of NaCl on germanium. *Thin Solid Films*, *172*(1), pp.123-132.

[16] Anwar, J., Frenkel, D. and Noro, M.G., 2003. Calculation of the melting point of NaCl by molecular simulation. *The Journal of Chemical Physics*, *118*(2), pp.728-735.

[17] Sun, X. and Silly, F., 2010. NaCl islands decorated with 2D or 3D 3, 4, 9, 10-perylene-tetracarboxylic-dianhydride nanostructures. *Applied Surface Science*, *256*(7), pp.2228-2231.

[18] Guo, Q., Qin, Z., Liu, C., Zang, K., Yu, Y. and Cao, G., 2010. Bias dependence of apparent layer thickness and Moiré pattern on NaCl/Cu (001). *Surface Science*, *604*(19-20), pp.1820-1824.

[19] Ploigt, H.C., Brun, C., Pivetta, M., Patthey, F. and Schneider, W.D., 2007. Local work function changes determined by field emission resonances: Na Cl/ Ag (100). *Physical Review B*, *76*(19), p.195404.

[20] Cabailh, G., Henry, C.R. and Barth, C., 2012. Thin NaCl films on silver (001): island growth and work function. *New Journal of Physics*, *14*(10), p.103037.

[21] Chase Jr, M.W., Davies, C.A. and Downey, J.R., 1985. Jr., Frurip; DJ; McDonald, RA; Syverud. *J. Phys. Chem. Ref. Data*, *14*.

[22] Li, B., Michaelides, A. and Scheffler, M., 2007. Density functional theory study of flat and stepped NaCl (001). *Physical Review B*, *76*(7), p.075401.

[23] Bennewitz, R., Barwich, V., Bammerlin, M., Loppacher, C., Guggisberg, M., Baratoff, A., Meyer, E. and Güntherodt, H.J., 1999. Ultrathin films of NaCl on Cu (111): a LEED and dynamic force microscopy study. *Surface science*, *438*(1-3), pp.289-296.

[24] Ashcroft, N.W. and Mermin, N.D., 1976. Solid state. *Physics (New York: Holt, Rinehart and Winston)*, pp.131-151.

[25] Olsson, F.E., Persson, M., Repp, J. and Meyer, G., 2005. Scanning tunneling microscopy and spectroscopy of NaCl overlayers on the stepped Cu (311) surface: Experimental and theoretical study. *Physical Review B*, *71*(7), p.075419.

[26] Heidorn, S., Bertram, C., Koch, J., Boom, K., Matthaei, F., Safiei, A., Henzl, J. and Morgenstern, K., 2013. Influence of Substrate Surface-Induced Defects on the Interface State between NaCl (100) and Ag (111). *The Journal of Physical Chemistry C*, *117*(31), pp.16095-16103.

[27] Bruno, M., Aquilano, D., Pastero, L. and Prencipe, M., 2008. Structures and surface energies of (100) and octopolar (111) faces of halite (NaCl): an ab initio quantum-mechanical and thermodynamical study. *Crystal Growth and Design*, *8*(7), pp.2163-2170.

[28] Barbier, A., 1998. Generalized model for interface description. *Surface Science*, *406*(1-3), pp.69-89.

[29] Seah, M.P., 1973. Distinction between adsorbed monolayers and thicker layers in Auger electron spectroscopy. *Journal of Physics F: Metal Physics*, *3*(8), p.1538.

[30] Davis, L.E., MacDonald, N.C., Palmberg, P.W., Riach, G.E. and Weber, R.E., 1976. Handbook of Auger Electron Spectroscopy. *Physical Electronics Industries, Eden Prairie, MN*, *27*(6), p.l.

[31] Oura, K., Lifshits, V.G., Saranin, A.A., Zotov, A.V. and Katayama, M., 2013. *Surface science: an introduction*. Springer Science & Business Media.

[32] Castell, M.R., Wincott, P.L., Condon, N.G., Muggelberg, C., Thornton, G., Dudarev, S.L., Sutton, A.P. and Briggs, G.A.D., 1997. Atomic-resolution STM of a system with strongly correlated electrons: NiO (001) surface structure and defect sites. *Physical Review B*, *55*(12), p.7859.

[33] Bruno, M., Aquilano, D. and Prencipe, M., 2009. Quantum-mechanical and thermodynamical study on the (110) and reconstructed (111) faces of NaCl crystals. *Crystal Growth and Design*, *9*(4), pp.1912-1916.

[34] Glöckler, K., Sokolowski, M., Soukopp, A. and Umbach, E., 1996. Initial growth of insulating overlayers of NaCl on Ge (100) observed by scanning tunneling microscopy with atomic resolution. *Physical Review B*, *54*(11), p.7705.

[35] Schönenberger, C., Van Houten, H., Kerkhof, J.M. and Donkersloot, H.C., 1993. Single-electron tunneling in double-barrier junctions by scanning tunneling microscopy. *Applied Surface Science*, *67*(1-4), pp.222-227.

[36] Li, Z., Schouteden, K., Iancu, V., Janssens, E., Lievens, P., Van Haesendonck, C. and Cerdá, J.I., 2015. Chemically modified STM tips for atomic-resolution imaging of ultrathin NaCl films. *Nano Research*, *8*(7), pp.2223-2230.

[37] Wells, A.F., 2012. *Structural inorganic chemistry*. Oxford university press.

[38] Quertite, K., Lasri, K., Enriquez, H., Mayne, A.J., Bendounan, A., Dujardin, G., Trcera, N., Malone, W., El Kenz, A., Benyoussef, A. and Kara, A., 2017. Atomic Structure of Submonolayer NaCl Grown on Ag (110) Surface. *The Journal of Physical Chemistry C*, *121*(37), pp.20272-20278

[39] Lipari, N.O. and Kunz, A.B., 1971. Energy bands and optical properties of NaCl. *Physical Review B*, *3*(2), p.491.

[40] Alivisatos, A.P., 1996. Semiconductor clusters, nanocrystals, and quantum dots. *Science*, *271*(5251), pp.933-937.

[41] Arita, R., Tanida, Y., Kuroki, K. and Aoki, H., 2004. Electronic properties of metal-induced gap states at insulator/metal interfaces: Dependence on the alkali halide and the possibility of excitonic mechanism of superconductivity. *Physical Review B*, *69*(11), p.115424.

[42] Machado, M., Chulkov, E.V., Silkin, V.M., Höfer, U. and Echenique, P.M., 2003. Electron lifetimes in image-potential states at metal–dielectric interfaces. *Progress in Surface Science*, *74*(1-8), pp.219-237.

[43] Fuggle, J.C. and Mårtensson, N., 1980. Core-level binding energies in metals. *Journal of Electron Spectroscopy and Related Phenomena*, *21*(3), pp.275-281.

[44] Cardona, M. and Ley, L., 1978. Photoemission in solids I. *Photoemission in Solids I: General Principles*.

[45] Wertheim, G.K., Rowe, J.E., Buchanan, D.N.E. and Citrin, P.H., 1995. Experimental interatomic auger rates in sodium halides. *Physical Review B*, *51*(19), p.13669.

[46] Yafet, Y. and Watson, R.E., 1977. Interatomic Auger processes in NaCl. *Physical Review B*, *16*(2), p.895.

[47] Travnikova, O., Fink, R.F., Kivimäki, A., Céolin, D., Bao, Z. and Piancastelli, M.N., 2006. Disentangling the complex line profiles in the Cl 2p photoelectron spectra of Cl2. *Chemical physics letters*, *426*(4-6), pp.452-458.

[48] Patanen, M., Bancroft, G.M., Aksela, S. and Aksela, H., 2012. Direct experimental determination of the K 2 p and Cl 2 p core-level binding energy shifts between molecular and solid KCl: Line broadening effects. *Physical Review B*, *85*(12), p.125419.

[49] Barr, T.L. and Lishka, M.A., 1986. ESCA studies of the surface chemistry of zeolites. *Journal of the American Chemical Society*, *108*(12), pp.3178-3186.

Chapter 3. Growth of 2D Silicon Layer on an NaCl Ultra-Thin Insulating Film

As reported in the previous chapter NaCl ultra-thin insulating films can be grown to cover the metallic substrate of Ag(110). An important purpose set for this thesis was to investigate the adsorption and self-assembly of silicon atoms on these insulating films in order to obtain silicene or 2D silicon layer grown over them. In the next sections, *silicene*: *state of the art* and a detailed description of the experiments and studies that we made on this novel system are presented.

3.1. Silicene: State of The Art

The structural and electronic properties of the material that we now call silicene were studied for the first time in 1994 by Takeda and Shiraishi [1]. Using first principles calculations, they demonstrated that a buckled 2D silicon layer is more energetically favorable than a planar one.

In 2007, Verri and Voon [2] used for the first time the name “silicene”. Upon their investigation on planar silicon nanostructures using tight-binding Hamiltonians they showed that the planar structure of silicene would possess linear crossing bands around the Fermi level. Their reported results helped silicene to receive more attention across the nanomaterials community. Still, it was not accurate enough given the fact that the silicene planar structure that was used in their investigation was not the most energetically favorable configuration for the 2D silicon layer as had been shown before. This was confirmed later in 2009 by Cahangirov et al. [3]. Their calculations demonstrated that the flat silicene configuration have imaginary frequencies suggesting that this configuration is unstable. On the other hand,

buckled silicene shows positive phonon modes indicating the existence of restoring forces that can be generated in the case of any possible deformation.

After the Nobel Prize in physics was assigned to Geim and Novoselov for their work on graphene, silicene has been considered as the "next big thing" that may surpass the potential of graphene. Still, on the experimental side, the absence of a layered crystal counterpart such as graphite presents one of the biggest issues when aiming for 2D silicene synthesis. This form needed a more advanced nanofabrication process than the simple bottom-down method such as exfoliation used for graphene. For silicene, the bottom-up method by growing the 2D silicon layer on top of a substrate by means of physical vapor deposition (PVD) approach is considered the best growth method.

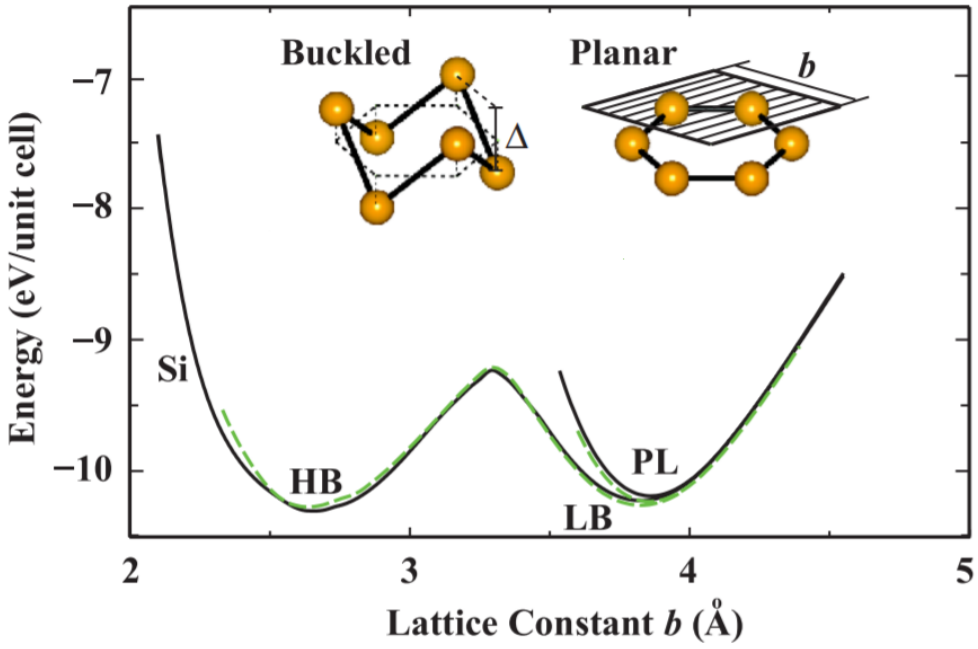

Fig. 3.1 Energy versus hexagonal lattice constant of 2D silicon layer is calculated for buckled and planar honeycomb structures. Black and dashed green curves of energy are calculated by LDA using PAW potential and ultra-soft pseudopotentials, respectively. Here planar (PL), low-buckled (LB), and high-buckled (HB) honeycomb structures correspond to distinct minima Image from [3].

One of the most used substrates for silicene growth was silver. The interest in this metallic material as a substrate comes from reverse system studies showing that when silver atoms are

deposited over silicon surfaces, an interface is produced without any silicide compounds [4]. Moreover, inspired by the theoretically reported results of the silicon 2D system and also their interesting physical properties, Aufray et al. [5] and De Padova et al. [6] published the first papers on the experimental synthesis of a silicene layer on Ag(110), forming what we call today silicene nanoribbons (NRs) (see figure 3.2). Angle resolved photoelectron spectroscopy (ARPES) investigations of silicene NRs revealed linear band states near the *K* point of silicene separated by a small gap of 0.5 eV located below the Fermi level [6]. The observed bands were assigned to π and π^* states corresponding to the Si $3p_z$ orbital. As for the shifted measured gap, it was assigned to the effect of the interaction between the silicene NRs and the Ag(110) substrate.

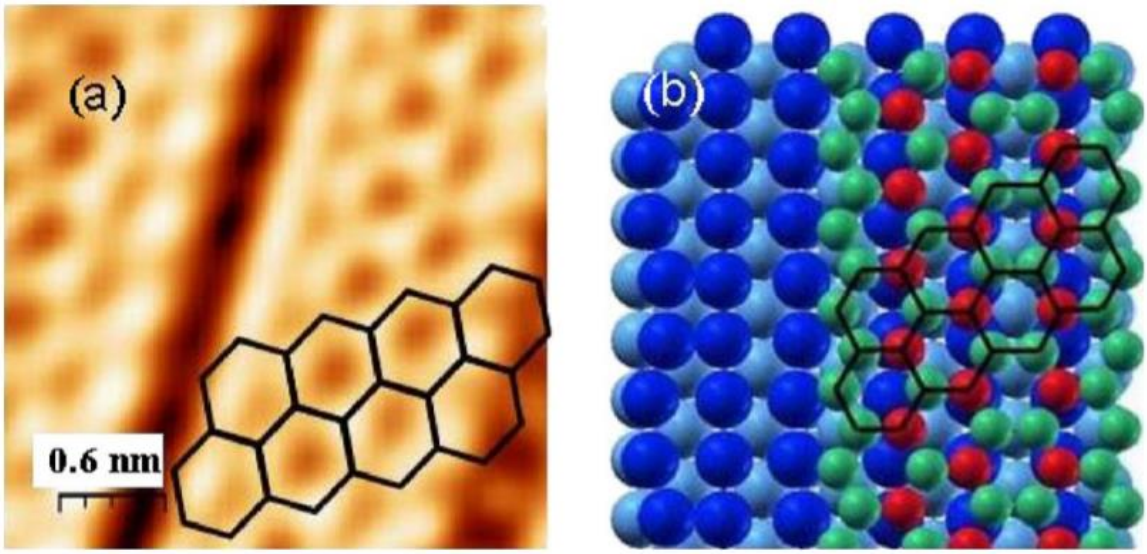

Fig. 3.2 Atomic structure of silicon NRs grown on Ag(110): (a) high resolution STM image showing honeycomb structure and (b) ball model of the silicene NRs layer where blue balls represent Ag atoms and green, red balls represent Si atoms. Images from [5].

By the end of 2010, Lalmi et al. [7] reported for the first time experimental evidence of a silicene sheet with a honeycomb lattice grown by epitaxy on Ag(111). Later, Vogt et al. [8] and Jamgotchian et al. [9] reported the existence of a new structure made by silicene sheet on Ag(111). The observed silicene sheet has a (3x3) superstructure which match (4x4) supercell of Ag(111) plane.

ARPES experiments conducted by Vogt et al. [8] on this 2D silicon layer suggested the existence of a Dirac cone resulting from linear dispersion of the π and π^* bands states near

the K point of silicene. A small gap (0.6 eV) was observed and was interpreted as a result of silicene monolayer interaction with the metallic surface of Ag(111). An estimation of the Fermi velocity from the ARPES results gave $\vartheta_F = 1.3\ 10^{-6}\ ms^{-1}$ which is close to the one already reported for graphene [10].

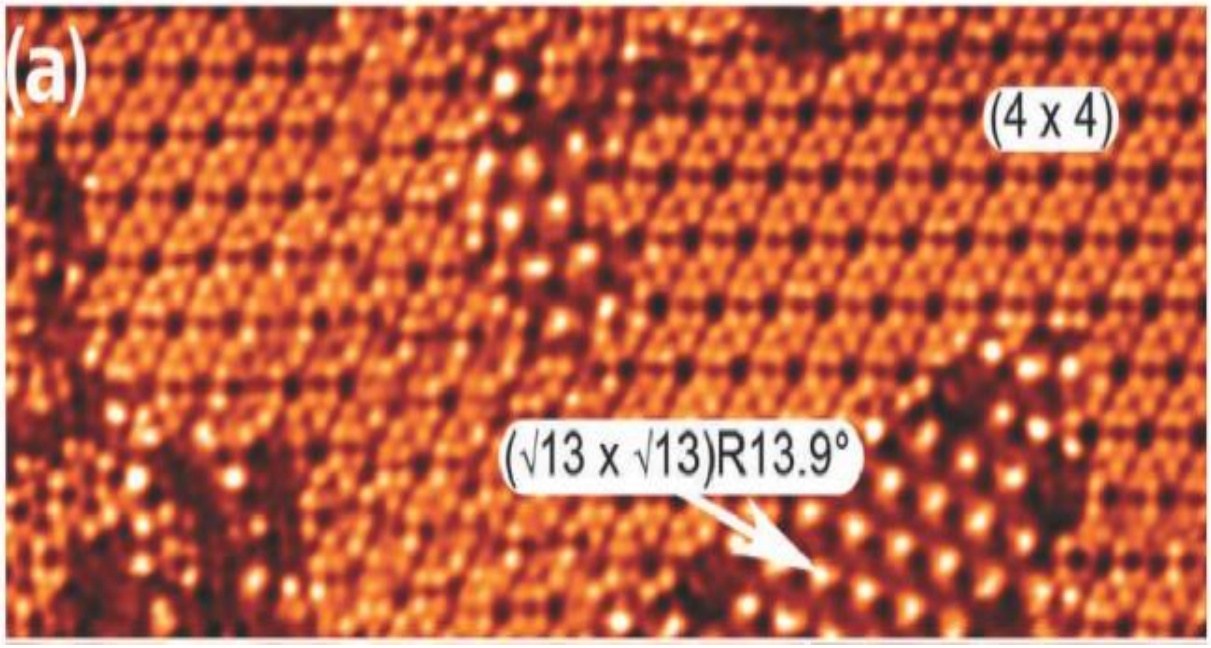

Fig. 3.3 Atomically resolved STM topography of silicene grown on Ag(111) showing an area on the sample which contains two silicene reconstructions known as $(\sqrt{13} \times \sqrt{13})$R13.9◦ and (4 × 4). Image reproduced from [11].

The silicene growth was not only limited to silver substrates as has been shown in 2012 by Fleurence et al [12]. In their paper they reported for the first time the growth of buckled silicene on ZrB_2(0001) surface. Following this work, Meng et al. [13] reported the growth of silicene on another metallic surface Ir(111). Their STM and LEED measurements show well-ordered buckled ($\sqrt{3}$ x $\sqrt{3}$) silicon layer. Gold also was used as a substrate for silicene growth studies, Enriquez et al. [14] reported the adsorption of silicon Au(110) and the formation of an ordered two dimensional surface alloy. Later on, the work of Sadeddine et al. [15] demonstrated the existence of Dirac cone in the electronic structure of a 2D silicon layer grown on Au(111).

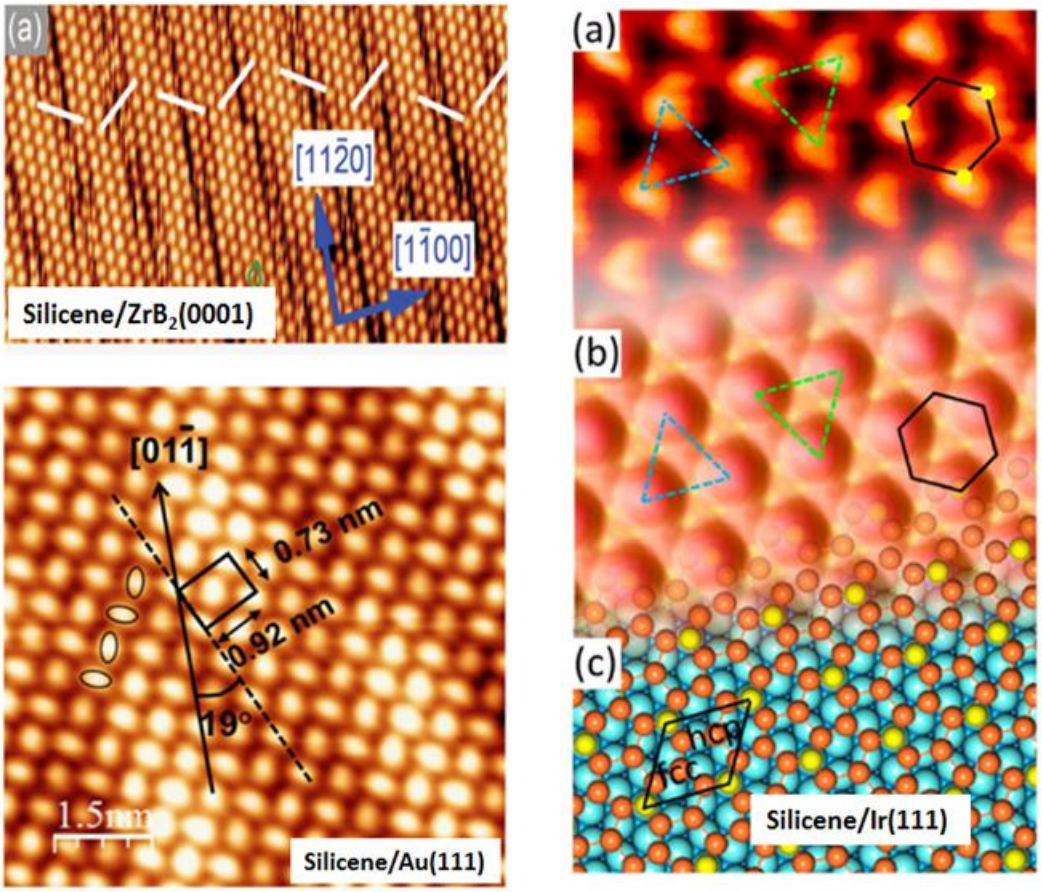

Fig. 3.4 STM images of silicene on ZrB_2(0001) [12], Ir(111) [13] and Au(111) [15]

While scientific groups were looking to enhance the quality of the silicene monolayer, others were still questioning the reality behind the observed linear bands of silicene. Lin et al. [16] claimed that the observed linear bands cannot be a concrete proof of the Dirac cone and that more studies were needed to clarify the electronic properties of silicene on Ag substrates. In other words, they stated that investigating the Landau levels by measuring the current-voltage I(V) using scanning tunneling spectroscopy under different magnetic fields could be a strong evidence for the Dirac cone [7]. The Landau level or Landau quantization is a quantum mechanics phenomenon in which charged particles (electrons) can only occupy orbits with discrete energy values when a magnetic field is applied. The number of electrons per level will be proportional to the value of the applied magnetic field. From these measurements, they concluded that silicene on Ag(111) does not possess the Dirac cone feature, and they assigned the observed linear bands to the Ag (sp) bands along the Γ- K direction. In this context, based on DFT calculations, Johnson et al. [8] suggested that the origin of the linear bands is

hybridized states between the Si(3p) and Ag(4d) localized at the surface. The reason behind the absence of silicene Dirac cone was assigned to silicene/substrate (silver) electronic interactions in which DFT showed that the hybridization between Si and Ag leads to a symmetry breaking which suppresses the Dirac quasiparticles [16]. It was also suggested that a weak charge transfer from the silicene layer to the silver surface would create slightly positively charged silicon atoms and a silver surface with Ag atoms that carries a negative charge. As a result, an electrostatic interaction between the silicene and the substrate would alter the intrinsic electronic properties of silicene and suppress the Dirac cone [19].

Other groups were interested in silicene growth beyond one monolayer for which it has been found that a new ($\sqrt{3}$ x $\sqrt{3}$) reconstructed structure of silicene can be grown on top of the (3x3) superstructure already grown over the (4x4) supercell of Ag (111) plane. These islands were interpreted as silicene multilayer [20].

Meanwhile, silicene functionalization started to get more attention because silicene oxidation was anticipated to alter strongly the structural and electronic properties of the 2D silicon layer. ARPES experiments showed that upon silicene oxidation (more than 600L) the Si-Ag hybridization can be broken. As a result the metallic Ag surface states can be observed again [21]. Silicene functionalization was not limited only on using oxygen and different ad-atoms have been explored [22]. Based on DFT calculations, it has been found that alkali metals such as Li can be adsorbed above the center of the hexagonal rings of silicene. Its binding energy to silicene is 2.4 eV. Using DFT calculations, a small charge transfer from the alkali ad-atom to silicene conduction band was calculated around 0.8 e. In this case, silicene could have a metallic behavior. On the other hand, alkaline-earth metals like Mg are adsorbed on bridge sites. Upon their adsorption, silicene starts to behave like a semiconductor with a narrow gap. At the opposite, transition metals such as Fe show a very strong chemical bonding with silicene (4.79 eV) due to their high electronic density of states in the d orbitals.

In the next sections, a detailed description of the experiments investigating the silicon layer growth on insulating films of NaCl grown over Ag(110) metallic surface is given.

3.2. Sample Preparation

The chemical vapor deposition (CVD) of silicon using a gaseous precursor like silane (SiH_4) is the typical mechanism used by manufacturers in order to make silicon-based photovoltaic

solar cells [23]. However, molecular beam epitaxy (MBE) has until now been the most efficient deposition method used for epitaxial silicene growth. In this method, we have a piece of silicon wafer of 1.5 x 0.5 cm^2 mounted in an ultra-high vacuum chamber (Pressure<10^{-9} mbar). The silicon wafer is attached to two poles of a vacuum feedthrough connected to an external power supply and fixed with tantalum plates able to resist high temperature. We heat directly the silicon wafer at 1100°C to start the silicon sublimation and the deposition on the substrate. A basic illustration of the PVD setup of epitaxial silicene is presented in figure 3.5.

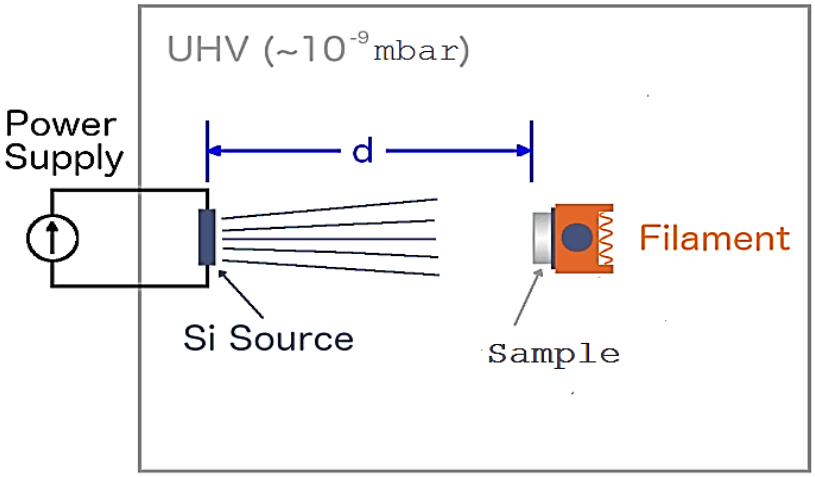

Fig. 3.5 Simple schematic of the PVD setup of epitaxial silicene used to prepare the surface in our experiments.

Since the silicon wafer is vulnerable to oxidation, Si source degassing has to be performed each time before use. Here, the degassing is achieved by slowly increasing the current through the wafer then performing multiple "flash degassing" at even higher current than the one used for sublimation (6.5 A at 5V). Prior to each silicon deposition the sample was prepared as described in the previous chapter (II.3). First cleaning the Ag(110) substrate by multiple cycles of sputtering to remove contaminants or any residues from previous preparations and then annealing at 480°C to allow surface recrystallization and provide a monocrystalline substrate (1x1)-Ag(110). Next, we let the substrate cool down by thermal radiation until reaching 140°C and then we start 1ML NaCl deposition with an evaporation rate of ~0.04 ML/min. After the NaCl deposition, we perform Si deposition for 40 min with an evaporation rate of ~0.02 ML/min and a post annealing for 3h at 140°C.

We should note that during our experiments, we found that silicon 2D growth on insulating films is not trivial. In fact, having to deposit in sequence NaCl films and then silicon ad-layer enhances the difficulties of the sample preparation.

3.3. First Attempts

LEED diffraction and STM images of the first silicene growth where 0.2 ML of silicon was deposited on 0.3 ML of NaCl films are presented in figure 3.6. During the silicon deposition process the substrate was kept at 100°C. As can be seen from figure 3.6c and figure 3.6d, it is clear that Si atoms prefer to adsorb on the bare Ag(110) surface by forming silicene nanoribbons with a periodicity of (2x5). This is observed in the LEED pattern (see figure 3.6a). The same silicene structure has been reported for Si/Ag(110) by several research groups [24,25]). NaCl islands show no evidence of Si atoms adsorption. The atomic vacancies observed in the NaCl islands in figure 3.6e correspond to defects and are labeled Cl vacancies and they are not due to Si deposition.

Figure 3.7 presents an STM image obtained after the deposition of 0.2 ML of silicon on 0.7 ML of NaCl. During the silicon deposition the substrate temperature was kept at 60°C. As can be seen, an interesting feature is observed on the NaCl islands in which silicon atoms tend to arrange as of Si dimers to form 1D stripes oriented along Ag[1-10].

We should note that more studies on the initial results obtained for Si/NaCl is not straightforward. This is due to the fact that clean metallic surface areas covered with Si ribbons with the (2x5) structure coexist with the new Si/NaCl structure. This is limiting its intrinsic characterization.

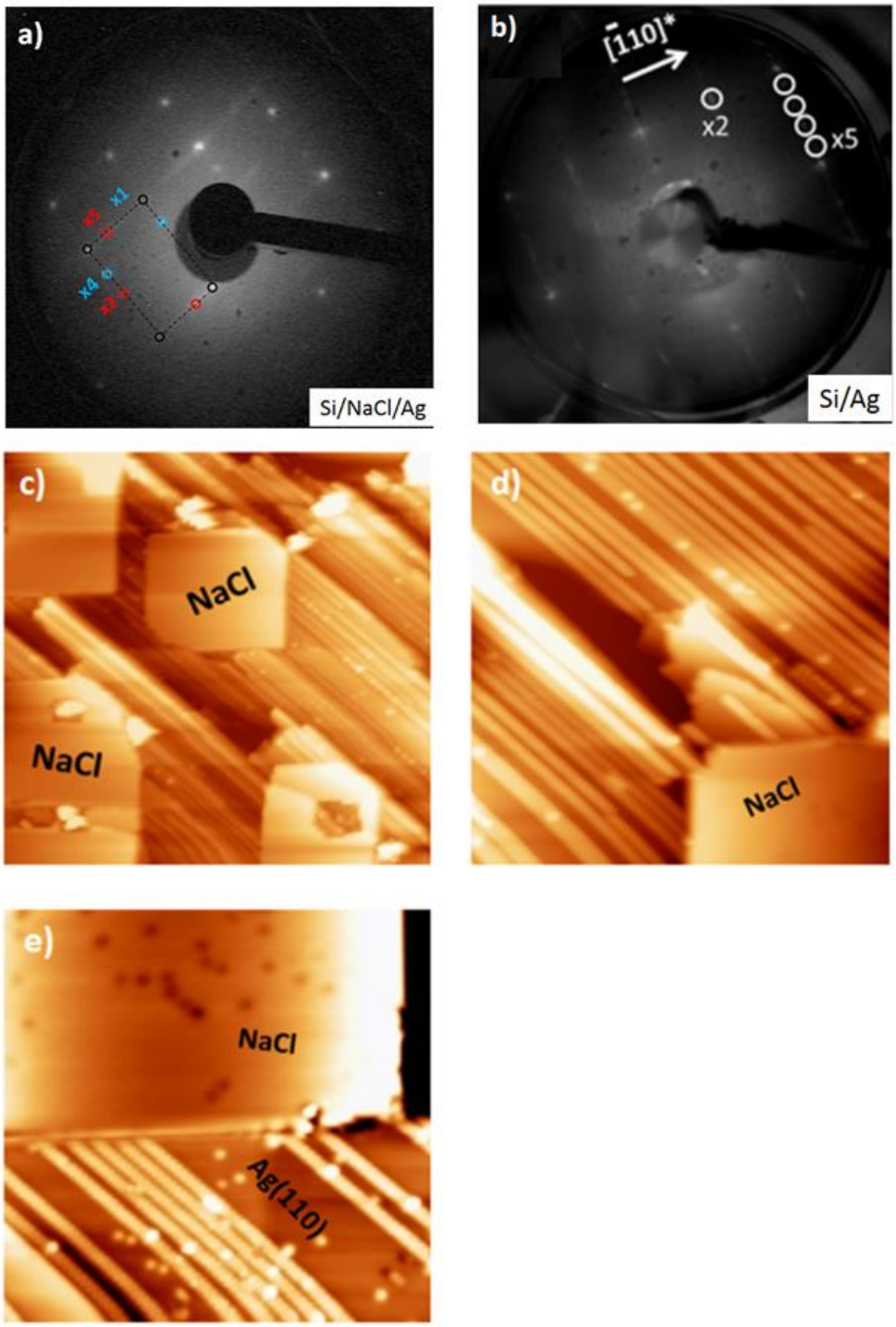

Fig. 3.6 LEED and STM images: (a) (2x5) and (4x1) LEED patterns assigned to silicene/Ag(110) and NaCl/Ag(110), respectively. (b) (2x5) LEED pattern of silicene on Ag(110) (c) STM image (105x105nm², V_b= -1,06V, I_t=1,01nA), (d) STM image (33,5x33,5nm², V_b= -1,06V, I_t=1,01nA) and (e) STM image (25x25nm², V_b= -1V, I_t=0,8nA) filled states topography revealing silicene NRs and clean NaCl islands. Image (b) is adapted from [25].

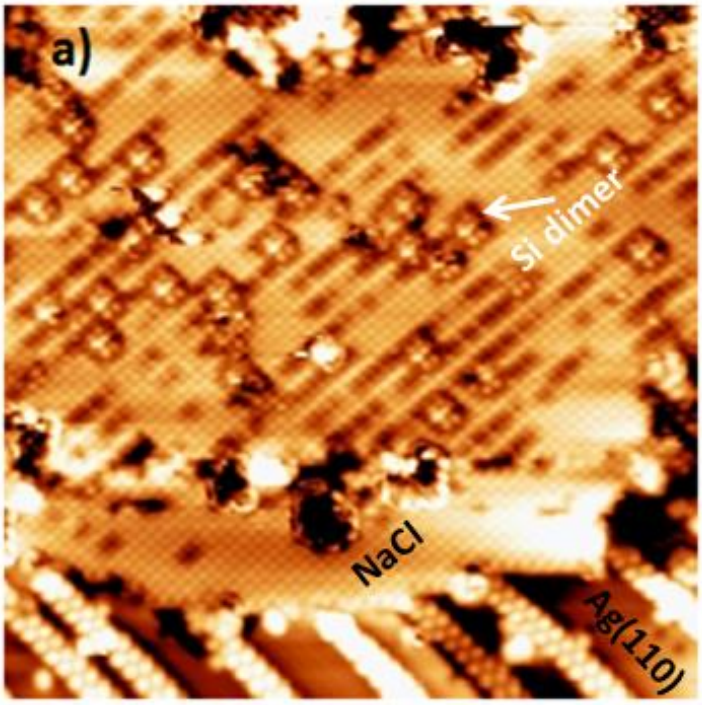

Fig. 3.7 STM image showing 0.2 ML silicon atoms self-assembled to form Si dimers on the NaCl islands (20x20nm², V_b= -1,16V, I_t=1,02nA). During the deposition the substrate temperature was held at 60 °C.

In the next sections, we present the results corresponding to the effect of increasing the NaCl and Si coverages and performing an annealing and a post-annealing at 140 °C. Here, more ordered silicon structure can be observed.

3.4. LEED Observations

Following this sample preparation:

(i) Increasing the coverage of NaCl to ~1ML and the Si to ~0.7ML
(ii) Annealing the substrate at 140°C during the silicon deposition
(iii) Performing a post-annealing at 140°C for 3hrs

We are able to obtain the LEED patterns shown in the figure 3.8, where figure 3.8a presents a clean Ag(110) surface with rectangular symmetry and figure 3.8b presents the characteristic (4x1) superstructure of NaCl grown on Ag(110). Figures 3.8c and 3.8d show the LEED diffraction pattern after silicon deposition over the NaCl/Ag(110) surface. As can be seen, a new (3x4) superstructure is observed with a periodicity of 3 x $a_{Ag[1-10]}$ = 0.86 nm and 4 x $a_{Ag[001]}$ = 1.6 nm. Figure 3.8d presents the LEED pattern of the surface after decreasing the

reciprocal space of the system. This helps to resolve more diffraction spots by using lower beam energy. The fact that the silicon (in red) and NaCl (in blue) diffraction spots do not match would suggest an incommensurate superstructure (see figure 3.9). Such incommensurate growth may indicate that the adsorbate layer is weakly bonded to the thin film [26].

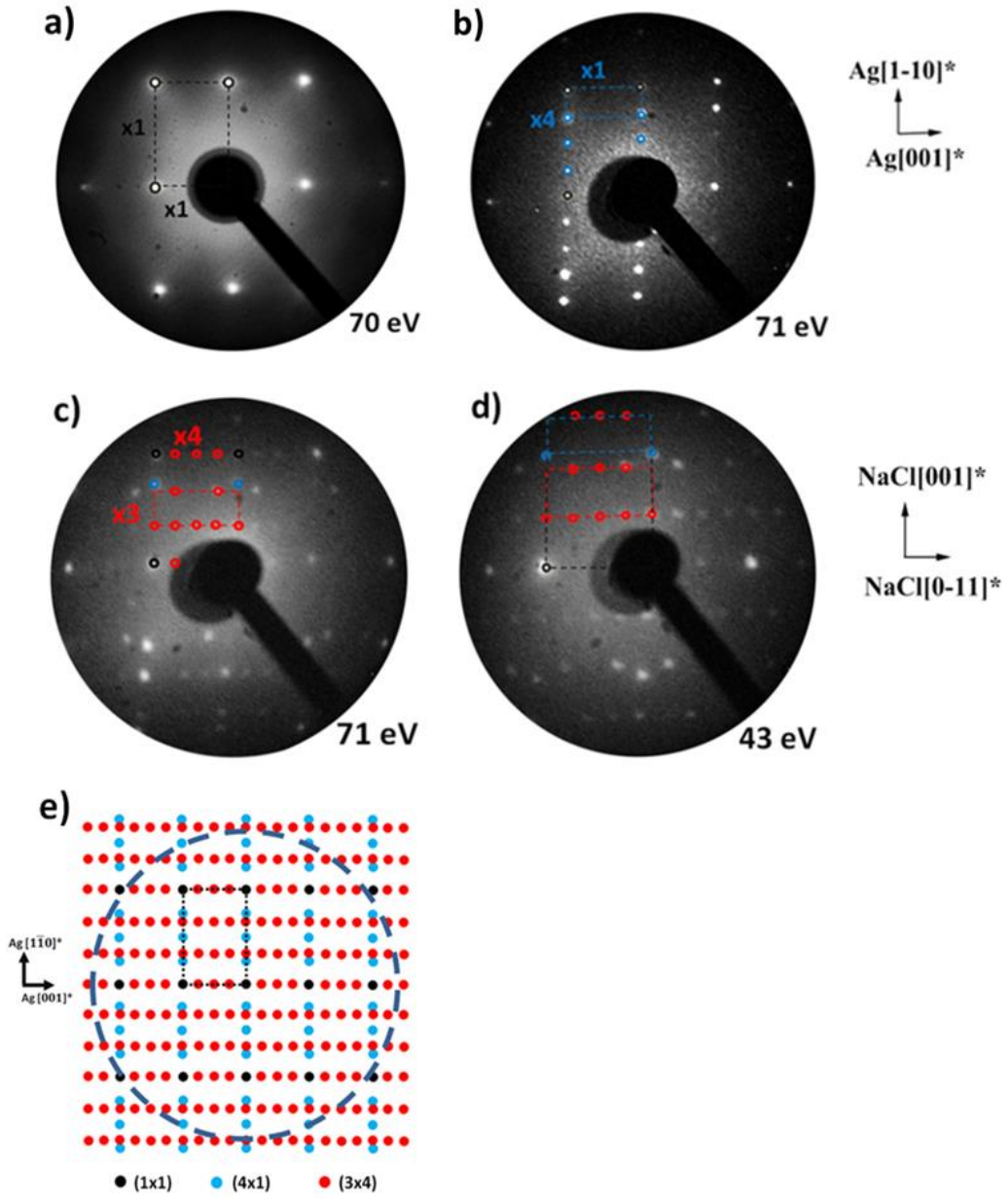

Fig. 3.8 LEED diffraction patterns of (a) clean Ag(110) substrate (b) after 1ML NaCl deposition (c) after deposition of 0.7 ML of silicon (d) after using lower beam energy (e) illustration shows the diffraction spots of Si/NaCl/Ag(110) system. The black, blue, and red dashed rectangles show the unit cell of the (1x1), (4x1), and (3x4) superstructures of Ag(110) pure, NaCl/Ag(110), and Si/NaCl/Ag(110) surfaces, respectively.

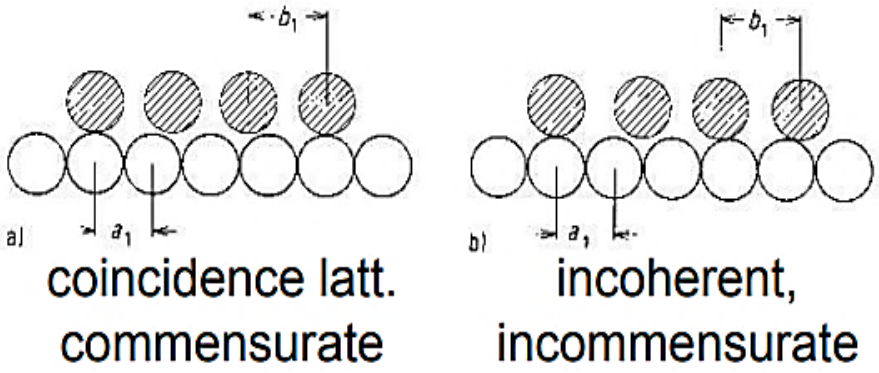

Fig. 3.9 Illustration showing the difference between commensurate and incommensurate structure.

3.5. AES Measurements

After deposition of Si/NaCl/Ag(110) following the process described above, Auger electron spectroscopy (AES) is performed (figure 3.1) in order to investigate the surface chemical composition. The spectrum is composed of peaks assigned to Ag (356 eV), Cl (181 eV) and Si (92 eV). The Na Auger peak cannot be detected due to its higher kinetic energy (KLL transition at 990 eV) and to its weaker ionization cross section compared to Ag and Cl [27].

From the spectrum we can also note the absence of any contaminants such as carbon (272 eV) or oxygen (503 eV). The silicon peak located at 92 eV demonstrates that silicon is not bonding with other chemical components such as chlorine or oxygen. In this case a shift towards lower kinetic energy would be seen for silicon (e.g. Si peak at 76 eV for SiO_2 [27]). This is a strong indication on the purity of the new formed silicon structure for which no oxidation or carbonization takes place.

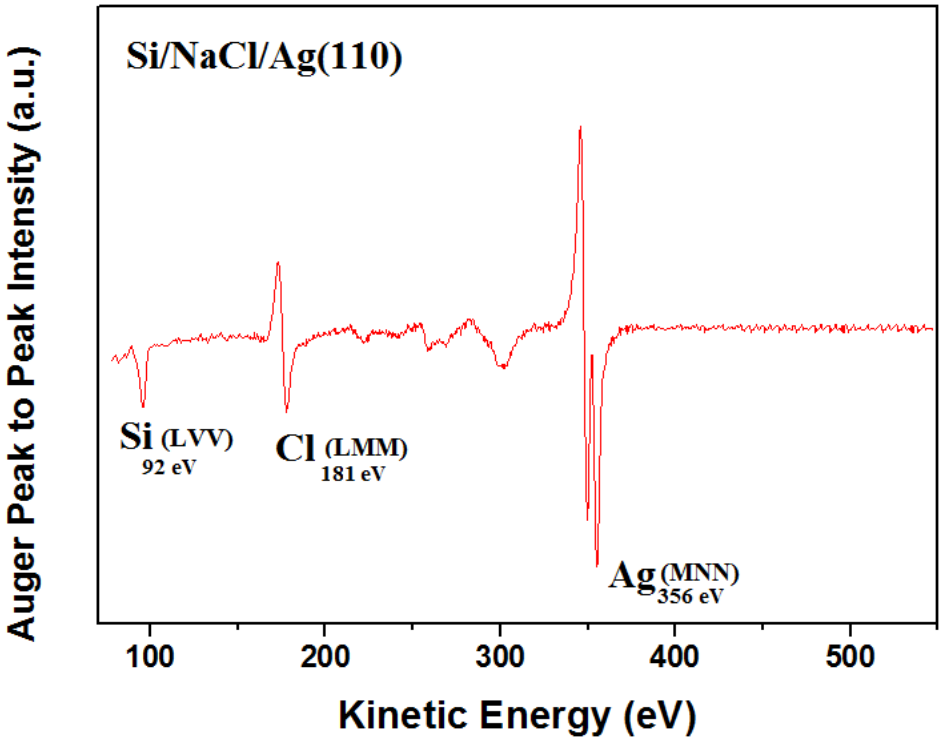

Fig. 3.10 Differential AES mode spectrum recorded from Si/NaCl/Ag(110) sample

3.6. STM Observations

To investigate the silicon 2D ad-layer in real space, we use STM to study its morphology and electronic structure. All the STM images were taken after the system had been cooled down to room temperature. Figure 3.11a shows large square shaped NaCl islands covering the Ag(110) surface. Figure 3.11b shows the same surface after silicon deposition (0.7 ML). The silicon ad-layer appears in quasi-continuous films with large areas extending over tens of nanometers. As can be seen, the grown silicon films mimic the square shape of the NaCl islands. Some free areas of Ag(110) surface are observed but no silicene (2x5) nanoribbons are found.

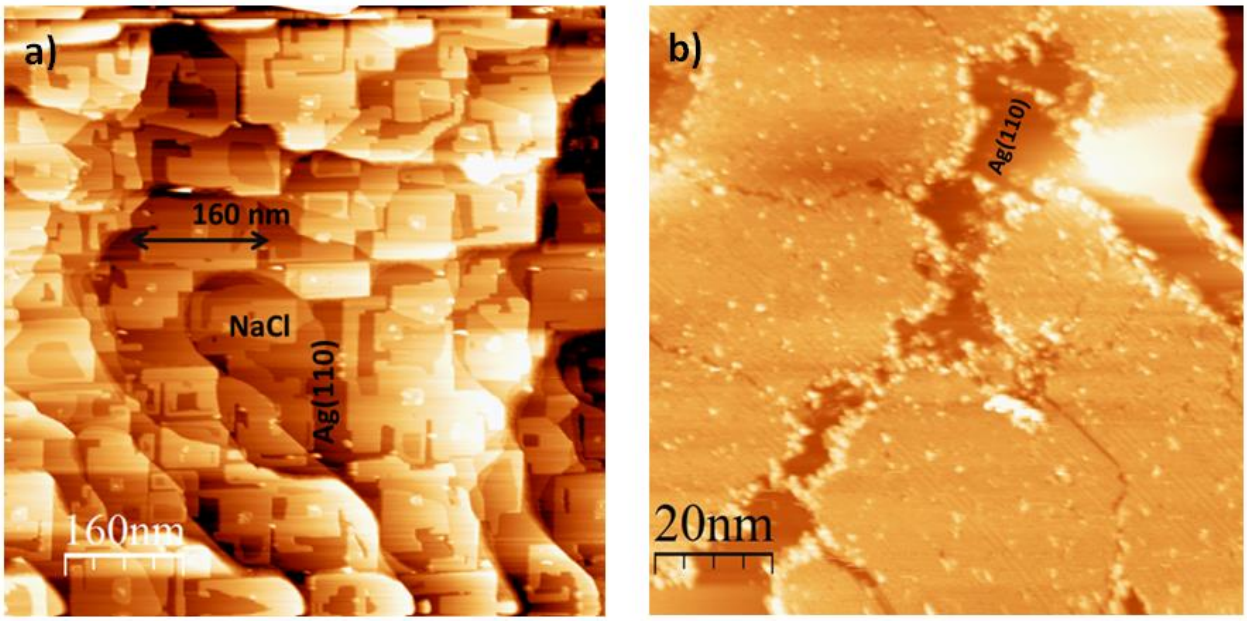

Fig. 3.11 STM images recorded at 77 K (a) 1ML NaCl islands covering Ag(110) substrate (800x800 nm², V_b= -1,05V, I_t= 0,95 nA), (b) 0.7ML of silicon deposited over the NaCl films (100x100 nm², V_b= -1V, I_t = 0,8 nA)

A further zoom-in gives us a better understanding of these films. The figure 3.12b shows an atomic resolved STM image obtained at high current (2.6 nA) and low bias voltage (-0.04 V). This image shows a highly ordered honeycomb-like lattice silicon structure. The measured line profile from this 2D silicon ad-layer agrees well with the expected superstructure from the LEED pattern and gives a distance of 0.86 nm that matches the periodicity of 3 x a $a_{\mathrm{Ag}[1-10]}$ = 0.864 nm. The line scans presented in figure 3.12c and figure 3.12d show that the unit cell of this honeycomb structure has a width of ~1.6 nm, which corresponds to 4xa Ag[001] = 1.63 nm. Furthermore, using the calculated atomic distances and the large size of the bright protrusions within the silicon nano-sheet, it is obvious that the bright spots observed in the STM images do not correspond to neighboring Si atoms and that the observed silicon honeycomb arrangement is indicative of a quasi-atomic resolution. From figure 3.12b it can be seen that the large atomic resolved spots have a triangular shape. The same pattern was observed on silicene/Ag(111) [8] and was interpreted as three Si atoms which form the so called “flower pattern”. Here a 3x3 reconstructed silicene matches 4x4 supercell of the Ag(111) surface.

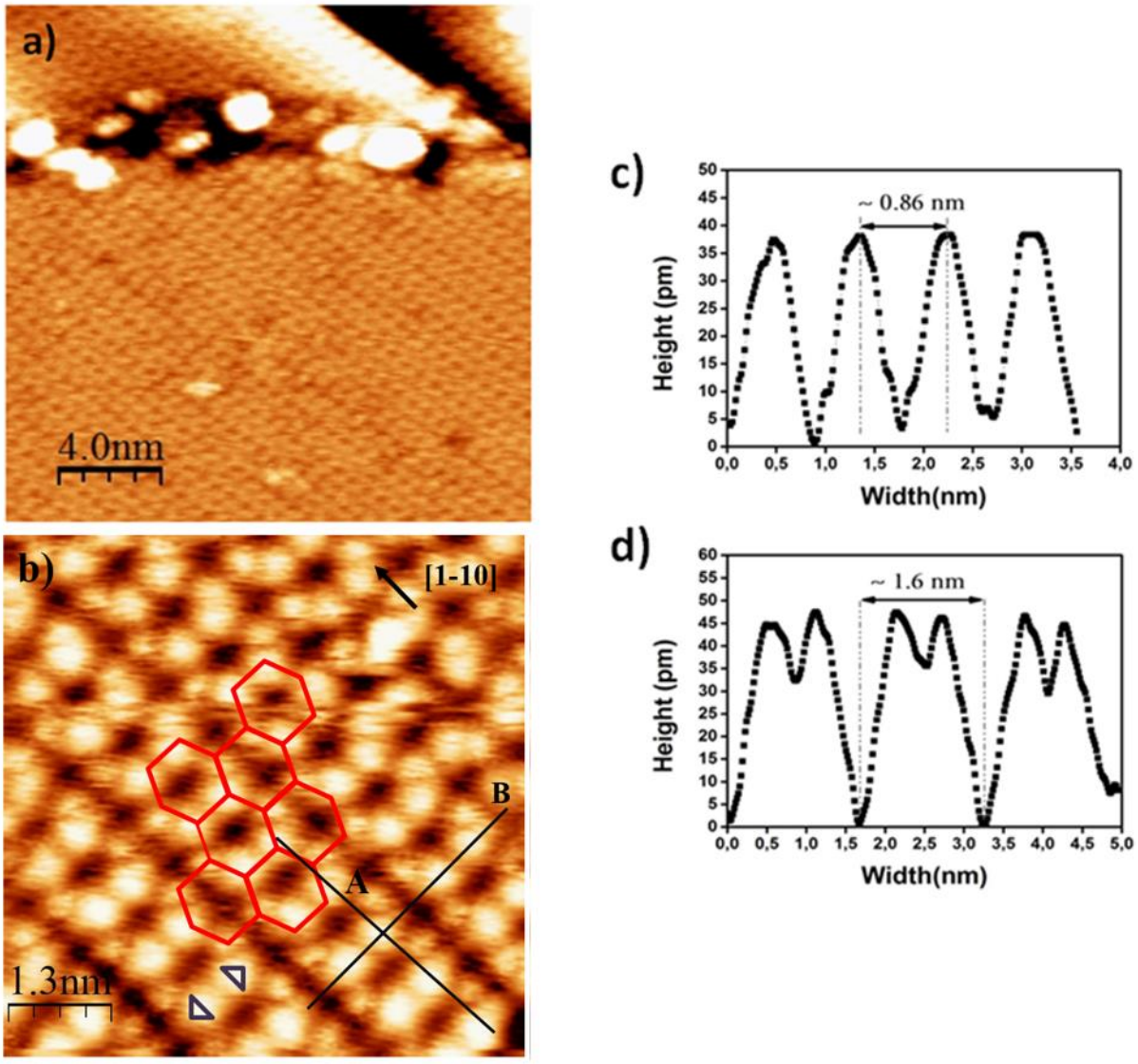

Fig. 3.12 Zoom-in for silicon ad-layer shown on Fig. 3.11b where (a) (20x20 nm², V_b = -0.7 V, I_t = 0.8 nA), (b) High-resolution STM image (6.5x6.5 nm², V_b= -0.04 V, I_t= 2.6 nA) showing the atomic structure of the deposited silicon self-assembled to form a honeycomb structure. (c) and (d) are line scans that belong to A and B, respectively. The triangles in black show the "flower pattern" of these structures.

To obtain a better understanding of the atomic geometry for the silicon superstructure, surface modelling and DFT calculations would be required. One can assume that the new ordered silicon structure could be a result of the mismatch (~ 2.8%) between the lattice parameters of the NaCl(100) and Si(111) planes. Given the fact that 3 x a_{NaCl} = 1.194 nm {a_{NaCl} = 0.398

nm is the first Cl-Cl or Na-Na distance in the NaCl(100)} surface and 3 x a_{Si} = 1.155 nm { a_{Si} = 0.385 nm is the second Si-Si neighbor distance in the Si(111) plane }.

Figure 3.13 shows the 2D silicon layer alongside the NaCl under-layer. The hexagonal lattice is not observed in the figure because of the tunneling parameters used to record the STM image. In order to atomically resolve the NaCl square symmetry, a low tunneling current should be used, whereas, the current must be higher for 2D silicon hexagonal atomic resolution.

The line scans from the figure 3.13a confirm the presence of two superstructures on the Ag(110) surface. Indeed, the line scan (A) shows a distance between NaCl spots of 0.4 nm corresponding to the square symmetry of NaCl(100) plane, and the line scan (B) shows the second structure related to silicon with a lattice distance of 0.86 nm as already shown in the LEED patterns. The key point of this STM image is to prove that the deposited silicon atoms are indeed adsorbed on top of the NaCl film. The Si atoms self-assemble to form a slightly distorted hexagonal structure on top of the insulating layer. To our knowledge, the observed silicon ad-layer represents the first observation of an extended 2D silicon assembly on an insulator material.

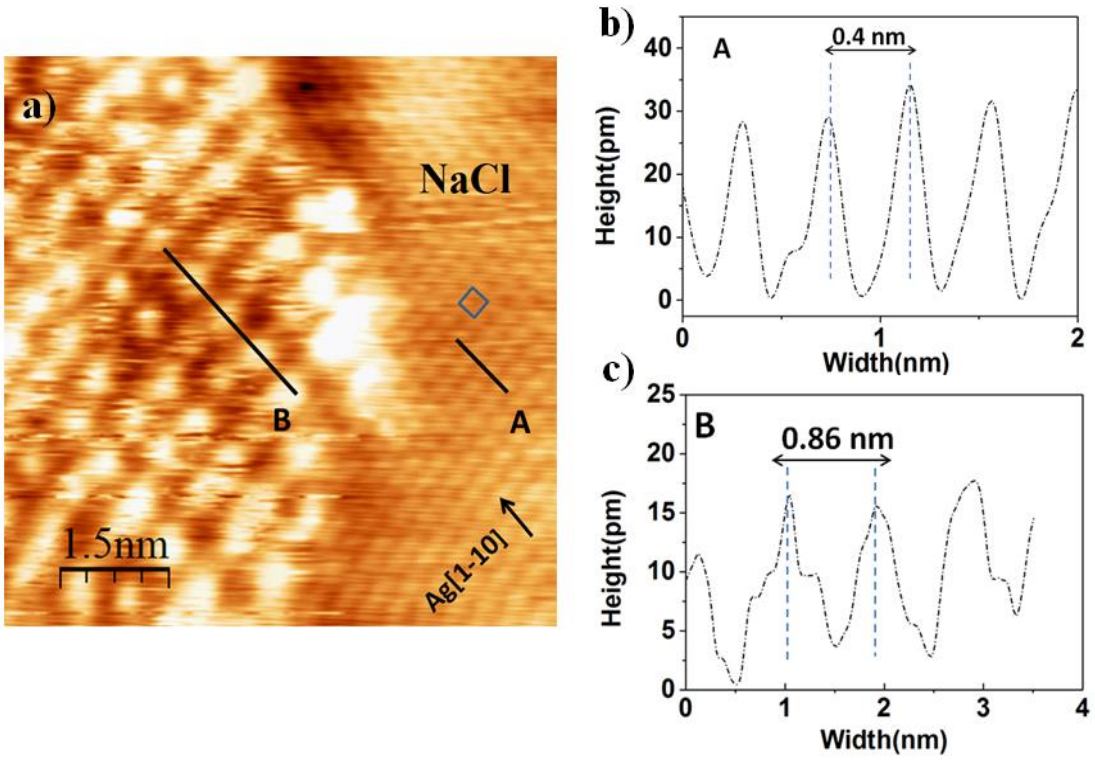

Fig. 3.13 (a) STM image of a silicon layer deposited on NaCl film (7.7x7.7nm², V_b= -0,6V, I_t=0,87nA). (b) and (c) are the lines profiles obtained along the black lines (A) and (B), respectively. The blue square shows the NaCl unit cell.

3.7. STS Measurements

In figure 3.14a, the curves obtained by STS are presented with the current versus voltage (I-V) on the NaCl film and silicon ad-layer.

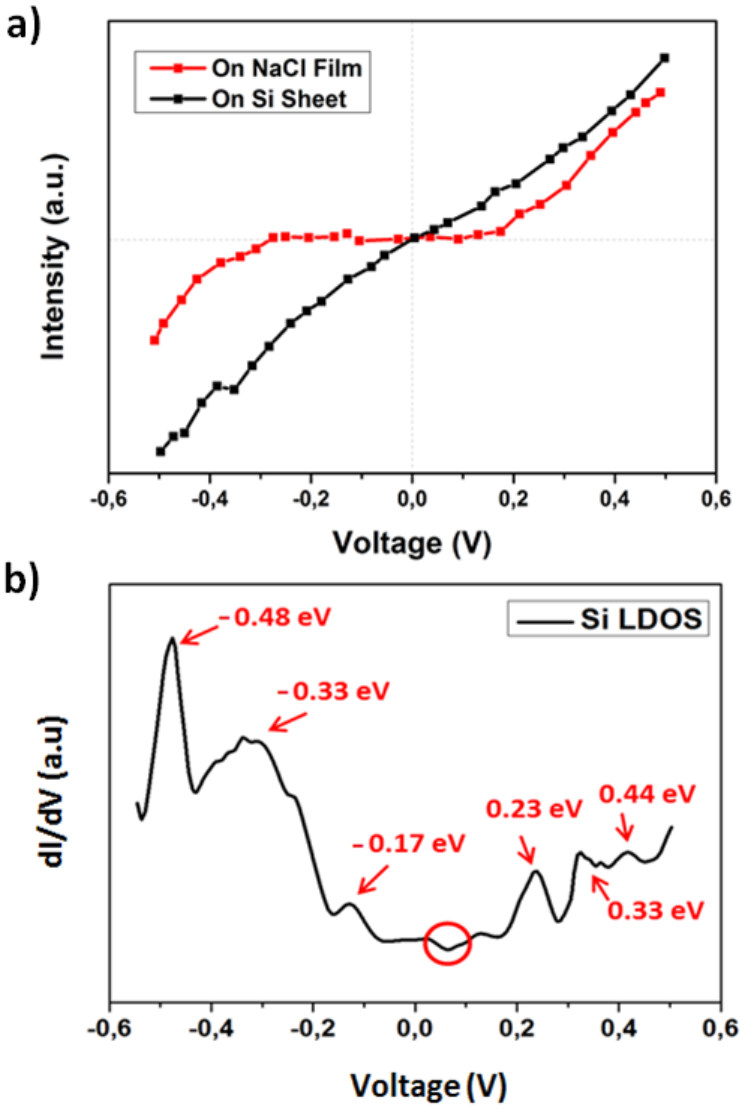

Fig. 3.14 Scanning tunneling spectroscopy measurement recorded at 77 K. (a) I-V curve registered on NaCl and silicon. We observe a straight line around the Fermi level (located at 0.0 V) showing the metallic character. (b) Local density of states (dI/dV) of silicon sheet in (a). Before recording the curve, the tip-surface distance is adjusted by closing the feed-back

loop and setting the current set point and V the sample bias voltage to 1 nA and 0.6 V, respectively.

From the STS spectra in figure 3.14a it is clear that the silicon 2D network has a metallic character. Figure 3.14b presents the local density of states (LDOS) calculated from the (I-V) curve which can be related to the electrical conductivity. Besides the pronounced filled states at -0.48 eV, -0.33 eV, -0.17 eV and empty states at 0.23 eV, 0.33 and 0.44 eV, the LDOS shows a finite density at the Fermi level with a minimum close to the Fermi level. The small V-shaped dip (see red circle in figure 3.14b) located near E_F at about 0.07 eV could be seen as an indication of a Dirac cone of silicene. A similar STS spectrum feature was reported for silicene on Ag(111) [16]. The dip in the dI/dV curve is not very clear compared with that of graphene [28] but it is more intense and clear than the one observed on silicene/Ag(111). The reason why the dip is smaller in the case of silicene/Ag(111) was interpreted as a result of the pronounced electronic density of states of the underlying metallic Ag(111) substrate superimposed in the dI/dV spectra. We should note that the V-shaped dip usually presents the density of states originating from the Dirac cone structure, which was proved for graphene on graphite [29]. However, this spectrum feature observed in the STS curve is not a solid evidence of the existence of the Dirac cone.

However, we should note that our STS results are quite different from those reported by Houssa et al. [30] in which their DFT simulation shows that depositing silicene on an insulator having hexagonal symmetry such as AlN ultrathin insulating graphite-like films enhances the sp^2-hybridization of the silicon atoms. This will preserve the gapless semiconducting (semi-metallic) behavior of its two-dimensional honeycomb network. The difference between the two results could be due to the different crystallographic symmetries of both surfaces, i.e., square and hexagonal symmetry for NaCl and AlN insulating film, respectively.

3.8. XPS Measurements

In this part, we present high-resolution Si 2p x-ray photoelectron (XPS) spectra of epitaxial silicene on NaCl(100) thin film. It is well established that such core level spectra are very sensitive to the chemical environment of the excited atom. High-resolution photoemission measurements are carried out on the TEMPO beamline at the Synchrotron SOLEIL using a

SCIENTA SES2002 electron spectrometer for variable incident x-ray photon energies. Photoemission spectra were collected with a high energy resolution (of the order of 50 meV resolving power) between 60 eV to 1100 eV. After silicon deposition the measurements are made at room temperature and the photon energy is set to 147 eV for Si (2p). Figure 3.15 shows the Ag (3d) core level spectra recorded at normal emission before and after deposition of the NaCl film and Si ad-layer. For the clean Ag surface, the Ag (3d) spin-orbit pair are located at 368.27 eV and 374.2 eV for $3d_{5/2}$ and $3d_{3/2}$, respectively. The measured binding energies values are close to the values reported in literature (367.9 eV and 373.9 eV) [31]. No major energy shift of the Ag (3d) peaks is observed after the growth of NaCl and the deposition of silicon ad-layer. This observation could be interpreted as a weak bonding between the elements of the sample (weak interaction between silver, NaCl and silicon). Furthermore, figure 3.15 shows plasmon loss peaks of Ag indicated by the red circles. As can be seen from the recorded Ag(3d) spectra for NaCl/Ag(110) and Si/NaCl/Ag(110), the plasmon peaks are still observed. This indicates a weak interaction between the Ag substrate and the adsorbate.

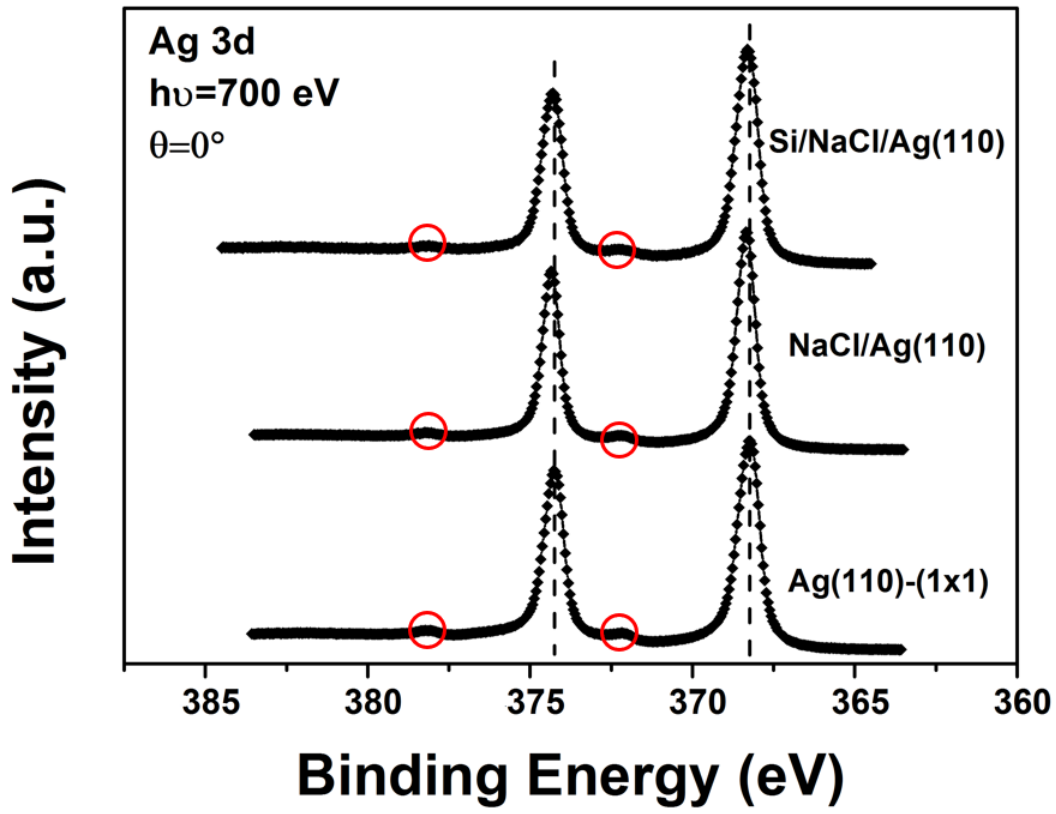

Fig. 3.15 XPS spectra of Ag 3d peak measured on clean Ag(110) substrate, after deposition of ~1 ML NaCl and after deposition of 0.7 ML Si

Figure 3.16c and 3.16d show the Si (2p) core level spectra of the ad-layer silicon for 0° normal emission (bulk sensitive) and 50° off-normal emission (surface sensitive), respectively. We can notice that the Si peaks do not show any additional components or peak energy shifts that can be raised due to oxidation processes (located between 101 and 103.5 eV) or due to carburization reactions to form $Si_{(1-x)}C_{(x)}$ compounds [32].

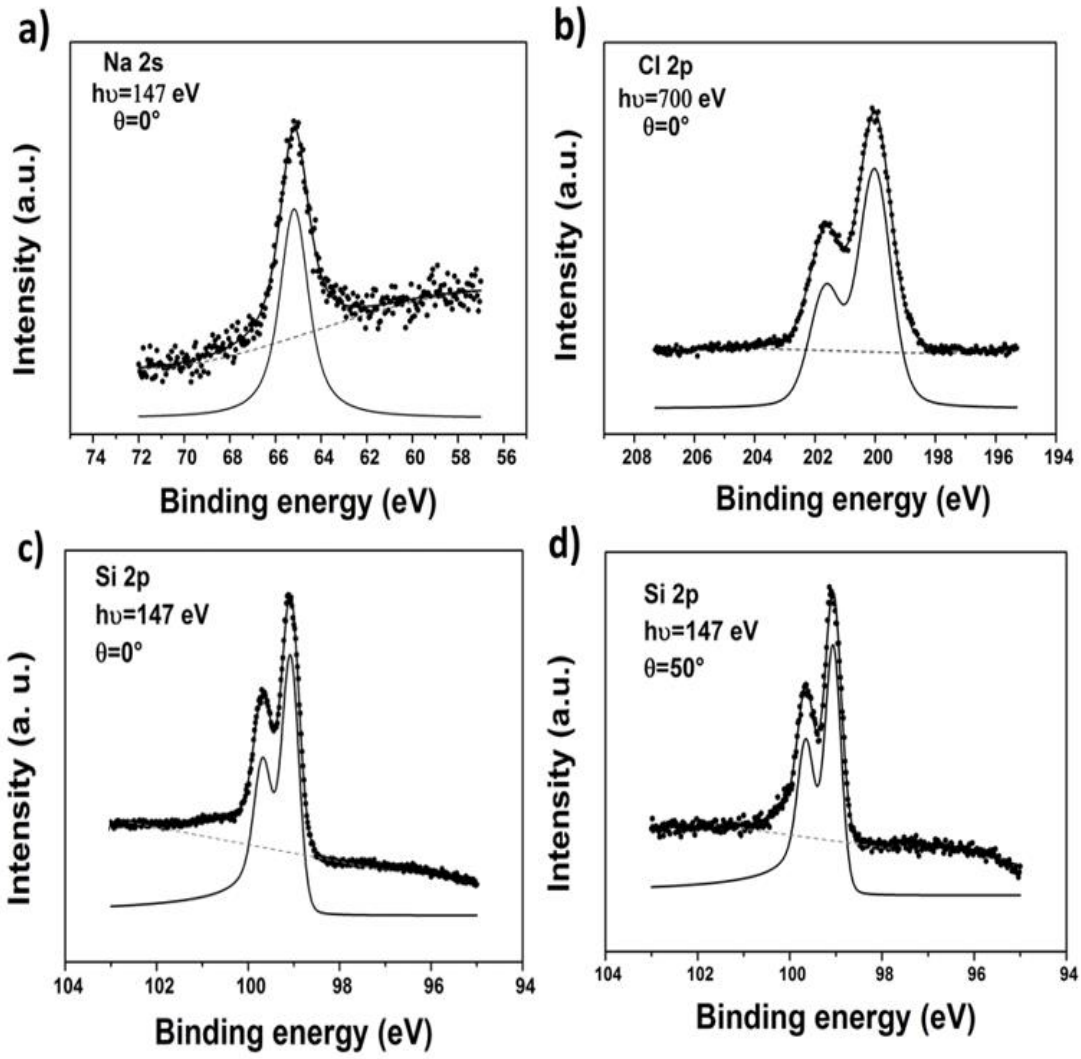

Fig. 3.16 Core level (HR-XPS) spectra (dots) and their de-convolution curves corresponding to: (a) Na (2s), (b) Cl (2p), recorder after deposition of 1 ML of NaCl. (c)-(d) Si (2p) recorded after deposition of 0.7 ML over NaCl/Ag, for normal and off-normal emission, respectively. The spectra were collected at room temperature.

The Si (2p) core level spectra are analyzed with the spin-orbit split Doniach-Sunjich (D-S) function as explained in the methods chapter. The fitting parameters listed below are used.

- Gaussian Width : 255 meV
- Lorentzian Width : 70 meV
- Asymmetry Parameter : 0.13
- Spin-Orbit Splitting : 0.61 eV
- Branching Ratio : 0.48 eV

To obtain the best fit, it is necessary to include an asymmetry of 0.13 indicating that the Si ad-layer possesses a metallic character. This metallic behavior is an agreement with the one observed when analyzing the I(V) spectra recorded on the silicon ad-layer (see figure 3.14a).

From figures 3.16c and 3.16d, it is clear that the Si (2p) peak is composed of only one component (spin-orbit splitted) located at 99.7 eV compared to 99.82 for Si ($2p_{1/2}$) component of silicon bulk [33]. The lower binding energy for the 2D silicon layer was also observed for silicene on diboride thin films [34] and for silicene on Ag(111) [35]. The fact that only one component was needed to fit the Si (2p) peak indicates that silicon atoms have only one chemical environment (Si-Si). On the other hand, from the Si (2p) core level spectra fitting of silicene grown directly on Ag (110) surface [36] it has been found that using two components is necessary. This indicates that silicon atoms have two distinct chemical environments such as Si-Si and Si-Ag.

3.9. ARPES Observations

We will describe now ARPES measurements of the valence band associated to the Si ad-layer. The measurements are performed at room temperature with photon energy of 80 eV along the direction $\bar{\Gamma}$-$\bar{X}$ of the substrate. In figure 3.17a the bands crossing the Fermi level are attributed to bulk states (sp) bands of silver. Here, no evidence of a silicene Dirac cone can be found from the ARPES spectra.

We observed, however, a silicene induced band (I) which is close to the Ag substrate bands. A similar band was observed on silicene/Ag(111) and was identified as a π band modified by the silicene buckled geometry and silicene-silver hybridization [37]. Meanwhile, other studies disagree with this interpretation and argue that the observed band should be assigned to the interface state of free-electron-like Ag substrate localized at the interface [38]. However, we

should note that this band disappears when changing the photon energy indicating that it has a surface or interface character.

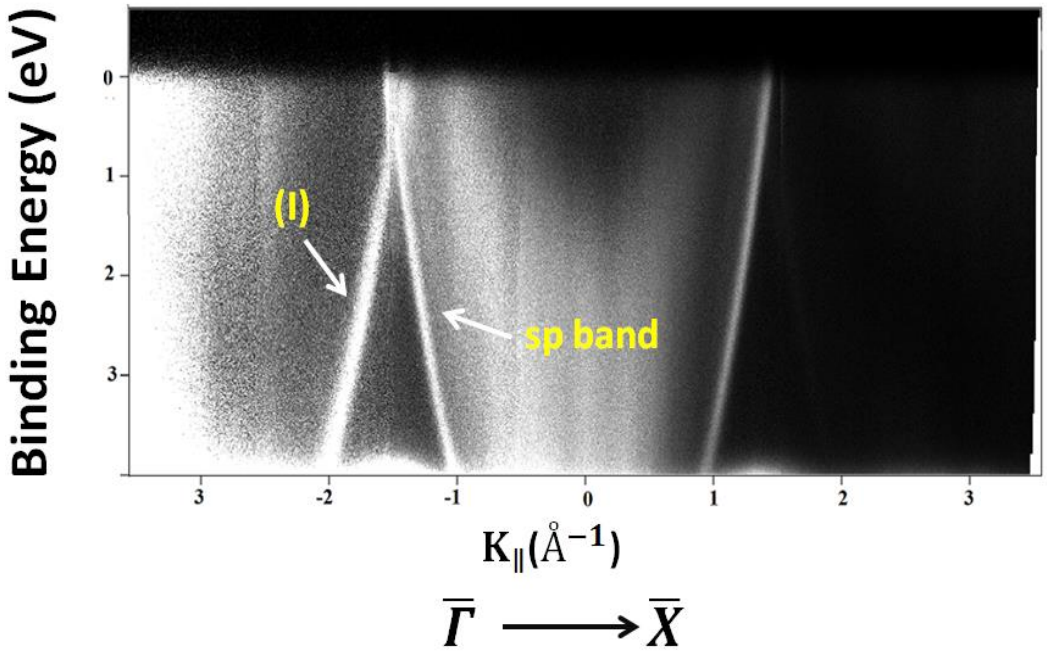

Fig. 3.17 Angle resolved photoemission maps for Si/NaCl/Ag(110) along $\bar{\Gamma}$-$\bar{X}$ direction measured using photon energy of 80 eV.

3.10. EXAFS Measurements

In order to investigate the local structure of the 2D silicon ad-layer grown on NaCl/Ag(110) surface, extended x-ray absorption fine structure spectroscopy (EXAFS) at the Si K-edge is used. EXAFS spectra can help us to determine:

(i) The interatomic distance between the excited atom and its neighbors

(ii) The coordination number for the excited atom and

(iii) The nature of the neighbors

This information allow us to compare the structure of the silicon 2D layer and the silicon crystal. The x-ray absorption spectra have been collected on the LUCIA beamline at Synchrotron SOLEIL. X-ray incident photons are obtained by using a double crystal InSb(111) monochromator. The EXAFS spectra at the silicon K-edge are collected in Total Electron Yield (TEY) mode in ultra-high vacuum chamber (10^{-10} mbar), using variable

energy steps (2 eV between 1820 and 1830 eV; 0.2 eV between 1830.2 and 1872 eV; 1 eV between 1873 and 2600 eV) for a counting time of 2 s per point. The analysis of the raw experimental data was carried out using Athena [39] applying the following parameters: a low-R filtering below 1.4 Å has been used in order to remove the background oscillations and a Kaiser-Bessel window spanning from k= 2 to 9.5 $Å^{-1}$ has been used before applying the Fourier transform. Figure 3.18 shows the modulus and the imaginary part of the Fourier transform of $k^3X(k)$ for bulk silicon crystal and for the 2D silicon ad-layer grown on NaCl/Ag(110). As can be seen, high similarities between the two local structures is evident. As a first result, we can notice that local order surrounding the Si atoms on the 2D silicon ad-layer is highly ordered. We should note that the peaks located at 1.92 Å and 3.4 Å (see figure 3.18a) are assigned to the first and second interatomic distances of silicon bulk crystal and that they are shifted compared to the well-known lattice parameters of 2.35 Å and 3.83 Å due to the effect of phase shifts between the absorbing atom and the backscattering one [40].

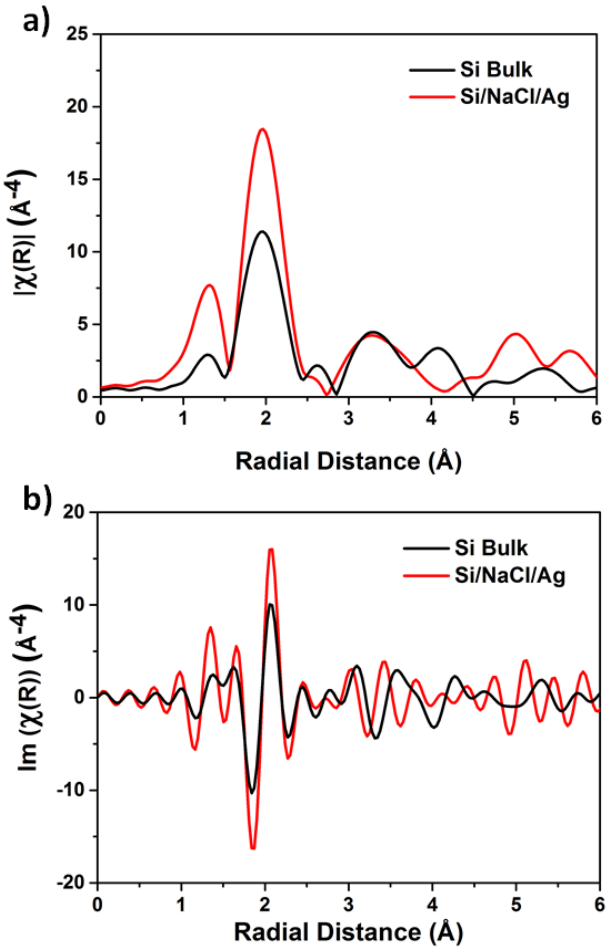

Fig. 3.18 (a) Modulus and (b) imaginary parts of the Fourier transforms of pure crystal silicon bulk and 2D Si sheet deposited on NaCl/Ag.

Taking into consideration the spectra of the imaginary part that holds information about the nature of the silicon surrounding atoms we can assume a local structural ordered around the Si atom in the 2D silicon layer. The first and second interatomic Si-Si distances found are very close to those of the crystal in Si-(111) plane and for the 2D silicene grown directly on Ag(110) or Ag(111) surfaces [41]. Compared to the result from Lagarde et al. [41], where the authors found an interatomic distance around 2.7 Å which was interpreted as Si-Ag bonding for silicene layer on metallic substrate of silver, we notice in our EXAFS analysis the absence of this interatomic distance around 2.7 Å. As a result, taking into consideration the absence of the Si-Ag bond and also the XPS data shown before we can believe that the new silicon ad-layer grows on NaCl layer and not on Ag substrate. Moreover, our results allow us to conclude that the Si layer made during our experiment on NaCl/Ag(110) has great similarities with silicene 2D layer already published but without the substrate coupling effect.

3.11. Conclusion

In this chapter, the experimental procedure, morphology and electronic structure of silicon layer grown on NaCl insulating film deposited over Ag(110) surface are studied.

We demonstrated that after covering the metallic substrate with NaCl islands, the deposition of silicon atoms by molecular beam epitaxy evaporation process produces silicon ad-layer sheet. The LEED shows a new (3x4) superstructure assigned to the silicon new structure. From STM images, we have found that the deposited silicon atoms self-assembly form a silicon sheet with highly ordered honeycomb-like structure. The EXAFS experiment reveals that this silicon sheet grown on NaCl films have similarities with Si(111) plane and silicene grown directly on Ag surfaces. In addition, the EXAFS demonstrates the absence of an interatomic distance around 2.7 Å. This particular interatomic distance was described as Si-Ag bonding distance for silicene/Ag. This observation can confirm the absence of silicene/substrate coupling effect. Moreover, the XPS measurements agree with this result showing only one silicon chemical environment interpreted as Si-Si bonding.

Bibliography

[1] Takeda, K. and Shiraishi, K., 1994. Theoretical possibility of stage corrugation in Si and Ge analogs of graphite. *Physical Review B*, *50*(20), p.14916.

[2] Guzmán-Verri, G.G. and Voon, L.L.Y., 2007. Electronic structure of silicon-based nanostructures. *Physical Review B*, *76*(7), p.075131.

[3] Cahangirov, S., Topsakal, M., Aktürk, E., Şahin, H. and Ciraci, S., 2009. Two-and one-dimensional honeycomb structures of silicon and germanium. *Physical Review Letters*, *102*(23), p.236804.

[4] Wilson, R.J. and Chiang, S., 1987. Structure of the Ag/Si (111) surface by scanning tunneling microscopy. *Physical Review Letters*, *58*(4), p.369.

[5] Aufray, B., Kara, A., Vizzini, S., Oughaddou, H., Leandri, C., Ealet, B. and Le Lay, G., 2010. Graphene-like silicon nanoribbons on Ag (110): A possible formation of silicene. *Applied Physics Letters*, *96*(18), p.183102.

[6] De Padova, P., Quaresima, C., Ottaviani, C., Sheverdyaeva, P.M., Moras, P., Carbone, C., Topwal, D., Olivieri, B., Kara, A., Oughaddou, H. and Aufray, B., 2010. Evidence of graphene-like electronic signature in silicene nanoribbons. *Applied Physics Letters*, *96*(26), p.261905.

[7] Lalmi, B., Oughaddou, H., Enriquez, H., Kara, A., Vizzini, S., Ealet, B. and Aufray, B., 2010. Epitaxial growth of a silicene sheet. *Applied Physics Letters*, *97*(22), p.223109.

[8] Vogt, P., De Padova, P., Quaresima, C., Avila, J., Frantzeskakis, E., Asensio, M.C., Resta, A., Ealet, B. and Le Lay, G., 2012. Silicene: compelling experimental evidence for graphenelike two-dimensional silicon. *Physical Review Letters*, *108*(15), p.155501.

[9] Jamgotchian, H., Colignon, Y., Hamzaoui, N., Ealet, B., Hoarau, J.Y., Aufray, B. and Bibérian, J.P., 2012. Growth of silicene layers on Ag (111): unexpected effect of the substrate temperature. *Journal of Physics: Condensed Matter*, *24*(17), p.172001.

[10] Knox, K.R., Wang, S., Morgante, A., Cvetko, D., Locatelli, A., Mentes, T.O., Niño, M.A., Kim, P. and Osgood Jr, R.M., 2008. Spectromicroscopy of single and multilayer graphene supported by a weakly interacting substrate. *Physical Review B*, *78*(20), p.201408.

[11]Majzik, Z., Tchalala, M.R., Švec, M., Hapala, P., Enriquez, H., Kara, A., Mayne, A.J., Dujardin, G., Jelínek, P. and Oughaddou, H., 2013. Combined AFM and STM measurements of a silicene sheet grown on the Ag (111) surface. *Journal of Physics: Condensed Matter*, *25*(22), p.225301.

[12] Fleurence, A., Friedlein, R., Ozaki, T., Kawai, H., Wang, Y. and Yamada-Takamura, Y., 2012. Experimental evidence for epitaxial silicene on diboride thin films. *Physical Review Letters*, *108*(24), p.245501.

[13] Meng, L., Wang, Y., Zhang, L., Du, S., Wu, R., Li, L., Zhang, Y., Li, G., Zhou, H., Hofer, W.A. and Gao, H.J., 2013. Buckled silicene formation on Ir (111). *Nano Letters*, *13*(2), pp.685-690.

[14] Enriquez, H., Mayne, A., Kara, A., Vizzini, S., Roth, S., Lalmi, B., Seitsonen, A.P., Aufray, B., Greber, T., Belkhou, R. and Dujardin, G., 2012. Adsorption of silicon on Au (110): An ordered two dimensional surface alloy. *Applied Physics Letters*, *101*(2), p.021605.

[15] Sadeddine, S., Enriquez, H., Bendounan, A., Das, P.K., Vobornik, I., Kara, A., Mayne, A.J., Sirotti, F., Dujardin, G. and Oughaddou, H., 2017. Compelling experimental evidence of a Dirac cone in the electronic structure of a 2D Silicon layer. *Scientific Reports*, *7*, p.44400.

[16] Lin, C.L., Arafune, R., Kawahara, K., Kanno, M., Tsukahara, N., Minamitani, E., Kim, Y., Kawai, M. and Takagi, N., 2013. Substrate-induced symmetry breaking in silicene. *Physical Review Letters*, *110*(7), p.076801.

[17] Li, G., Luican, A. and Andrei, E.Y., 2009. Scanning tunneling spectroscopy of graphene on graphite. *Physical Review Letters*, *102*(17), p.176804.

[18] Johnson, N.W., Vogt, P., Resta, A., De Padova, P., Perez, I., Muir, D., Kurmaev, E.Z., Le Lay, G. and Moewes, A., 2014. The metallic nature of epitaxial silicene monolayers on Ag (111). *Advanced Functional Materials*, *24*(33), pp.5253-5259.

[19] Stephan, R., Hanf, M.C. and Sonnet, P., 2014. Spatial analysis of interactions at the silicene/Ag interface: first principles study. *Journal of Physics: Condensed Matter*, *27*(1), p.015002.

[20] De Padova, P., Avila, J., Resta, A., Razado-Colambo, I., Quaresima, C., Ottaviani, C., Olivieri, B., Bruhn, T., Vogt, P., Asensio, M.C. and Le Lay, G., 2013. The quasiparticle band dispersion in epitaxial multilayer silicene. *Journal of Physics: Condensed Matter*, *25*(38), p.382202.

[21] Xu, X., Zhuang, J., Du, Y., Feng, H., Zhang, N., Liu, C., Lei, T., Wang, J., Spencer, M., Morishita, T. and Wang, X., 2014. Effects of oxygen adsorption on the surface state of epitaxial silicene on Ag (111). *Scientific Reports*, *4*, p.7543.

[22] Sahin, H. and Peeters, F.M., 2013. Adsorption of alkali, alkaline-earth, and 3 d transition metal atoms on silicene. *Physical Review B*, *87*(8), p.085423.

[23] Filtvedt, W.O., Holt, A., Ramachandran, P.A. and Melaaen, M.C., 2012. Chemical vapor deposition of silicon from silane: review of growth mechanisms and modeling/scaleup of fluidized bed reactors. *Solar Energy Materials and Solar Cells*, *107*, pp.188-200.

[24] Prévot, G., Hogan, C., Leoni, T., Bernard, R., Moyen, E. and Masson, L., 2016. Si nanoribbons on Ag (110) studied by grazing-incidence x-ray diffraction, scanning tunneling microscopy, and density-functional theory: evidence of a pentamer chain structure. *Physical Review Letters*, *117*(27), p.276102.

[25] Tchalala, M.R., Enriquez, H., Mayne, A.J., Kara, A., Dujardin, G., Ali, M.A. and Oughaddou, H., 2014. Atomic structure of silicene nanoribbons on Ag (110). In *Journal of Physics: Conference Series* (Vol. 491, No. 1, p. 012002). IOP Publishing.

[26] Laukkanen, P., Sadowski, J. and Guina, M., 2012. Surface studies by low-energy electron diffraction and reflection high-energy-electron diffraction. In *Semiconductor Research* (pp. 1-21). Springer, Berlin, Heidelberg.

[27] Davis, L. E., MacDonald, N. C., Palmberg, P. W., Riach, G. E., & Weber, R. E. (1976). Handbook of Auger electron spectroscopy. *Physical Electronics Industries, Eden Prairie, MN*, *27*(6), l.

[28] Berger, C., Song, Z., Li, X., Wu, X., Brown, N., Naud, C., Mayou, D., Li, T., Hass, J., Marchenkov, A.N. and Conrad, E.H., 2006. Electronic confinement and coherence in patterned epitaxial graphene. *Science*, *312*(5777), pp.1191-1196.

[29]Matsui, T., Kambara, H., Niimi, Y., Tagami, K., Tsukada, M. and Fukuyama, H., 2005. STS observations of Landau levels at graphite surfaces. *Physical review letters*, *94*(22), p.226403.

[30] Houssa, M., Pourtois, G., Afanas' ev, V.V. and Stesmans, A., 2010. Can silicon behave like graphene? A first-principles study. *Applied Physics Letters*, *97*(11), p.112106.

[31] Fuggle, J.C. and Mårtensson, N., 1980. Core-level binding energies in metals. *Journal of Electron Spectroscopy and Related Phenomena*, *21*(3), pp.275-281.

[32] Santoni, A., Frycek, R., Castrucci, P., Scarselli, M. and De Crescenzi, M., 2005. XPS and STM study of SiC synthesized by acetylene and disilane reaction with the Si (1 0 0) 2× 1 surface. *Surface science*, *582*(1-3), pp.125-136.

[33] Cardona, M. and Ley, L., 1978. Photoemission in solids I. *Photoemission in Solids I: General Principles*.

[34] Friedlein, R. and Yamada-Takamura, Y., 2015. Electronic properties of epitaxial silicene on diboride thin films. *Journal of Physics: Condensed Matter*, *27*(20), p.203201.

[35] Molle, A., Grazianetti, C., Chiappe, D., Cinquanta, E., Cianci, E., Tallarida, G. and Fanciulli, M., 2013. Hindering the oxidation of silicene with non-reactive encapsulation. *Advanced Functional Materials*, *23*(35), pp.4340-4344.

[36] Leandri, C., Le Lay, G., Aufray, B., Girardeaux, C., Avila, J., Davila, M.E., Asensio, M.C., Ottaviani, C. and Cricenti, A., 2005. Self-aligned silicon quantum wires on Ag (1 1 0). *Surface science*, *574*(1), pp.L9-L15.

[37] Avila, J., De Padova, P., Cho, S., Colambo, I., Lorcy, S., Quaresima, C., Vogt, P., Resta, A., Le Lay, G. and Asensio, M.C., 2013. Presence of gapped silicene-derived band in the prototypical (3× 3) silicene phase on silver (111) surfaces. *Journal of Physics: Condensed Matter*, *25*(26), p.262001.

[38] Mahatha, S.K., Moras, P., Bellini, V., Sheverdyaeva, P.M., Struzzi, C., Petaccia, L. and Carbone, C., 2014. Silicene on Ag (111): A honeycomb lattice without Dirac bands. *Physical Review B*, *89*(20), p.201416.

[39] Ravel, B. and Newville, M.A.T.H.E.N.A., 2005. ATHENA, ARTEMIS, HEPHAESTUS: data analysis for X-ray absorption spectroscopy using IFEFFIT. *Journal of synchrotron radiation*, *12*(4), pp.537-541.

[40] Lee, P.A., Teo, B.K. and Simons, A.L., 1977. EXAFS: A new parameterization of phase shifts. *Journal of the American Chemical Society*, *99*(11), pp.3856-3859.

[41] Lagarde, P., Chorro, M., Roy, D. and Trcera, N., 2016. Study by EXAFS of the local structure around Si on silicene deposited on Ag (1 1 0) and Ag (1 1 1) surfaces. *Journal of Physics: Condensed Matter*, *28*(7), p.075002.

Chapter 4. Growth of Silicene on Dissociated NaCl Ultra-thin Film

In this chapter, we report preliminary experiments investigating the effect of electron bombardment on an NaCl film deposited on Ag(110) metallic surface and the growth of silicene on the electron irradiated NaCl surface.

4.1. NaCl Alkali Halide Electron Irradiation

The dissociation of sodium chloride (NaCl) has been reported for the first time by Tokutaka et al. [1] and Friedenberg et al. [2]. They have shown that upon electron irradiation using low energy electron diffraction (LEED), Auger electron spectroscopy (AES) and reflection high-energy electron diffraction (RHEED) tools, new defects are induced on NaCl crystal bulk due to the effect of the incident electrons. The defects were assigned to halogen vacancies where the halogen atoms (Cl) are ejected out of the surface and the alkali metal atoms (Na) remain. These alkali metal atoms can diffuse and self-assembled to form aggregates of metallic clusters [3]. In the case of ultrathin films of NaCl, it has been found that exposing the NaCl/Ag(110) sample to electron bombardment the NaCl film dissociates resulting on an ordered alkali metal atoms structure (Cl ejection and Na diffusion) [4].

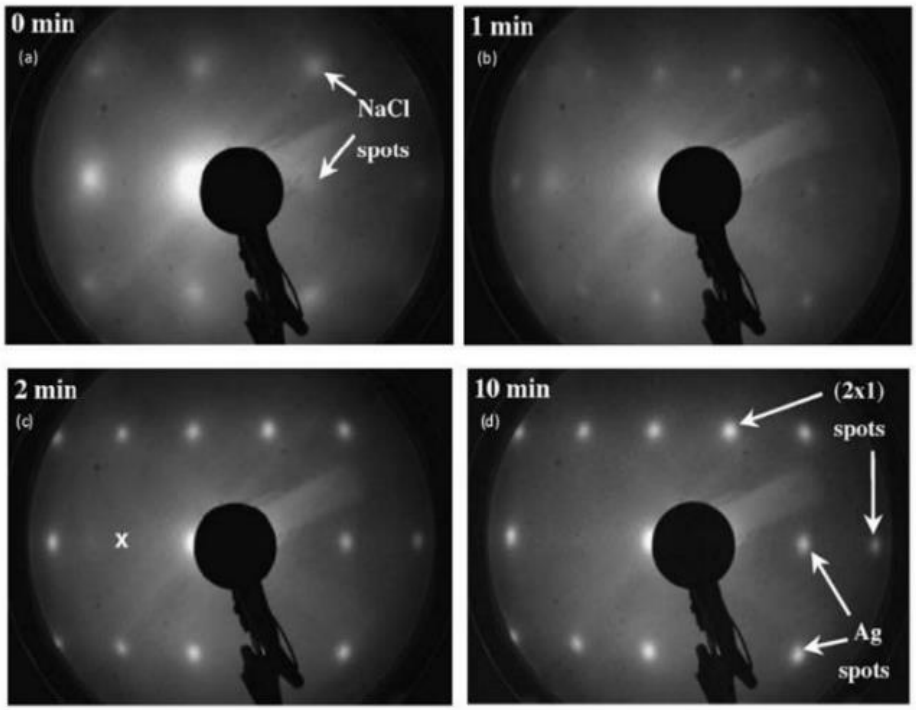

Fig. 4.1 LEED pattern shows the effect of electron bombardment on a 10 ML NaCl film deposited on Ag (110) recorded at 63 eV in the very first stages (a) and its evolution as a function of LEED exposure time: (b) 1 min, (c) 2 min and (d) 10 min. Adapted from [4].

Figure 4.1 shows the effect of LEED exposure on a NaCl films. As can be seen, within a few minutes the (4 x 1) superstructure of NaCl disappears and a new periodic structure of Na atoms appears with a (2 x 1) surface reconstruction. We should note that the same atomic arrangements were found when Na atoms are directly deposited over the Ag(110) surface [5]. On the other hand, similar Na surface reconstruction was reported on the Ag(001) substrate [6]. The new Na atomic arrangement is assigned to a missing row reconstruction of the Ag(001) surface. Figure 4.2 shows the effect of electron bombardment using LEED and AES on 1ML of NaCl grown on Ag(110). As can be seen, the intensity of the Cl peak decreases indicating the Cl ions depletion.

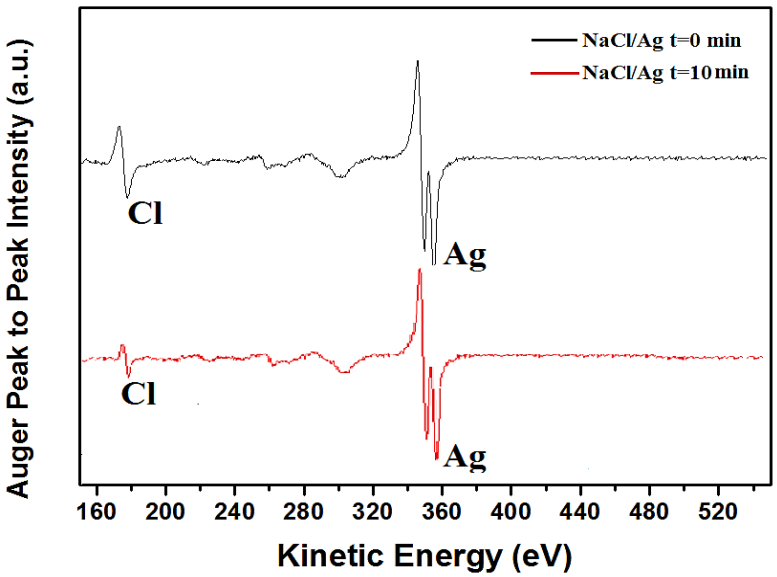

Fig. 4.2 Differential AES showing NaCl dissociation upon surface irradiation with the electron beams of a LEED (primary electron energy 65 eV) and an AES (3 keV)

4.2. Silicon Deposition on NaCl Dissociated Film

Figure 4.3a shows an AES spectrum after deposition of ~1ML of silicon over a completely dissociated NaCl film. In order to completely dissociate the NaCl surface, the sample was kept 30 min under low energy electron beam at 65 eV. Figure 4.3b presents a LEED pattern of the surface. As can be seen, the LEED diffraction reveals a clear c(2x2) superstructure indicating a long range order on the surface.

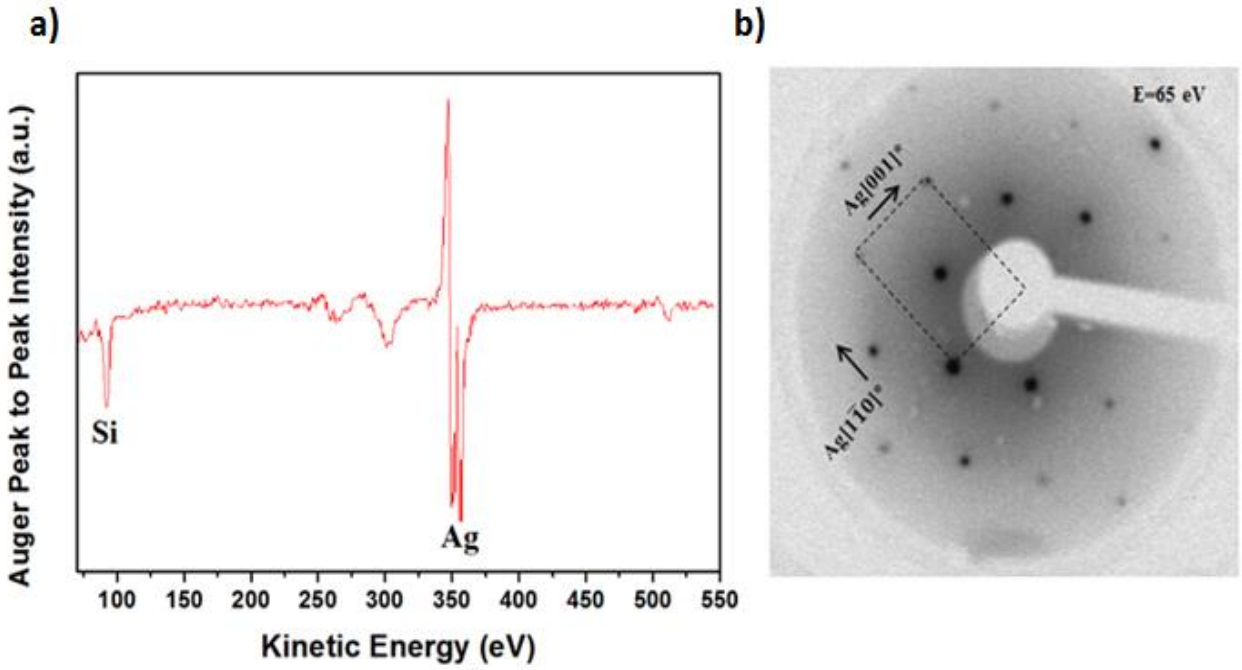

Fig. 4.3 (a) Differential AES mode spectrum recorded on the sample after depositing of about 1 ML of silicon on a dissociated NaCl film. (b) LEED pattern corresponding to ~1 ML silicon deposited over a dissociated NaCl surface grown on Ag(110).

In figure 4.4, the ARPES spectra are shown upon deposition of silicon over Ag(110) with the remaining residual Na atoms from the NaCl film using a photon energy of 60 eV along the $\bar{\Gamma}$-$\bar{X}$ direction of the substrate. As can be seen from the ARPES data, two bands are prominent: sp band of Ag bulk and a conical dispersion band which could be attributed to the silicene Dirac cone. The apex of the band cone is shifted below the Fermi level of about 0.3 eV. From the ARPES data only the π band is detected which means that gap opening π-π^* should be at least around 0.3 eV.

However, we should note that freestanding silicene is expected to have zero gap which means that the observed Dirac cone should be assigned to silicene layer that still has some interaction with the substrate due to π-π^* opening.

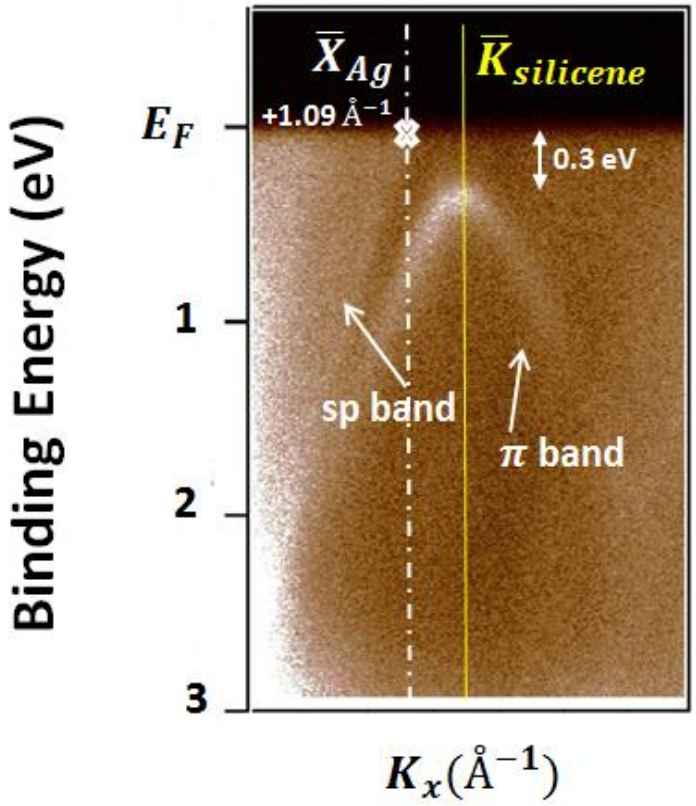

Fig. 4.4 Angle resolved photoemission spectra for Si/NaCl(dissociated)/Ag(110) along $\bar{\Gamma}$-$\bar{X}$ direction measured using photon energy of 60 eV.

We should note also that these experimental observations agree with the theoretical work of Quhe et al. [7]. They have demonstrated that the destroyed Dirac cone of silicene can be effectively restored with linear dispersion by intercalating alkali metal atoms such as K or Na between silicene and the metal substrate. Based on their calculations they have found that the intercalated alkali metal atoms prefer being located beneath the hollow center of the Si honeycomb where Na atoms penetrate Stone-Wales defect in silicene [8,9].

Comparing our experimental ARPES spectra with the calculated band structure [7] in figure 4.5 we find that the band structure of alkali metal K-intercalated interface silicene/K/Ag in which a near linear energy dispersion close to the Dirac point has been found [7]. Furthermore, a band gap of ~0.3 eV is opened between the π and π^* bands. The same gap opening has been observed on our ARPES measurements. This band gap is explained by inversion symmetry breaking between the two silicene sub-lattices [10]. The breaking of the

sub-lattice symmetry is due mainly to the build-in electric field vertical to the silicene plane induced by the charge transfer between the silicene layer and the substrate [11].

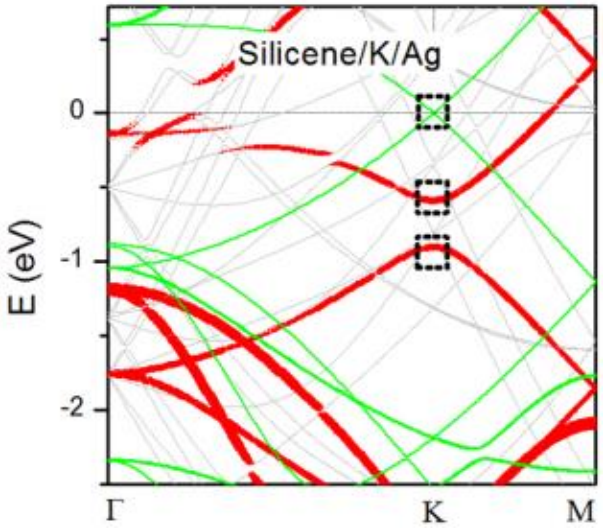

Fig. 4.5 Calculated band structures show epitaxial silicene/K/Ag bands in red and freestanding silicene intercalated K atoms in green. Adapted from [7].

4.3. Conclusion

In this chapter, we demonstrate the effect of electron irradiation on the NaCl film. Indeed, we show that exposing a metallic surface of Ag(110) covered with NaCl islands to electron bombardment of LEED and AES induces Cl atoms ejection. The remaining Na atoms form an alkali metal atoms structure. After deposition of silicon over the new dissociated NaCl film, the ARPES data revealed the existence of a linear dispersion crossing bands that resemble the silicene Dirac cone.

Bibliography

[1] Tokutaka, H., Prutton, M., Higginbotham, I.G. and Gallon, T.E., 1970. The (100) surfaces of alkali halides: II. Electron stimulated dissociation. *Surface Science*, *21*(2), pp.233-240.

[2] Friedenberg, A. and Shapira, Y., 1979. Electron induced dissociation of the NaCl (111) surface. *Surface Science*, *87*(2), pp.581-594.

[3] Kolodziej, J.J., Such, B., Czuba, P., Krok, F., Piatkowski, P., Struski, P., Szymonski, M., Bennewitz, R., Schär, S. and Meyer, E., 2001. Frenkel defect interactions at surfaces of irradiated alkali halides studied by non-contact atomic-force microscopy. *Surface Science*, *482*, pp.903-909.

[4] Aït-Mansour, K., Bielmann, M., Gröning, O., Ruffieux, P., Fasel, R. and Gröning, P., 2006. (2× 1)-Na surface reconstruction induced by NaCl dissociation on Ag (1 1 0) during LEED analysis. *Applied Surface Science*, *252*(18), pp.6368-6374.

[5] Marbrow, R.A. and Lambert, R.M., 1976. Adsorption and surface structural chemistry of Na and Na+ O2 on Ag (110). *Surface Science*, *61*(2), pp.329-342.

[6] Müller, M., Ikonomov, J. and Sokolowski, M., 2011. Structure of epitaxial layers of KCl on Ag (100). *Surface Science*, *605*(11-12), pp.1090-1094.

[7] Quhe, R., Yuan, Y., Zheng, J., Wang, Y., Ni, Z., Shi, J., Yu, D., Yang, J. and Lu, J., 2014. Does the Dirac cone exist in silicene on metal substrates?. *Scientific Reports*, *4*, p.5476.

[8] Hu, W., Wu, X., Li, Z. and Yang, J., 2013. Helium separation via porous silicene based ultimate membrane. *Nanoscale*, *5*(19), pp.9062-9066.

[9] Schrier, J., 2010. Helium separation using porous graphene membranes. *The Journal of Physical Chemistry Letters*, *1*(15), pp.2284-2287

[11] Quhe, R., Fei, R., Liu, Q., Zheng, J., Li, H., Xu, C., Ni, Z., Wang, Y., Yu, D., Gao, Z. and Lu, J., 2012. Tunable and sizable band gap in silicene by surface adsorption. *Scientific Reports*, *2*, p.853.

[11] Ni, Z., Liu, Q., Tang, K., Zheng, J., Zhou, J., Qin, R., Gao, Z., Yu, D. and Lu, J., 2011. Tunable bandgap in silicene and germanene. *Nano Letters*, *12*(1), pp.113-118.

Conclusions & Perspectives

The aim of this PhD study was to investigate the silicene formation/properties on an insulating surface. This approach is very interesting in order to decrease the interaction between the silicene and the metallic substrate. Here we proposed to study the silicene growth on NaCl insulating film which was grown on Ag(110) metallic surface. The first point was to determine the condition in which NaCl film cover the Ag(110) surface.

We demonstrate that several parameters had to be severely constrained. The optimization of the substrate temperature and the evaporation time are key points to obtain large NaCl islands on Ag(110). For instance, we are able to produce very large NaCl islands that cover the metallic surface only when the sample was kept at 140°C.

The grown NaCl film reveal a clear (4x1) superstructure in which the NaCl mesh parameter is close to the Ag(110) one with a mismatch of about 3.55 %, as has been demonstrated in chapter 2. This superstructure indicates the presence of a long range order for the NaCl film on Ag(110). The analysis of the STM images suggest that the initial thickness of the NaCl film is one atomic layer and that the growth of the second and third layers starts after reaching a coverage of about 0.4 ML. We have characterized the obtained thin film by investigating the insulating character of the NaCl layer in which a band gap value of 1 eV was measured using STS. From the XPS measurements, we concluded that the interaction between the NaCl film and Ag(110) substrate is weak. Indeed, the plasmons associated to the bare substrate did not disappeared after growth of NaCl on the surface. A low binding energy of NaCl and Ag(110) was calculated in the range of 0.18 eV. The NaCl core level photoemission reveals also the presence of only one chemical environment for Na and Cl atoms. Indeed the corresponding spectra present only one component in which Na atoms bond with Cl atoms, and vice versa.

After controlling the NaCl film growth, we studied the growth of silicon on NaCl film. The silicon deposition was performed on a sample kept at 140°C followed by a post-annealing at 140°C for 180 minutes. We have characterized the growth of silicon by LEED. The results show a new (3x4) superstructure related to silicon deposition.

With the STM images, we determined that the new 2D silicon sheet mimics the square shape of the NaCl islands. Further zoom-in on this sheet shows an ordered honeycomb-like lattice

silicon structure. The analysis of the STM is in agreement with the formation of a silicene structure on a NaCl film.

In order to investigate the local structure of this silicon layer, we used EXAFS technique which is very sensitive to the local order around the study atom (here the silicon). The results showed high similarities with the local structures of Si(111) plane and silicene grown on Ag(110) and Ag(111) surfaces. More precisely, the EXAFS results allow us to find as for previous study, the first and second Si-Si interatomic distances at 2.35 Å and 3.83 Å, respectively. Furthermore, the analysis of EXAFS spectra reveal the absence of an interatomic distance around 2.7 Å which was interpreted as Si-Ag bonding for silicene layer on metallic substrate of silver. This result is very important because we can conclude that the absence of this distance at 2.7 Å indicate the absence of substrate coupling effect with the silver. The XPS measurements are in agreement with this result, in which only one silicon chemical environment was found presented by Si-Si bonding. We may conclude from these observations that the observed 2D silicon layer represents the first extended silicene sheet on insulator without strong silicene/substrate coupling.

In Addition, the initial ARPES investigations didn't show any intrinsic Dirac cone that can be assigned to the observed silicon ad-layer. We believe that further ARPES measurements are necessary in order to understand the electronic properties of this silicon sheet. In addition, DFT calculations which can provide great insights are expected to be conducted in the near feature in order to gain more info about the structural properties of the silicene/NaCl interface.

In the last part of this thesis, preliminary experiments on the growth of silicene on dissociated NaCl films are conducted. The effect of electron irradiation on the NaCl film and initial ARPES measurement on the silicene intercalated-Na atoms system are presented.

We showed that due to electron irradiation, the Cl atoms are ejected from the surface. The remaining Na atoms self-assembled to form an ordered alkali metal atoms structure. After deposition of silicon ad-layer, the ARPES measurements shows the existence of a Dirac cone with a gap opening π-π^* of about 0.3 eV. More analysis using other surface science techniques such as STM would be necessary. We believe that this silicene-Na-substrate system may open a promising route offering an important opportunity to investigate the electronic properties of silicene without the need to use insulators.

For the future, we believe that investigating the growth of silicene on NaCl bulk insulator is required in order to better understand the silicene/insulator system. Here, the atomic force microscopy (AFM) and DFT calculations would be very helpful to describe and characterize such surfaces.

Résumé Détaillé

Le but de cette étude était d'étudier la formation et les propriétés de la croissance silicène sur une surface isolante. Cette approche est très intéressante pour diminuer l'interaction entre le silicène et le substrat métallique. Ici, nous avons proposé d'étudier la croissance du silicium sur un film isolant de NaCl qui a été développé sur une surface métallique d'Ag (110). Le premier point consistait à déterminer les conditions dans lesquelles un film de NaCl recouvre la surface de Ag (110).

Nous démontrons que plusieurs paramètres ont dû être sévèrement contraints. L'optimisation de la température du substrat et le temps d'évaporation sont des points clés pour obtenir de grands îlots de NaCl sur Ag (110). Par conséquent, nous avons réussi à produire de très grands îlots de NaCl qui couvrent la surface métallique uniquement lorsque l'échantillon a été conservé à 140 ° C.

Le film de NaCl formé révèle une superstructure claire (4x1) dans laquelle le paramètre de maille de NaCl est proche de celui de Ag(110) avec un décalage d'environ 3,55. L'analyse des images STM suggère que l'épaisseur initiale du film de NaCl est une couche atomique et que la croissance des deuxième et troisième couches commence après avoir atteint une couverture d'environ 0,4 ML. Nous avons caractérisé le film mince obtenu en recherchant le caractère isolant de la couche de NaCl dans laquelle une valeur de bande interdite de 1 eV a été mesurée à l'aide de STS. À partir des mesures XPS, nous avons conclu que l'interaction entre le film de NaCl et le substrat Ag (110) est faible. En effet, les plasmons associés au substrat n'ont pas disparu après la croissance de NaCl à la surface. Une faible énergie de liaison de NaCl et Ag (110) a été calculée dans l'ordre de 0,18 eV. La photoémission au niveau du noyau de NaCl révèle également la présence d'un seul environnement chimique pour les atomes de Na et de Cl. En effet, les spectres correspondants ne présentent qu'un composant dans lequel les atomes de Na se lient aux atomes de Cl, et inversement.

Après avoir contrôlé la croissance du film de NaCl, nous avons étudié la croissance du silicium sur un film de NaCl. Le dépôt de silicium a été effectué sur un échantillon maintenu à 140 ° C suivi d'un post-recuit à 140 ° C pendant 180 minutes. Nous avons caractérisé la croissance du silicium par LEED. Les résultats montrent une nouvelle superstructure (3x4) liée au dépôt de silicium.

Utilisons le STM, nous avons déterminé que la nouvelle feuille de silicium 2D imite la forme carrée des îlots de NaCl. Un zoom sur cette feuille montre une structure ordonnée en silicium à réseau en nid d'abeille. L'analyse du STM est en accord avec la formation d'une structure de silicène sur un film de NaCl.

Afin d'étudier la structure locale de cette couche de silicium, nous avons utilisé la technique EXAFS, qui est très sensible à l'ordre local autour de l'atome etudié (ici le silicium). Les résultats ont montré de fortes similitudes avec la structure locale du plan de Si (111) et du silicène sur les surfaces Ag(110) et Ag(111). Plus précisément, les résultats EXAFS nous permettent de retrouver, comme pour l'étude précédente, les première et seconde distances interatomiques Si-Si à 2,35 Å et 3,83 Å, respectivement. En outre, l'analyse des spectres EXAFS révèle l'absence d'une distance interatomique autour de 2,7 Å, interprétée comme une liaison Si-Ag pour une couche de silicène sur un substrat métallique d'argent. Ce résultat est très important car nous pouvons conclure que l'absence de cette distance à 2,7 Å indique l'absence d'effet de couplage du substrat avec le silicène. Les mesures XPS sont en accord avec ce résultat, dans lequel un seul environnement chimique de silicium a été trouvé présenté par liaison Si-Si. Nous pouvons conclure de ces observations que la couche de silicium 2D observée représente la première feuille de silicène étendue sur un isolant sans couplage fort silicium / substrat.

Dans la dernière partie de cette thèse, des expériences préliminaires sur la croissance de silicène sur des films de NaCl dissociés sont présentés. L'effet de l'irradiation électronique sur le film de NaCl et la mesure initiale d'ARPES sur le système d'atomes de silicène-Na-substrat sont présentés. Nous avons montré qu'en raison de l'irradiation électronique, les atomes de Cl sont éjectés de la surface. Les atomes de Na restants pour former une structure ordonnée d'atomes de métal alcalin. Après le dépôt de silicium, les mesures ARPES montrent l'existence d'un cône de Dirac avec une ouverture d'ouverture de gap d'environ 0,3 eV.

Résume (max 200 mots)

Le silicène est l'équivalent du graphène pour le silicium avec une structure bidimensionnelle (2D). Il est supposé avoir des propriétés électroniques intéressantes comme les fermions de Dirac sans masse et présentant une grande mobilité des électrons. L'existence du silicène a été montrée récemment sur des substrats de métaux nobles comme l'argent. Cependant les résultats montrent des interactions fortes entre la couche de silicène et le substrat métallique, ce qui a pour conséquence de détruire les propriétés électroniques intrinsèques du silicène.

Dans le but de résoudre ce problème, nous proposons dans ce travail d'explorer d'autres substrats potentiels présentant de faibles interactions avec le silicene. Nous avons étudié la croissance de couches 2D de silicium sur un film mince isolant de NaCl.

Nous avons étudié les propriétés structurales et électroniques des couches de silicium 2D déposées sur un film mince de NaCl, lui-même déposé sur un substrat d'Ag (110). L'absorption d'atomes de silicium sur les films de NaCl révèle l'existence d'une couche de silicium 2D superficielle avec une structure très ordonnée en forme de nids d'abeilles. Cette couche présente une interaction faible avec le substrat tout en étant analogue au silicène.

Mots-clefs (5) : Science des surfaces, microscope à effet tunnel, silicène, LEED, XPS

Abstract (max 200 mots)

Silicene, the silicon-based analog of graphene which has a two-dimensional (2D) structure. It is expected to have attractive electronic properties such as massless Dirac fermions and high electron mobility. The existence of silicene has been shown recently on noble metal substrates such as Ag and Au. The results present strong interactions between the silicene ad-layer and the metallic substrate which destroy the intrinsic electronic properties of silicene.

In order to solve this problem, we propose in this work to explore other potential substrates that have weaker interactions with silicene. We studied the growth of a 2D silicon layer on insulating NaCl thin film.

We studied the structural and electronic properties of 2D silicon layer grown on a NaCl film deposited over Ag (110) substrate. The adsorption of silicon atoms on NaCl films reveals the existence of a 2D silicon sheet ad-layer with a highly ordered honeycomb-like structure. The silicon ad-layer has weak interactions with the substrate and it mimics the structure of silicene.

Key Words (5): Surface science, tunneling microscope, silicene, LEED, XPS